Influence of catalyst ink mixing procedures on catalyst layer properties and in-situ PEMFC performance

By

Clayton Jeffery Jacobs

Submitted in partial fulfilment of the requirements for the degree of

Master of Science in Engineering

Supervised by:
Dr. Pieter Levecque (Core supervisor)
Mr. Nabeel Hussain (Co-supervisor)
Dr. Bernhard Schwanitz (Co-supervisor)

Centre for Catalysis Research

Department of Chemical Engineering

University of Cape Town

March, 2016

Abstract

Despite the benefits of fuel cell technology its advancement to being commercially functional is hindered by a number of crucial factors. These factors are often associated with the lack of appropriate materials or manufacturing routes that would enable the cost of electricity per kWh to compete with existing technology.

Whilst most research efforts have been directed towards developing more active catalysts, the amount of catalyst required in the fuel cell can be further reduced by improving the platinum utilisation in the membrane electrode assembly. The platinum utilisation is a strong function of the catalyst layer preparation step and there remains significant scope for optimisation of this step.

Whereas significant work has been conducted into the different components of the catalyst ink there is limited work and understanding on the influence of the mixing method of the catalyst ink. This study will focus on the influence of the mixing technique on the catalyst ink properties and on the final fuel cell performance. Specifically, the study will investigate the effect of the three different mixing techniques on (i) catalyst ink quality (ii) the physical properties of the resultant catalyst layer and (iii) the in-situ electrochemical performance of the membrane electrode assembly.

A large set of characterisation techniques were chosen to effectively study the step wise processing of the catalyst layer, and fuel cell performance. The results presented here include a comparison of the various mixing techniques and a comprehensive 2 x 2 factorial design into the individual techniques. The results suggest that high energy mixing is required for effective distribution of catalyst layer components, an even catalyst layer topography and a highly functional ionomer network which consequently, enhances performance. The mixing energy referred to involves prolonged mixing time, enhanced mixing intensity or a combination of the two. During bead milling of catalyst inks, high intensity mixing seems to be beneficial however, prolonged mixing time appears to be detrimental to the ionomer film structure. During high shear stirring and ultrasonic homogenisation of catalyst inks, the ink mixture significantly heats up. It has been observed that at higher temperatures, Nafion elongates and the contact with catalyst agglomerates is enhanced. High shear stirring of catalyst inks seems to be most effective at high agitation rates. High mixing energies result in high shear forces and in addition, high mixing temperatures which appear to be beneficial to establishing an effective catalyst/Nafion interface, enhancing the three phase boundary observed during in-situ testing. Ultrasonic homogenisation seems to be more effective at prolonged sonication times. Due to the erosive nature of ultrasonic dispersion, sufficient time is required to establish a well dispersed and distributed catalyst ink. However, the nature of particle size distribution resulting from ultrasonication shows that inks are unstable and is not recommended for high throughput processing.

Overall, fuel cell performance is not significantly affected by the mixing step however; mixing does have an observable impact on catalyst layer formulation. Generally, when optimizing membrane electrode assembly fabrication, mixing parameters should be carefully chosen. This goes without saying that parameters need to be effectively studied before foregoing catalyst ink processing.

Acknowledgements

“I can do all things through Christ who strengthens me.”

(Philippians 4:13, NKJV)

Firstly, all thanks to the Lord God for giving me knowledge and strength; Who carried me through this journey.

I would like to thank my supervisors for the tremendous amount of hard work and patience they had to endure through the duration of this project. Pieter Levecque thank you for being so helpful and always available to consult with. Nabeel Hussain thank you for being such a great mentor in both academic and personal matters. Bernhard Schwanitz, thank you for all the inspiration and your insights on life.

I would like to thank the all the members of Centre of Catalysis Research for all their help, especially Dr. Olaf Conrad, Dr. Sharon Blair and Dr. Shiro Tanaka.

I would like to thank Miranda Waldron (Centre for Imaging and Analysis, UCT), Zulfa Le Riche (Analytical Laboratory, UCT) and Piotr Bujło (HySA Systems Competence Centre, UWC), for the tremendous amount of effort put into assisting me with characterisation.

Thanks to those who made time spent in the lab enjoyable. Namely: Tereshan Gangen, Tapiwa Chivengwa, Thulile Khoza and a special thanks to Tshepang Tsieane for your willingness to assist me.

I would like to thank my friends and family members, who always tried to make things a bit easier. A special thanks to my mother, Tania Cox, and father, Alexander Jacobs, who always supported me and believed I could.

Lastly I would like to thank my Fiancé, Candis Field and my son, Micah Jacobs for being patient and understanding. My love for you extends infinity.

Plagiarism Declaration:

I know the meaning of plagiarism and declare that all the work in the document, save for that which is properly acknowledged, is my own.

Signed by candidate

Signature removed

Table of Contents

Page

List of Figures

Page

List of Tables

Page

List of Symbols

e^-	Electron
H^+	Proton
η_a	Apparent viscosity
$\mathcal{E}$	Dielectric constant
κ	Rheological consistency index
τ	Shear stress
γ	Shear rate

Glossary

BM	Bead milling
CCM	Catalyst coated membrane
CL	Catalyst layer
CCS	Catalyst coated substrate, referring to catalyst coated onto Teflon sheet.
Decal	Peeling off of the catalyst layer (coated on a substrate) onto a membrane after hot pressing.
ECSA	Electrochemical Surface Area
EDX	Energy-dispersive x-ray spectroscopy
EIS	Electrochemical Impedance Spectroscopy
FC	Fuel cell
GDL	Gas diffusion layer
HSS	High shear stirring
MEA	Membrane electrode assembly
MPL	Microporous layer
Nafion	Membrane ionomer which has an aliphatic perflourinated backbone with ether linked side chains and sulfonate cation exchange sites at the ends.
PEM	Proton exchange membrane or Polymer electrolyte membrane
PEMFC	Polymer electrolyte membrane fuel cell
PTFE	Polytetrafluoroethylene used as a decal substrate.
SEM	Scanning electron microscopy
TPB	Three phase boundary
UH	Ultrasonic homogenisation

1. Introduction

In a proton-exchange membrane fuel cell (PEMFC), the catalyst layer (CL) is one of the most important components under consideration in terms of achieving a high performance with reduced costs as substantiated in Figure 1. Recent advances and discoveries in the PEMFC space have led to the catalyst layer and catalyst coated membrane (CCM) as attractive area for optimisation and cost reduction. During fuel cell operation, transport paths for electrons, gases and protons are established by carbon, pore channels and Nafion, respectively. Inadequately established paths can limit the electrochemical reactions in the CLs. Therefore, understanding and optimising CL components are important to facilitating the benchmark to high fuel cell performance (Suzuki et al., 2011).

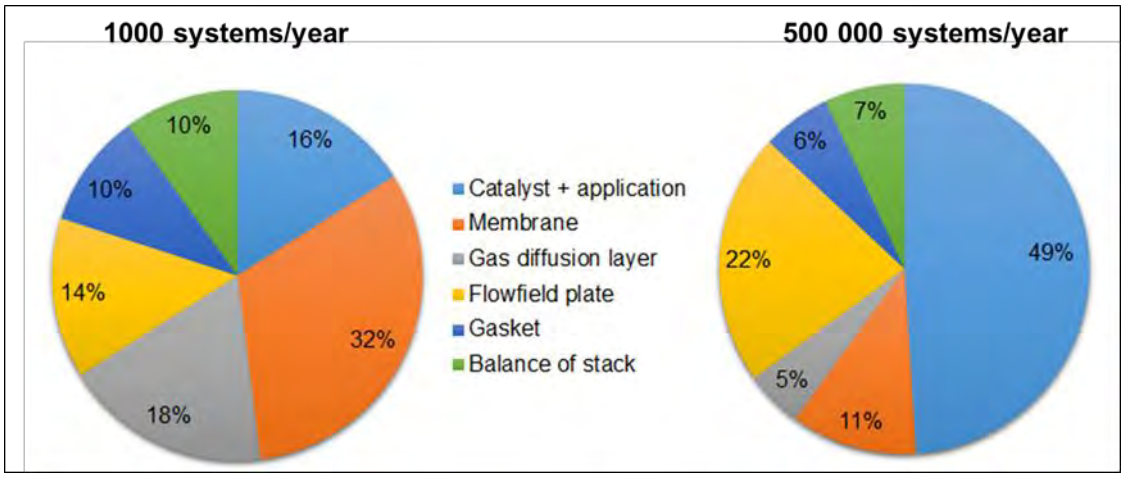

Figure 1: The U.S. Department of Energy projections show that as we move to larger systems output, catalyst layer and application costs become almost half of the total fuel cell cost (U.S. Department of Energy, 2013).

1.1 History of Fuel Cells

Fuel cells are one of the oldest electrical energy converting systems known to man. Chemical energy was successfully converted into electrical energy in a primitive fuel cell which was first demonstrated over 100 years ago (Yuan & Wang, 2008). During its first century, fuel cell development lacked, as abundant and inexpensive energy sources were available. The use of electrochemical conversion systems became more important during the start of the 20th century due to the increase in demand for flexible electrical systems (Carrette et al., 2001). The PEMFC was invented at General Electric in the 1960s. In the Gemini Space Program, repeated technical difficulties faced with PEMFCs made its use impractical. This was a major setback for the development of PEMFCs. Research by Ballard Power Systems led to a revival of interest in PEMFCs in 1980s. From this point, interest in PEMFCs intensified and a number of institutions worldwide contributed to several innovations to bring the concept of PEMFCs to what it is today (Yuan & Wang, 2008). A major driving force behind fuel cell development is the increasing concern about the environmental consequences due to the use of fossil fuels for electricity production and vehicle propulsion. Fuel cells have the potential to reduce our dependence on fossil fuels and diminish the emissions of poisonous gases into the atmosphere (Wang et al., 2011).

1.2 Basic Principles of Hydrogen Fuel Cells

A fuel cell is a galvanic cell in which the free energy of a chemical reaction is converted into electrical energy. The anodic reaction can either involve the direct oxidation of hydrogen, methanol or a reformate gas. For the hydrogen/oxygen fuel cell with an acid electrolyte, the following reaction principal is followed (Srinivasan, 2006):

Anode reaction:

$$H_2 \rightarrow 2H^+ + 2e^- \quad (1)$$

Cathode reaction:

$$\frac{1}{2}O_2 + 2H^+ + 2e^- \rightarrow H_2O \quad (2)$$

Overall combustion reaction:

$$H_2 + + \frac{1}{2}O_2 \rightarrow H_2O \quad (3)$$

At standard conditions (25°C), the thermodynamic equilibrium voltage for the cell is 1.23 V. Furthermore, myriad parasitic losses that occurs during fuel cell operation does not allow the system to realise this cell voltage. As a consequence, the voltage drops and practical fuel cell efficiency is about 55 – 65 % (Ramani, 2006). The oxygen reduction kinetics contributes to one of the major voltage losses as a result of the high reduction overpotential in the performance of a PEMFC. This is therefore a great limiting factor in energy conversion efficiency of PEMFCs. Therefore investigation of the oxidation reduction reaction (ORR) remains a major focus for PEMFC research (Zhang, 2008).

1.3 Structure of Fuel Cell

In its immanent form, fuel cells consist of two electrodes separated by an electrolytic medium connected by an external circuit. The electrodes are exposed to either a gas or liquid fuel and oxidant supply. The currents produced in the cell would be small due to the low contact area between the gas, electrode and electrolyte; and the large distance between electrodes. To overcome this, electrodes are usually made flat using a thin layer electrolyte. The electrode has a porous structure in order to allow gases and electrolyte to penetrate it. This provides a maximum possible contact area between the electrode, gaseous species and electrolyte. The permeability of the electrolyte should be low as reactant gases (hydrogen and oxygen) brought into contact would combust in a highly exothermic reaction (Larminie et al., 2003). Shown in Figure 2, the major constituents in a PEMFC assembly are the anode and cathode, consisting of: bipolar plates containing reactant feeding channels; gasket material; gas diffusion layers; catalyst layers and polymer electrolyte membrane. Together they combine in a compact unit converting chemical energy stored in reactants, to generate electricity.

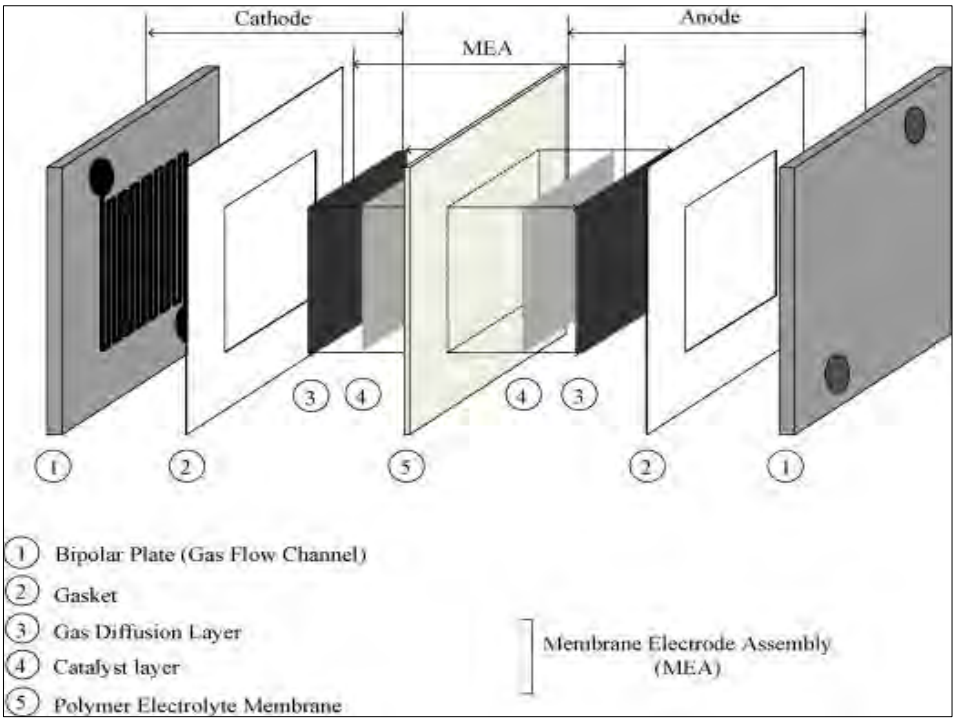

Figure 2: A simplified schematic of a PEM fuel cell (Tang et al., 2010).

1.4 Types of Fuel Cells

Fuel cells are usually classified in terms of the type of electrolyte incorporated, with the exception of Direct Methanol Fuel Cells which is named by its type of fuel. Another way of classifying fuel cells is in terms of their operating temperatures. There are low temperature and high temperature fuel cells. Low temperature fuel cells which operate at a temperature range of 80°C - 200°C are the Alkaline Fuel Cell (AFC), Direct Methanol Fuel Cell (DMFC), the Phosphoric Acid Fuel Cell (PAFC) and the Polymer Electrolyte Membrane Fuel Cell (PEMFC). High temperature fuel cells operate at temperatures in the range 600°C - 1000 °C. Examples of these are the Molten Carbonate Fuel Cell (MCFC) and the Solid Oxide Fuel Cell (SOFC) (U.S. Department of Energy, 2015).

1.5 Polymer Electrolyte Membrane Fuel Cells

PEM fuel cells are low temperature fuel cells (operating temperature: 80°C - 120 °C) which make use of a solid proton exchange membrane. These were the first fuel cells to be used in space application. Due to the polystyrene sulfonate polymer membrane not being stable enough though, they were replaced by the AFC system. A major breakthrough in the field of PEM fuel cells occurred when DuPont developed the Nafion membrane which was significantly more stable and conductive than the membranes used at the time (Zaidi, 2009).

1.6 Membrane Electrode Assembly

The membrane electrode assembly (MEA) is the core of the PEMFC. It determines the durability and performance of the fuel cell. The improvement and optimisation of fuel cells are highly dependent on MEA component materials, structure and fabrication technologies used. As shown in Figure 3, the MEA consists of five layers, sandwiched in series. The

anode and cathode consists of a gas diffusion layer and a catalyst layer, each located adjacent to a proton exchange membrane. An ideal MEA would allow all the catalyst sites to be made available to reagents (H_2 and O_2), facilitate in the transport of protons and electrons, and effectively remove produced water (Haile, 2003). It has been shown that by changing the catalyst layer structure and investigating the use various components, the performance of MEAs significantly improves (Larminie et al., 2003).

1.6.1 Proton Exchange Membrane

The function of the membrane in the MEA is to facilitate the transport of protons from the anode to the cathode and to separate the fuel from the oxidant. The membrane must be able to withstand harsh conditions such as high and rapid temperature fluctuations, strong oxidants and reactive radicals (Wang, Li & Yuan, 2011). Various types of membranes have been tested for use in PEM fuel cells. These membranes are composed of polymers containing sulfonic groups incorporated for proton conduction. Early membranes only lasted between 200 - 500 hours before degrading (Zhang, 2008). Today one of the most widely used membranes is Nafion. Nafion has an aliphatic perflourinated backbone with ether linked side chains and sulfonate cation exchange sites at the ends, depicted in Figure 4. It has been reported that Nafion 120 operating at conditions of 43°C - 82 °C achieved 60 000 hours of operation. Generally, the lifetime of the membrane determines the lifetime of the MEA (Vielstich, Lamm & Gasteiger, 2009).

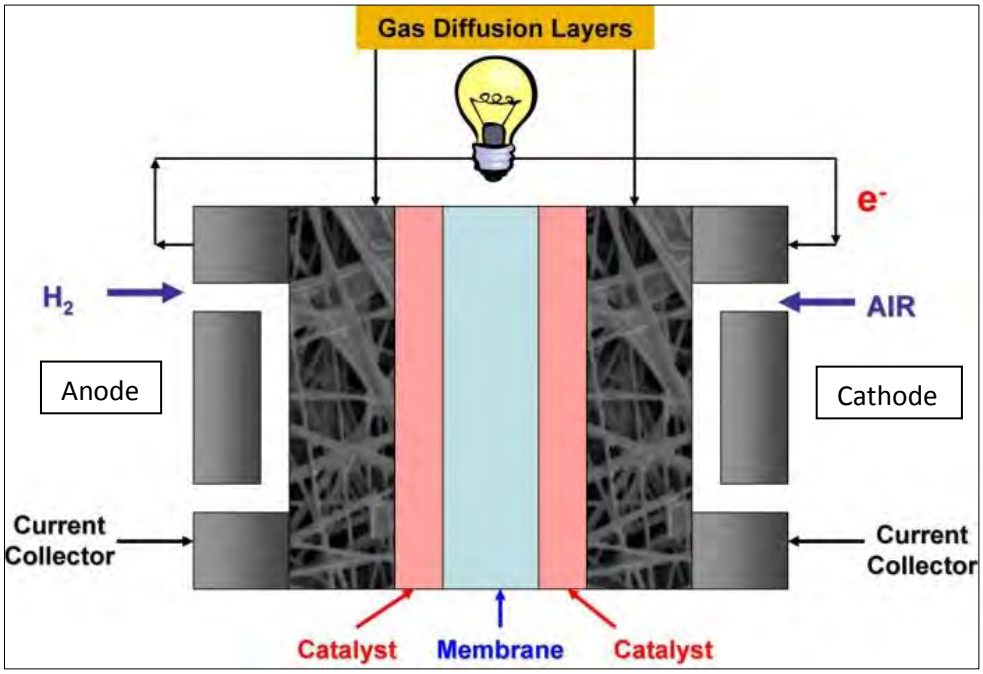

Figure 3: Schematic showing the basic operation of a PEM fuel cell (AimyBazylak, 2015).

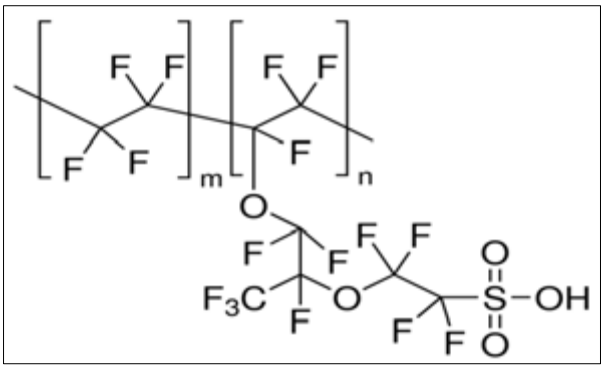

Figure 4: Chemical structure of perflourinated Nafion (Sigma Aldrich, 2016).

1.6.2 Gas Diffusion Layer

The gas diffusion layer (GDL) in a PEM fuel cell is a porous material responsible for the transport of gases to the catalyst layer in the MEA. The GDL also serves as an electronic connection between the carbon supported catalyst and the bipolar plate (or other current collectors). Additionally, the GDL aids water management in the fuel cell. The GDL has a dual-structure and is usually made of a carbon based porous substrate such as carbon paper or cloth. The first layer is a macro porous layer whose function is to provide structure, electron conduction and elasticity to the MEA. The second layer known as the micro porous layer (MPL) is composed of carbon black powder and a hydrophobic agent. The MPL is responsible for providing an appropriate surface pore size and hydrophobicity, which avoids flooding and enhances electrical contact between its interface and the catalyst layer (Cindrella et al., 2009).

1.6.3 Role of the Catalyst Layer in PEM Fuel Cells

In order to advance development in the fuel cell field, it is essential to understand the underlying factors impeding this move forward. The major challenges facing fuel cell development originate in the catalyst layer as it is a highly complex and heterogeneous structure. With respect to the catalyst layer, the foremost objective is to obtain the highest transfer current density from desired reactions with a minimum amount of catalyst (Malek et al., 2007). In order to increase the active surface area, the catalyst particles are reduced to the nanometre domain. The structure of the nanoparticles is a major influential component to the overall functioning of the catalyst layer. The move from fabrication to commercialisation is often deflected due to the challenges faced by electrocatalyst characterisation. Physiochemical properties such as particle and agglomerate size, porosity, surface chemistry, crystal structure, surface area and particle dispersion are some of the factors that may influence electrocatalyst behaviour (Williams et al., 2009).

2. Literature Review

2.1 Challenges Faced by PEMFC's

Although PEM fuel cells are a very promising technology, a number of challenges arise. One of the major factors impeding its move forward is material cost. A number of costly materials are required to produce an efficiently operating MEA. One of the most important and most costly materials is the use of a platinum based catalyst (Mathias et al., 2005). Much research has been geared towards developing higher activity catalysts. Other research focus areas are: reducing the catalyst loading by improving the utilisation of catalyst in the MEA; finding optimum ionomer to carbon ratio and investigating optimum fabrication parameters, such as solvents types and quantity (Brandon et al., 2003). The latter involve the actual preparation of the catalyst layer and hence form the basis for this work. In the next section, factors specifically related to the catalyst layer will be discussed.

2.2 CL and Three Phase Boundary

Platinum has been found to be the best catalyst for both the anode and cathode. Nano-sized platinum particles are usually deposited onto a larger support material such as carbon powder. A commonly used carbon powder is Vulcan XC72. A support is used to spread out the platinum particles increasing the amount of reaction sites per unit catalyst mass, thus increasing the catalyst (Pt/C) activity. A more active catalyst allows for a reduction in platinum loading and an increase in power output (Zhang, 2008).

The formation of the catalyst layer can be depicted by the self-organisation of the Pt/C and ionomer in the colloidal ink solution, leading to the formation of phase-segregated structures (Eikerling & Kornyshev, 1998). Figure 5 shows the carbon primary particles consisting of deposited platinum nanoparticles; usually depicted as spherical, with size approximately 20 nm. These form agglomerates which size range from 100 nm – 300 nm. Agglomerates coalesce into chain like aggregates which size typically range from 1 µm – 3 µm (Soboleva et al., 2010).

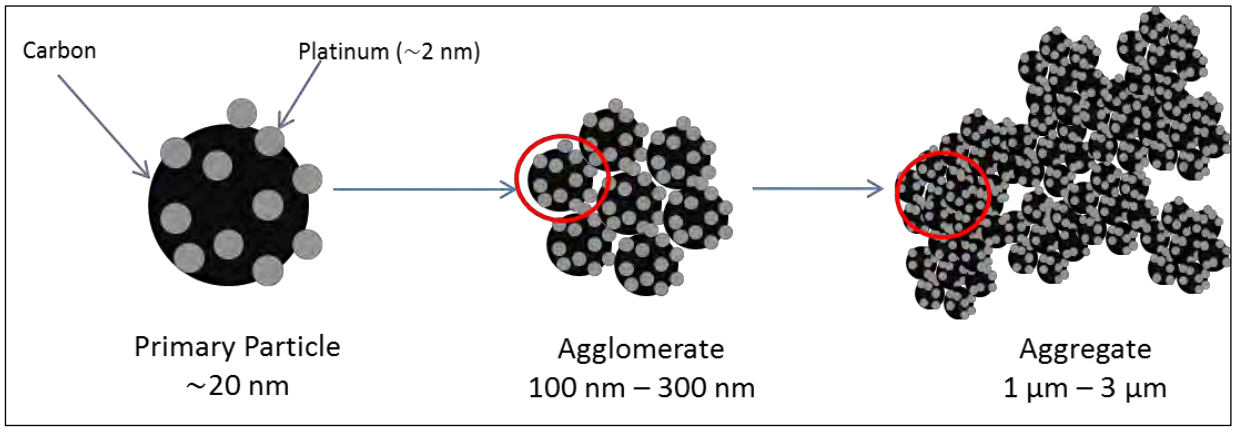

Figure 5: A schematic showing the microstructure of the CL (adapted from Soboleva et al., 2010).

A major requirement for the catalyst layer is the so-called three (triple) phase boundary (TPB). The concept of TPB holds that the hydrogen oxidation reaction and the oxygen

reduction reaction can only occur at confined spatial sites where electrolyte, gas, and electrically connected catalyst regions contact (O'Hayre et al., 2005). As shown in Figure 6, the TPB consists of (i) gas pores which supply oxygen, contain nitrogen, gaseous water and liquid water; (ii) dispersed ionomer (PEM), a complex porous medium which adsorbs water and facilitates proton conduction; embedded in (iii) an agglomeration of carbon and platinum catalyst where electrochemical reactions takes place (Berg et al., 2006). As aforementioned, the reaction kinetics (especially the ORR) often significantly limits fuel cell performance. Therefore, understanding, characterizing, and optimizing the TPB in fuel cells provides excellent opportunities for performance enhancement (O'Hayre et al., 2005).

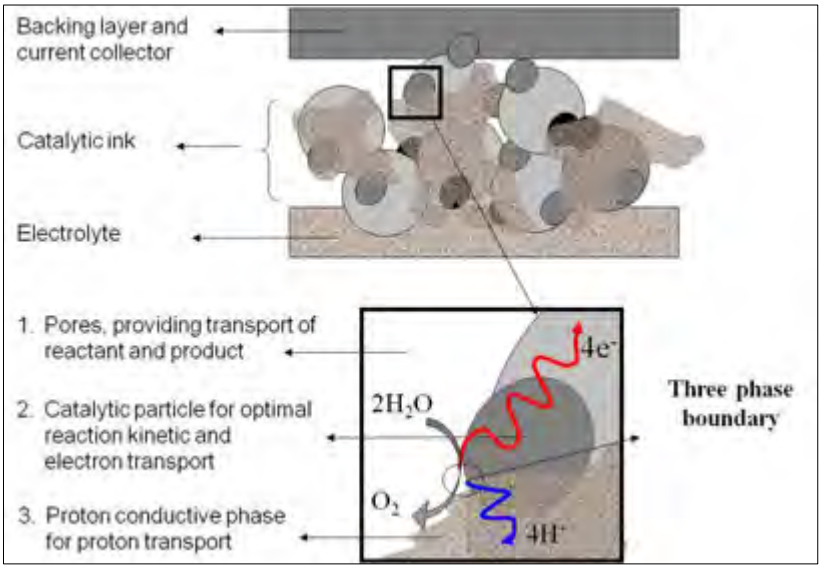

Figure 6: A simplified schematic diagram of the three phase boundary (Bladergroen et al., 2012).

2.3 Parameters Influencing Catalyst Layer Behaviour

Many problems surrounding PEMFC research arises from the catalyst layer, as the structure is fairly complicated. It is well known that the performance of the MEA is greatly affected by the formation and uniformity of a polymer electrolyte network in the catalyst layer. Much focus has been dedicated to maximising the catalyst/electrolyte interface and in doing so, extend the TPB reaction zone (Wang et al., 2007).

Important properties of the catalyst layer provided by the three phase boundary (i.e. active reaction area, porosity and electronic/protonic conductivity) and catalytic activity are largely determined by the fabrication method and the properties of the components. Up to the present time several catalyst layer application techniques have been developed. Of these are spraying, blading, printing, painting, rolling and screening. Each of these have their unique qualities, thus it is difficult to determine which technique is the overall best (Zhang, 2008).

To understand the influence fabrication parameters have on the catalyst layer quality, it is necessary to understand the function and behaviour of its components and the layer as an entirety.

2.3.1 Catalyst Layer Fabrication

There are basically two methods of preparing an MEA for a PEMFC as illustrated in Figure 7. The first uses an appropriate application technique to add the supported catalyst onto a carbon cloth or paper, also known as the gas diffusion layer based application (Figure 7a). The catalyst ink solution is applied to the surface of the GDL which is then dried. A catalysed GDL is often referred to as a gas diffusion electrode (GDE) (Cho et al., 2009). Using two GDEs, the MEA is fabricated by hot pressing them together with the membrane located in the centre. Another method is membrane based fabrication, sometimes referred to as catalyst coated membrane (CCM, Figure 7b). One method involves applying the ink directly onto the membrane and allowing the complex to dry. The GDL is then applied when assembling the cell. Another method involves applying the catalyst ink onto a transfer film, dried and then hot pressed onto the membrane. The resulting complex undergoes a transfer step where the resulting catalyst layer is transferred onto the membrane by peeling off the transfer film, also known as decal; the GDL is applied when assembling the cell (Frey & Linardi, 2004).

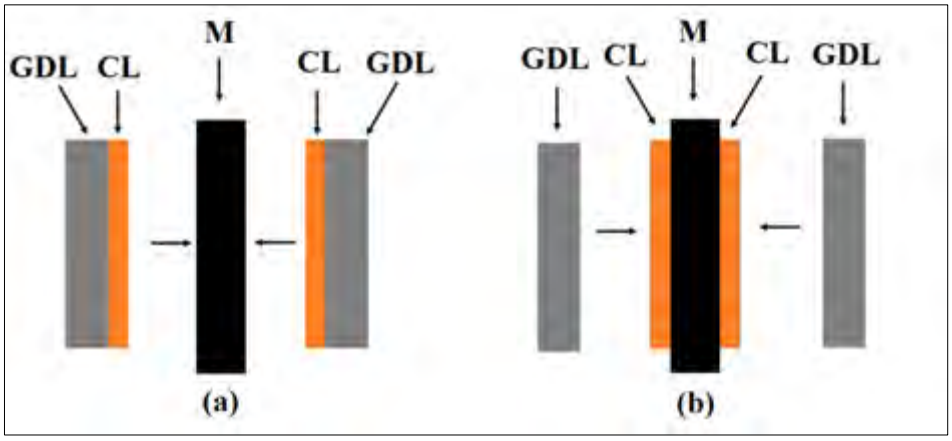

Figure 7: Schematic shows the two ways of applying ink during MEA fabrication. (a) Gas diffusion electrode (GDE) and (b) Catalyst coated membrane (CCM).

It is clear that all commonly used catalyst layer preparation techniques use a catalyst ink as application medium. It is therefore crucial to understand the properties of such inks.

2.3.2 Ink Characteristics

In general, electrode designs are differentiated by the structure and fabrication of the catalyst layer. There are two widely used designs to construct membrane electrodes. These electrode designs are the PTFE-bound and thin-film electrodes. Emerging but less commonly employed methods are those featuring catalyst layers formed with electrodeposition and vacuum deposition (Litster & McLean, 2004).

2.3.2.1 Hydrophobic Inks

Hydrophobic catalyst inks contain a hydrophobic agent such as polytetrafluoroelthylene (PTFE). PTFE acts as a binding agent for catalyst particles, induces hydrophobicity to the catalyst layer and provides pathways for gas transportation. If the PTFE content is too high, the catalyst particles could become wrapped, which results in a decreased conductivity and

catalyst utilisation. An optimal PTFE content range is 10-40 wt. % (Zhang, 2008). PTFE bound catalyst layers was the conventional method employed before the use of ionomer. Later, in order to provide ionic transport to the catalyst site, the PTFE-bound catalyst layer was impregnated with Nafion by brushing or spraying. Platinum utilisation in PTFE bound electrodes is about 20% (Litster & McLean, 2004).

2.3.2.2 Hydrophilic Inks

In a hydrophilic catalyst ink, the binding agent is replaced with a hydrophilic perfluorosulfonate ionomer (PFSI) such as Nafion. Nafion can exist in different states depending on the dielectric constants (Ɛ) of the solvents it is dissolved in. Nafion forms a solution in solvents with Ɛ>10, a colloid in those between 10 and 3, and a precipitate in those Ɛ <3. The function of ionomer is to increase proton conductivity from the catalyst layer to the membrane. The addition of PFSI has to be optimised to such an extent as to maximise the contact between ionomer and Pt particles and minimise the electron/gas transport resistances. Too high ionomer content could result in low porosity caused by gas transport resistance and water build-up. An ionomer to carbon (I/C) ratio of 0.8 - 1 is usually optimal (Zhang, 2008).

The most common electrode design currently employed is the thin-film design. The thin-film design is characterized by the thin Nafion film that binds carbon supported catalyst particles. The thin Nafion layer provides the necessary proton transport in the catalyst layer. This is a significant improvement over its predecessor; however, one drawback of the Nafion thin-film method is its reduced resiliency (Litster & McLean, 2004).

2.3.2.3 Electrodeposition and Vacuum Deposition Methods

These methods make use of depositing catalyst metals from a source to a target material. Both methods have the ability to achieve very low loadings (lowest reported loading is 0.0073 $mg.cm^{-2}$). Common vacuum deposition methods include chemical vapour deposition, physical or thermal vapour deposition, and sputtering. The sputtering of catalyst layers consists of a vacuum evaporation process that removes portions of a coating material (the target) and deposits a thin and resilient film of the target material onto an adjacent substrate (Litster & McLean, 2004). Sputter deposition is a relatively cheap technique and the deposition process can be directly controlled however, the performance of sputter deposited electrodes is still inferior to that of conventional ink-based electrodes (Wilkinson et al., 2009).

2.3.3 Development of Catalyst Ink and MEA Preparation

There are a number of factors which could influence the performance of fuel cells as a result of the catalyst layer formulation. Early fuel cell catalyst layers were prepared by mixing Pt powder and PTFE; the resulting electrodes contained very high loadings of Pt (4 $mg.cm^{-2}$) (Alkire et al., 2006). Even though these electrodes proved to show long term performance, cost was a prohibitive factor to consumer application. Lower Pt loadings were therefore necessary to make PEM fuel cells marketable. Later, Nafion was incorporated into electrodes which extended the three phase reaction zone and greatly reduced Pt loadings to 0.35 $mg.cm^{-2}$ (Ticianelli et al., 1988). Later, they increased the activity of the supported Pt by an additional 50 nm sputter coat of Pt; the performance they observed was equivalent to a Pt black electrode with nearly ten times the amount of Pt in comparison. However, this

technique resulted in a low catalyst utilisation of between 10 - 20% and the electrodes were prone to delamination from the membrane (Ticianelli et al, 1988). Initially CLs were directly applied to a GDL, however, these two components (CL & GDL) had different properties (due to its functional differences) and optimising performance became complicated. To overcome this Wilson & Gottesfeld, (1992a) suggested preparing an ionomer bound hydrophilic catalyst layer using the decal transfer technique. This is done by coating catalyst ink onto a blank substrate followed by a decal transfer step. This allowed the CL and gas diffusion backing to be independently prepared and formulated to its function. The decal technique improved the integrity between the CL-membrane interface, improving H^+ conduction hence, overall FC performance. Later, to further increase ionic contact, the catalyst ink solution was directly sprayed onto both sides of the membrane. Electrodes purely containing solubilised ionomer (Nafion) as a binder are described to be "thin-film" CL's as high performance was obtained at very low Pt loading (0.12 $mg.cm^{-2}$) at thickness of <10 μm (Alkire et al., 2006). Due to the thinness and high ionomer loadings achievable in these CL's, high catalyst utilisation and enhanced CL-membrane interface were possible. Lee et al., (1997) studied the effects of Nafion loading on electrode polarisation characteristics. They found that Nafion content predominantly influences the mass transport polarisation. In order to increase Pt utilisation it is vital to increase the contact area between catalyst and protonic ionomer. In order to achieve this, ionomer-bound hydrophilic catalyst layers have been developed. It has been reported that a catalyst bound to a hydrophilic catalyst layer could improve catalyst utilisation up to 45 % (Cheng et al., 1999). Song et al., (2000) further developed this idea of a hydrophilic CL and a hydrophobic GDL. They developed the catalyst supporting layer (now known as microporous layer - MPL) containing PTFE and carbon in terms of thickness and composition. This layer improved water management properties of the MEA and thus improved cell performance over conventional MEA's. Figure 8 illustrates the change in structure when an MPL is added to the MEA.

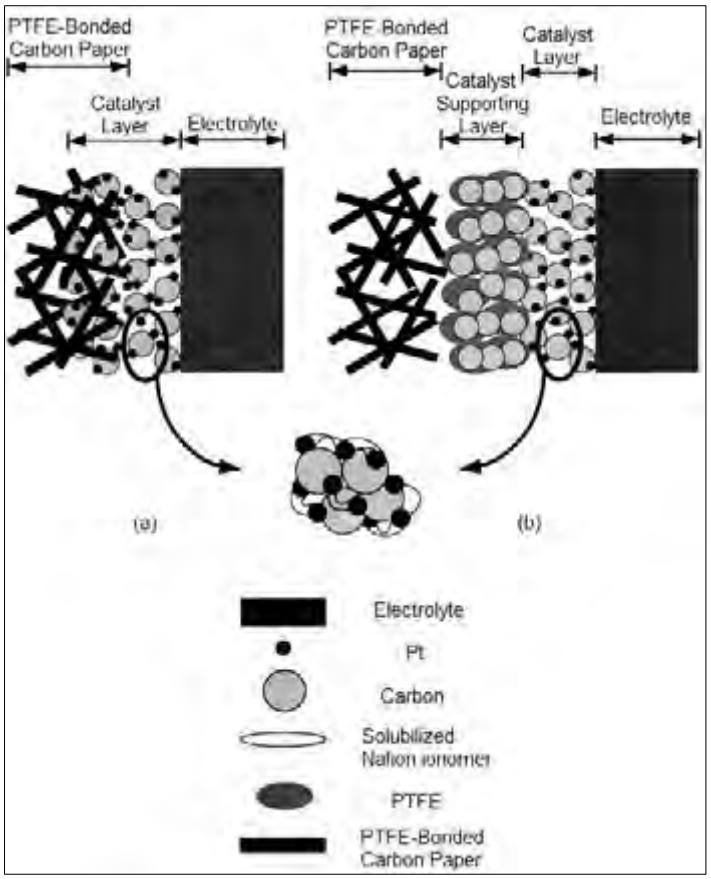

Figure 8: Schematics depicting the electrode: (a) without the catalyst-supporting layer; (b) with the catalyst-supporting layer (adapted from Song et al., 2001).

MEA preparation conditions were found to have a significant influence on the performance. Park et al., (2007) studied the influence of GDE drying on fuel cell performance. Using isopropanol as a solvent, they found that drying temperature influences the pore structure and volume in the CL, thus recommend that a careful selection of solvent and drying temperature could significantly improve FC performance.

Low loading CL electrodes could also be formed by spraying catalyst inks onto the GDL. Qi & Kaufman, (2003) used a mixture of Nafion and water without the addition of any other solvent and applied it to a GDL. A Nafion content of 30% and Pt/C loading of 0.12 $mg.cm^{-2}$, testing under ambient conditions, yielded the best performance. They further suggested ways of increasing the FC performance: (i) steam electrodes prior to testing (Qi & Kaufman, 2002b); (ii) do a H_2 evolution on electrodes which could change the porosity and tortuosity of the catalyst layer, using an external power source (He et al., 2002); (iii) operate the fuel cell at elevated temperature and pressures before operating under normal conditions (Qi & Kaufman, 2002a).

It is believed that when using the Nafion in the colloidal state, fuel cell performance is enhanced. The colloid ionomer adsorbs catalyst particles to form larger agglomerates and this enhances gas transportation and assists the construction of the catalyst microstructure. A colloid method is more suitable for GDL application as larger agglomerates do not easily penetrate the GDL (Shin et al., 2002). Gas transfer through the hydrophilic catalyst layer can be improved by inducing hydrophobic gas pathways into the catalyst layer through

pyrolysing a part of the ionomer. This is done by applying the hydrophilic catalyst ink (containing Nafion) onto the GDL and heating it in the temperature range of 208-340 °C. The sulfonic group is lost during the heating process which results in the surface Nafion groups to act as a hydrophobic agent. The rest of the unpryolysed material still serves as proton conducting material. Following this, a small amount of Nafion is sprayed onto the surface of the electrode which increases the adherence between the catalyst layer and the membrane. This method essentially secures electrical contact and in addition, evades water build-up within the catalyst layer and thus improves cell performance (Zhang, 2008).

By comparing performance, electrochemical and physical properties Shin et al., (2002) studied the effect of catalyst ink preparation on electrode structure and performance by spraying catalyst inks onto carbon paper. Using butyl acetate (ε = 5.01) as the colloidal solvent and isopropanol (ε = 18.30) as the solution solvent, they found that the MEA with the colloidal form produced a 20 % improvement in the cell performance compared to the MEA prepared using the solution form. The effect of the colloidal method is illustrated below (Figure 9).

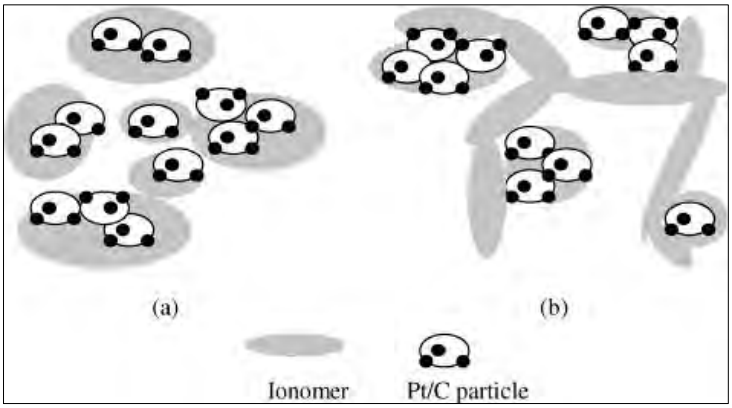

Figure 9: The schematic of the microstructure of CL prepared using (a) the solution method compared to (b) the colloidal method as proposed by Shin et al., (2002).

Described in Figure 9, the solution method “blocks” the conduction of electrons by covering Pt/C with ionomer (a), whereas the colloidal ink adsorb ionomer onto the Pt/C and subsequently improving porosity (b).

Later a different fabrication method was studied by Yang et al., (2004). They investigated the effect of solvent type on fuel cell performance using the decal transfer method. In contradiction to the findings of Shin et al., (2002), performance analysis (conducted using polarisation curves) shows that the solution form of Nafion produced a better MEA performance. Fernandez et al., (2005) studied series of solvent parameters on fuel cell performance. They propose that the deposition of the ink requires a compromise between the dielectric constant and physical properties such as viscosity and boiling point of the solvent. When preparing catalyst ink using low dielectric constant solvents such as butyl acetate, it is necessary to use additional components to the ink mixture, as it is very volatile and has a low viscosity. This ensures a stable suspension during the ink deposition process. Four solvents were used together with glycerine for the preparation of inks during their study and the ink was sprayed onto carbon cloth. Here performance curve analyses had shown that low dielectric constant solvents produced a higher performance compared to high dielectric constant solvents, also shown by Shin et al., (2002). Therdthianwong et al., 2010

studied the influence of solvent type on fuel cell performance using the decal transfer method. Similar to Yang et al., (2004) that also used a membrane based fabrication method; their findings indicate that an ink solution using a higher dielectric constant produces a higher cell performance, compared to low dielectric constant solvents. They suggest that the performance difference compared to Shin et al., (2002) and Fernandez et al., (2005) might be due to the use of a different fabrication technique.

Huang et al., (2011) concluded that particles in ink with a high viscosity are more stable than in ink with low viscosity. Solvents with a high boiling point have low evaporation rates and are therefore more stable during coating; but it is difficult to remove them afterwards. They suggest that viscous ink is preferred for doctor blade spreading and thinner ink for nuzzle spraying.

2.4 Effect of Hot Pressing Conditions on CL Transfer during Decaling

The exact effect of hot pressing on the overall performance of MEAs is complex and not well understood. A limited amount of studies have specifically investigated this and the results are summarised in Table 1.

Table 1: Hot pressing parameters for decal process for Pt/C CCM preparation as described in literature

Author	Temperature ˚C	Time minutes	Pressure MPa
Ren et al., 1996	125	2	10.6
Song et al., 2005	180	1.5	9.8
Cho et al., 2011	140	4.0	15.7
Yoon et al., 2011	240	3.0	6.0
Ngo et al., 2013	130	1.0	9.8

Cho et al., (2009) studied the effects of using various decal substrate materials on the transfer of the CL to the membrane. Of the four materials used, Teflon, PDMS, Kapton, and Al foil; Teflon was the only material to produce a complete transfer under hot press conditions of 8 MPa and 180 ˚C for 8 minutes. The authors describe the order of material superiority as a decal substrate as: Teflon, PDMS, Al foil and the poorest Kapton. They also observed that when an additional layer of ionomer solution is added to the surface of the CL, the adhesion of the CL to the membrane increases and subsequently improves decal transfer of the CL. Saha et al., (2010) suggested that using colloidal inks increases Pt/C agglomerate sizes and subsequently improves the transfer of the CL to membrane during the decal process. In order to improve the decal process scheme, Yoon et al., (2011) treated the membrane prior to hot pressing by brushing the surface with various solvents. The addition of 1-pentanol significantly improved CL transfer and thus lowered decal operating temperatures to 110 ˚C at 6 MPa for 3 minutes. Liang et al., (2015) reports an improved decal transfer process by decaling the substrate immediately after hot pressing, whilst maintaining the substrate at the pressed temperature. They achieved 100 % transfer by hot pressing at 6 MPa and 120 ˚C for 3 minutes.

It is common to transfer the membrane to the Na^+ form by NaOH treatment to improve its mechanical strength prior to decaling; then re-protonating it after decaling, by boiling it in

H_2SO_4 (Cho et al., 2009). However, this enhances the complexity of the decaling process. A number of alternate factors that could influence the decal transfer process are substrate thickness; CL thickness and ionomer loading; and the type of membrane used.

2.5 MEA Characterisation Techniques

The heart of the PEM fuel cell is the MEA which is a multiphase material composing of a number of interconnected components. A subcomponent to the MEA is the catalyst layer. It is well understood that CL preparation influences the microstructure, electron/proton conductivity, mass transport and chemical kinetics therefore overall performance of the fuel cell. Therefore, studying and optimisation of the CL and its components is crucial for fuel cell development. In doing so, a minimum set of properties should be considered during electrocatalyst characterisation as it is implausible to characterise every property. The collection of data should be standardised to a systematic protocol where only a selection of properties are examined during characterisation (Williams et al., 2009).

2.5.1 Modelling of CL

Catalyst layer modelling plays an important role in developing knowledge for fuel cell optimisation. In order to effectively model the CL, microstructural characterisation is required coupled with an appropriate model to accurately predict the behaviour of fuel cells. Current microscopic characterisation techniques do not allow the simultaneous visualisation of all CL components (Scheiba et al, 2008). Among the commonly used CL models, the agglomerate model is considered to be the most theoretically detailed. The physical transport processes, successfully modelled in the agglomerate model is: (i) gas transport in the pore spaces; (ii) dissolution of chemical reactant in the electrolyte phase; (iii) diffusion and reaction of the dissolved reagents; (iv) ion transport in the electrolyte and (v) electrical conduction via carbon particles (Harvey et al, 2008). Recent advances in nano-tomography have made it possible to construct simulations so that it resembles what is observed in a real CL, though computational costs are very high and is time consuming. With the aid of FIB/SEM tomography data, Zhang et al., (2015) produced a simplified model describing oxygen reduction in the cathode CL. Their results showed that resistance due to oxygen diffusion through ionomer and agglomerates are minor, and that the main losses are due to oxygen dissolution in the ionomer film. The mutual symbiotic relationship between microscopy and modelling is ever developing and thus attention in both research areas is imperative for the development of the fuel cell industry.

2.5.2 Electron Microscopy

Electron microscopy is a commonly used characterisation technique and has proved to be crucial to unlocking the knowledge to advance the fuel cells industry.

Scanning Electron Microscopy (SEM) is one of the most commonly used techniques to examine the microstructural characteristics of solid objects. Conventional SEM has a resolution of between 5 – 10 nm. During SEM analysis, a finely focused electron beam sweeps over a bulk specimen. Once the electron beam obtrudes the surface of the specimen, it generates different signals of which are backscattered electrons (BSEs), secondary electrons (SEs) and X-ray fluorescence (elemental mapping). The BSEs are a result of elastic scattering, where the intensity of the signal increases with atomic number

and generates a compositional contrast image of the specimen (Z contrast). The SEs are lower energy electrons. The emission volume is confined around the impact and detection of this signal is dependent on the tilt of the sample. Thus, SEs generates topographical contrasts (shadow effects) of the specimen. Typical SEM images of the CL are shown in Figure 10.

Determining the general structure of the MEA is carried out by embedding the MEA in a resin under a vacuum and allowing the sample to dry. Once dry, the sample is polished to a mirror-like finish, and then coated with a thin conductive carbon layer prior to SEM. Alternatively, cryofracturing of the MEA is a fast and easy way to image the cross section by SEM analysis. The MEA is very brittle at cryogenic temperatures therefore a centimetre length sample would be sufficient to do examinations using this method.

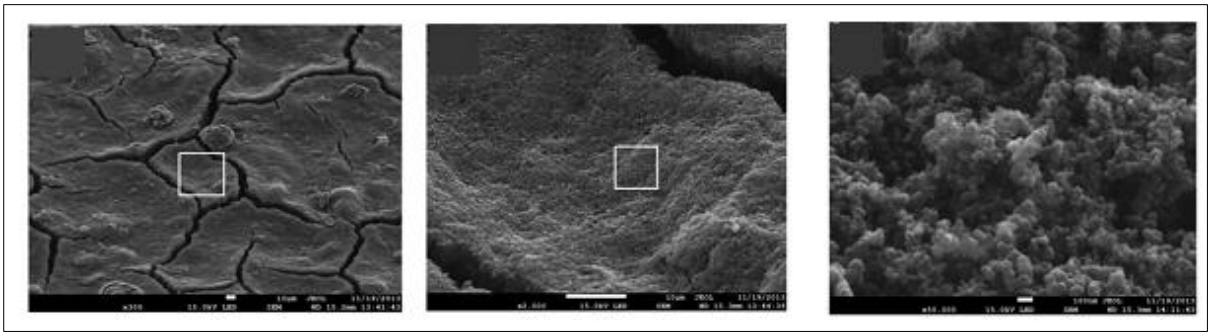

Figure 10: Sample SEM images showing CL surface and pore structure (Poynton et al, 2014).

Unlike SEM, Transmission Electron Microscopy (TEM) requires transmission of incident electron beams and therefore TEM is only used with samples thinner than a few hundred nanometres. During TEM, the electron beam lights the area analysed and the electron-generated image is magnified by electromagnetic lenses. TEM resolution can be below 0.2 nm and allows atomic imaging of crystalline materials.

When using SEM to image electrodes, the electron beam penetrates deeply into the sample. The carbon support is very porous and has a low density. This limits the obtainable resolution for Z-contrast BSEs and element resolved imaging, as these signals depend on the excitation volume. The excitation volume being referred to is the amount of material contributing to the signal. This might produce a level of discrepancy to what the true sample actually represents. However, Scheiba et al., (2008) investigated the use of SEM and TEM for electrode characterisation and found that energy dispersive x-ray microanalysis (EDX) and BSE imaging of the MEA to be suitable to characterise catalyst dispersion. Due to weak fluorine signal, EDX imaging did not provide much detail on Nafion distribution. When using energy filtered transmission electron microscopy (EF-TEM), Nafion was found to form several nanometers thick coating around the catalyst support. TEM cannot be used to image large agglomerate particles (>100 nm in diameter) and therefore using SEM is more favourable in this respect. SEM can be used to analyse a larger sample area in comparison to TEM and therefore produce a more representative set of information.

Due to the sulfonate or sulfonic acid side chains of the PFSA ionomer, it is possible to increase the imaging contrast by staining the PFSA with a suitable heavy metal ion, by an

ion exchange chemical reaction. Rieberer & Norian, (1992) used Cs^+ as a dopant and managed to observe Nafion ionomer filling catalyst agglomerates. Later, Uchida et al., (2006) used Ag^+ to observe the ionomer-carbon interaction under TEM. Cs^+ was replaced with Ba^{2+} as it bonds more strongly to sulfonate groups and when doing so, a more visible staining effect was obtained. However, CL doping is subject to discrepancy as membrane swelling could lead to image distortion during the staining process (Scheiba et al., 2008).

2.5.3 Porosimetry

Pore structure characterisation plays an important role in understanding the microstructural behaviour of CLs. This becomes particularly useful when trying to understand the mechanism of mass transport and important when developing optimisation strategies for fuel cell CLs. Mercury Intrusion Porosimetry (MP) is a well-known method used to characterise PEMFC materials and electrodes. Using MP, determination of pore size is based upon the intrusion of Hg into samples under an external pressure. The pressure required is a function of pore size and is expressed in the Washburn equation. Pore sizes ranging from a few nano-meters up to several hundred micro-meters could be measured using MP (Franco, 2013).

MP is a destructive method as the required pressures (>1000 bars) can lead to the deformation of samples and thus produce a distorted pore size distribution (PSD). This technique should therefore not be used for brittle and soft materials, thus has limited application in characterising PEMFC components. Uchida et al., (1995) used MP to characterise CL microstructure whilst investigating the effect ionomer and PTFE content on fuel cell performance. During their investigation they identified the primary and secondary pore structures and observed a boundary separating the two at about 40 nm. Pores below 5 nm were regarded as inaccessible for reactant transport as they do not form an interconnected pore network. Xie et al., 2004 used a combination of TEM, SEM and MP to characterise PSD. They observed that the majority of pores were located in 24 – 84 nm range and was independent of whether the support contained catalyst particles or not. It was noted that the pore structure of the MEA CL was different to that of the catalyst support. Their results led them to conclude that the nature of the pore structure is dependent on catalyst type, ionomer content and preparation method.

Brunauer-Emmett-Teller (BET) Nitrogen Adsorption-Desorption is a popular technique for characterising porous materials in the range of 0.35 – 100 nm. This is a convenient method and relatively inexpensive compared to other methods available. Here PSD can be determined using the Barrett-Joyner-Halenda (BJH) algorithm (Franco, 2013). Ma et al., (2007) used MP to evaluate the total surface areas of Pt/C catalysts, exposed to different temperatures (90 – 200 °C). The microstructures of carbon supports, Pt/C catalyst powders and the CLs were studied by Soboleva et al., (2010). PSD was differentiated into different zones being: primary particles (<2 nm), the void space inside agglomerates called the mesopores (2-20 nm) and macropores inside aggregates of agglomerates (>50 nm). They found that the deposition of platinum influenced the micropores; and ionomer content significantly influenced pores (mesopores) less than 20 nm.

Table 2 underneath gives an overview of studies that specifically investigated pore structure and volume.

Table 2: Porosity studies done with fuel cells

Author	Key Remarks and Findings	Pore analysis technique(s)
Uchida et al., 1995	-Primary pores remain unchanged as ionomer content is increased while the secondary pore volume decreased linearly. - Ionomer cannot reach/penetrate the primary pores due to the size of the ionomer, and therefore and therefore Pt existing in these pores cannot be considered to contribute to the reaction. -PEMFC performance increased due to the larger pore volume (macro pores) increasing the interface between Pt and ionomer inside agglomerate.	N_2 Physisorption & Hg-Porosimetry
Lee et al., 1998	-An inverse proportionate relationship between the increase of Nafion loading and meso pore volume. - The higher the Nafion loading, the narrower the pore volume distribution. -Thin Nafion films formed around agglomerates is the primary source of PEMFC diffusional losses.	N2 Physisorption & SEM
Shin et al., 2002	-Colloidal inks produce larger agglomerates and ionomer fills these pores, resulting in a decrease in secondary pore volume whilst primary pores remain unchanged. -Solution inks dissolve ionomer and results in blocking pores, thus decrease primary pore volume.	Hg-Porosimetry
Xie et al., 2004	-Addition of Pt and PtCr to carbon supports, decreased primary pores and the opposite effect observed when adding PtRu. -Boiling CCMs in H_2SO_4 significantly increased pore volume due to the expansion and contraction of the CL when boiling and drying. -Increased Nafion loading, decreased primary and secondary pores.	Hg-Porosimetry
Chisaka & Daiguji, 2006	-Primary and secondary pores decreases as glycerol quantities in inks are increased	N_2 Physisorption
Malek et al., 2007	-The Ɛ of solvents used to formulate catalyst dispersions influences agglomerate pore structure. -As Ɛ increases, primary pore volume decrease and secondary pore volume increase. This is because primary carbon agglomerates in high polarity solvents are more condensed.	Course-grained molecular simulation
Park et al., 2007	-GDE pore volume analysis shows that the GDL greatly influences the measured pore volume and is important to be considered when analysing CL PSD. -An increase CL fabrication temperature significantly increases secondary pore volume and has a negligible effect on primary pores. -Due to an increase in pore volume, mass transfer resistance decreased and therefore improved overall PEMFC performance.	Hg-Porosimetry

Chaparro et al., 2010	-Electro-sprayed CLs preserves porosity as compared to airbrushed films of which pore volume significantly reduced when ionomer content is increased.	N2 Physisorption & Hg-Porosimetry
Suzuki et al., 2011	-Majority of the carbon black pores are <100 nm -Primary pore volumes decrease with an increase in ionomer content which is attributed to the ionomer blocking pores in agglomerates. -Increase in porosity and pore width resulted in an increase in performance, but too high ionomer content (above its optimum value) causes the inverse as mass transport is limited. -CLs with low pore volume have limited reaction sites and are more prone to flooding due to water build-up.	N2 Physisorption & SEM

2.5.4 Rheology

Fluid materials are systems which flow when subjected to stress. Non-homogenous fluids containing more than one phase such as solid particles dispersed in a liquid are considered structured fluids, since their rheological behaviour is dominated by the interactions of their constituents. Structured fluids do not obey a simple linear relationship between applied stress and flow, also known as Newtonian fluid behaviour. It is more commonly found that material viscosity drops with an increase in shear stress. This phenomenon is known as shear thinning. At high solid concentrations, if the low shear rate viscosity region completely disappears then the material is yielding. Materials which do not have a yield stress but behave non-linear are classified as pseudo-plastic. Pseudo-plastic materials flow instantaneously upon application of stress but also display shear thinning behaviour (Franck, 2015). Stampino et al., 2009 suggested the use of pseudo-plastic shear thinning catalyst ink slurries as it is commonly used for laboratory and industrial applications. They optimised the ink composition in terms of selecting a suitable rheology by changing the surfactant, catalyst mass and solvent concentrations to be used for doctor blade application. Rheology was also then used to maintain a consistency in ink fabrication by measuring rheological behaviour, using a rotational rheometer for additional tests conducted.

The rheometer measures shear stress (τ) as a function of shear rate (γ) according to the following:

$$\tau = \kappa.\gamma^{n} = (\kappa.\gamma^{n-1}).\gamma \qquad (3)$$

The apparent viscosity(η_a) could be expressed as the following:

$$\eta_a = \frac{\tau}{\gamma} = \kappa.\gamma^{n-1} \qquad (4)$$

Here κ refers to the rheological consistency index. The exponent n can be calculated by linearizing Equation 4 and doing a logarithmic plot of kinematic viscosity versus shear rate. For Newtonian flow, $n = 1$ and the apparent viscosity is independent of γ. A pseudo-plastic or shear thickening fluid, where $n > 1$, viscosity increases with an increase in shear rate. For a shear thinning fluid, where $n < 1$, viscosity decreases with an increase in shear rate. A

value of n closer to 1 roughly suggests a better dispersion situation resembling behavior closer to Newtonian. The findings of Huang et al., (2011) favour the use of rheological studies for catalyst ink dispersion characterisation, as a consistency is achieved relating ink dispersion compared to MEA performance.

2.6 Ink Mixing

Dispersion is the process of breaking-up or reducing aggregates and agglomerates of pigment particles to a desired particle size. By reducing particle size, the total surface area of the material is increased and thus a higher percentage of atoms can interact with other matter. As a result, dispersion reduces the quantity of nano-materials needed to achieve the same effects. As most nano-materials are costly, this aspect is of high importance for the commercialisation of product formulations containing nano-materials (Hielscher, 2007).

Nanomaterials such as catalysts are produced in the dry form. For further processing, these materials therefore need to be mixed into liquid formulations. This wetting stage is where nanoparticles usually form agglomerates. Therefore effective methods of de-agglomeration and dispersion are required to overcome these bonding forces. The most used laboratory and industrial mechanical dispersion techniques are shear stirring, milling and ultra-sonication (Paipetis & Kostopoulos, 2013).

Understanding mixing conditions is vital for reproducible ink formulations. In order to scale up processes, mixing conditions require adjusting. Therefore understanding the influence mixing has to ink processing is a vital industrial tool.

2.6.1 Bead Milling (BM)

Milling is primarily used for the size reduction of solids which are suspended in fluids. Large scale milling generally has low throughput rates. Dispersion during milling is due to compressive and/or shear stress action mechanisms. Bead Mills (other common names are ball mills, pearl mills, etc.) is a type of milling which produces high impact milling. They usually consist of a grinding chamber with hardened beads (e.g. zirconium dioxide, steel, etc.) which is supported by a stirring mechanism such as a rotor. Ball milling is a mechanical dispersion method which generates local high –impact areas between the balls resulting in a random crushing of the materials. These mills either have a vertical or horizontal grinding chamber filled with a certain level of beads which is used to enhance grinding action. Bead loading is the percentage of free chamber volume nominally occupied by the beads which is generally in the range of 80-90%. If bead loading is too high, interference among grinding elements would prevent the establishment of effective velocity profiles. If loading is too low, shear forces and frequency of collision will not be sufficient to provide good disintegration (Harrison, 1993). Much higher quantities of dispersed samples can be produced by ball milling compared to other dispersion techniques making the technique very practical.

This technique is commonly employed industrially for shortening and particle de-agglomeration of carbon nanotubes (CNT's). Prolonged milling could transform CNT's into other forms of nanoparticles or even amorphous graphite. For particle dispersion, ball milling could be used for grinding in both dry and wet states.

Figure 11 represents the working principle and major action mechanism behind ball milling (Paipetis & Kostopoulos, 2013). The dispersion medium is agitated, causing the sliding and collision of beads against each other and the sides of the vessel. This action creates impact and shear forces which results in breakage and de-agglomeration of nanoparticles. The main controlling parameters for bead milling are rotation speed, mixing time and bead diameter. High impact speeds and large bead diameters will result in higher shear and impact forces. Higher energy forces could cause undesirable damages to the solid particles. Therefore it is imperative to understand the parameters involved when trying to obtain a desirable outcome. The kind of beads used for milling and their hardness might influence the efficiency of mixing and quality of the final suspension. The efficiency of a ball mill is also usually dependent on factors such as temperature, surface tension and viscosity of the dispersion media. Therefore ball mills are often supplied with a cooling/heating system (Paipetis & Kostopoulos, 2013).

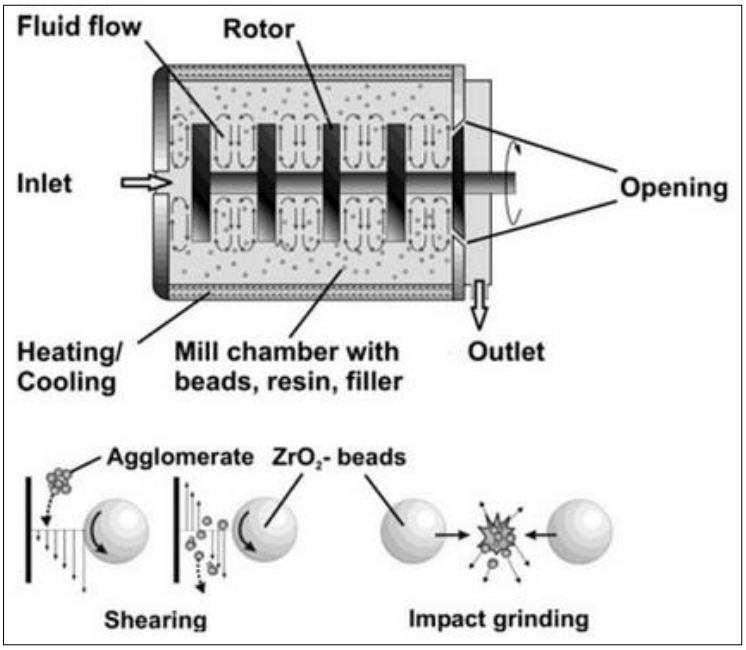

Figure 11: Bead mill and basic schematic of its main action mechanisms (Paipetis & Kostopoulos, 2013).

2.6.2 High Shear Mixing/ Stirrers (HSS)

High shear mixing also known as high intensity mixing are important in industries where emulsifying liquids, dispersing solids into liquids, breaking down aggregates and other applications where low speed agitation is not adequate (e.g.: processing of lubricants; silicone gels; polymer slurries; asphalt; paint primers; etc.). HSS use motors that operate between 3600 rpm to 10 000 rpm. High level shearing is produced through hydraulic forces when the mixing head rotates at high speeds, and mechanical forces split particles as they come into contact with the edges of mixing blades (Mixing & Blending Handbook, 2001). A typical example of a HSS is a high-speed disk disperser, as seen in Figure 12. This device consists of a circular-saw-type disk mounted onto a vertical shaft. The nature of the dispersion process is ultimately dependant on the viscosity and density of the mixture. At low solids content and low viscosity, flow is turbulent and impact processes are important

whereas, at higher solids content and high viscosities, flow is laminar and shear dispersive processes will be dominant (Tadros, 1987).

(a) 

(b) 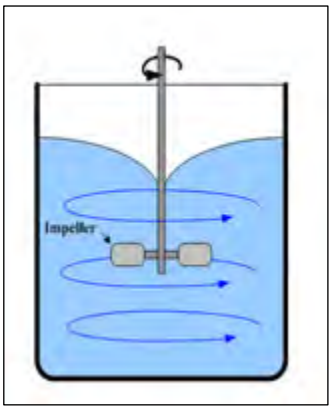

Figure 12: (a): Example of a High Shear Mixer and (b): Schematic of the mechanism of mixing using a HSS. During the mixing process, the blade creates a vortex that draws the mixture contents towards the blades and the blade mechanically disperses agglomerates (Ross, 2015).

2.6.3 Ultrasonic Homogenisation (UH)

Ultrasound is a tool very commonly used in the processing of nano-materials. Ultrasonic cavitation in liquids are used in various applications such as: chemical reactions by generating free radicals; accelerating chemical reactions by facilitating mixing of reagents; polymerising and depolymerising by temporarily dispersing aggregates or permanently breaking chemical bonds in polymer chains; and producing uniform dispersions of nano-sized or micron-sized materials (Hielscher, 2007).

A colloidal solution (an emulsion of two non-immiscible liquids) can be mixed by subjecting the solution to ultrasonic radiations. An ultrasonic mixer consists of one or more transducers vibrating at certain frequencies (Conley, 1996). A basic schematic of an UH setup is shown in Figure 13. Ultrasonic wave mixing can be used to enhance nano-scale dispersion by the destruction of agglomerates owing to the unique action of ultrasonic waves (Ryu et al., 2001).

In industry, high-intensity ultrasound is used to process liquids for the purpose of emulsifying; mixing; de-agglomeration and dispersion of particles. During high intensity sonication, sound waves propagate into the liquid media and results in alternating high pressure (compression) and low pressure (refraction) cycles. During the low pressure cycle, ultrasonic waves create minute vacuum bubbles in the liquid media. When vacuum bubbles attain a volume at which they are no longer able to absorb energy they violently collapse during a high pressure cycle. This process is known as cavitation. Cavitational collapse produces intense local heating (~5000 K); high pressures (~1000 atm); vast cooling rates (>10^9 K/s) and liquid jet streams (~400 km/h). The intensity of acceleration is one of the most important factors influencing the transformation of fractions of energy into cavitation. A greater acceleration generates higher pressure differences and this in turn, increases the probability of generating vacuum bubbles instead of waves propagating through the liquid (Suslick, 1998).

During dispersion and de-agglomeration, liquid jet streams resulting from cavitation cause particles to collide with one another at very high velocities. This breaks van der Waals forces in agglomerates and in some cases, breaks down primary particles. Larger particles undergo surface erosion and particle size reduction (Hielscher, 2007).

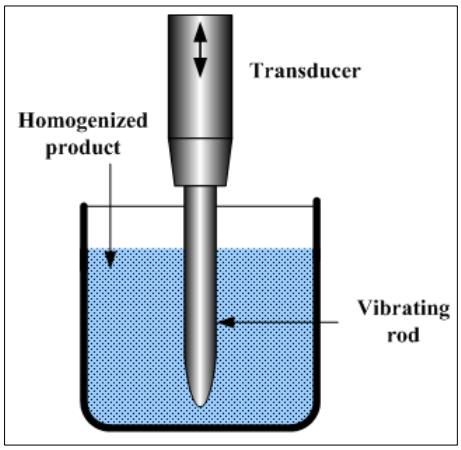

Figure 13: Schematic of an ultrasonic homogeniser showing all the basic components (Kopeliovich, 2015).

In conclusion: A perfect blend consists of an even distribution of its constituents in their primary un-agglomerated particle size. A method to evaluate the effectiveness of the blend is therefore to assess this property (Baines & Cope, 1968).

2.6.4 Ink dispersion for MEA preparation

Many reports have been based upon fabrication techniques involving catalyst components and CL preparation, but very little is mentioned about the intermediate mixing processes. Zhang, 2008 proposes that in order to ensure that nano-scaled catalyst particles are in contact with the other catalyst ink components, the catalyst ink should be stirred or ultrasonically dispersed. Below is a table showing a review of literature pertaining to mixing methods used during catalyst ink preparation. The most important studies and their highlights are discussed below.

Table 3: An overview of literature pertaining to mixing methods used during fuel cell catalyst ink preparation

Author (s)	**Mixing method**	**Preparation details**
Wilson et al., 1995	Magnetic Stirring	No details.
Uchida et al., 1995 & Uchida et al., 1998	Ultrasonication	Catalyst powder was dispersed in a colloidal solution of Nafion by ultrasonic treatment.
Chun et al., 1998	Mechanical stirring + Ultrasonication	Pt/C mechanically stirred in a solvent for 30 min, and then PTFE added and further dispersed for 30 min by sonication.
Fischer et al., 1998	Ultrasonic bath	C/Pt was ultrasonically dispersed in Nafion until the mixture became viscous.

Cheng et al., 1999	Ultrasonication	No details.
Song et al., 2001	Unknown	Formulated a "homogeneous mixture" before ink application.
Qi & Kaufman, 2002b	Ultrasonication + mechanical stirring	Ink mixture sonicated for 1 hour, and then kept under stirring until ink was used for CL formulation.
Hsu & Wan, 2003	Ultrasonic probe	Ink was hand mixed whilst Nafion was slowly added and subsequently the final mixture was ultrasonically treated.
Shin et al., 2002	Ultrasonication	No details.
Li & Pickup, 2003	Ultrasonication	Sonication for 30 min.
Frey & Linardi, 2004	Magnetic stirring + Ultrasonication	No details.
Kim et al., 2004	Ultrasonication	Sonicated for 30 minutes.
Yang et al., 2004	Magnetic Stirring	Nafion + Pt/C mixed by magnetic stirring for a few hours.
Benıtez et al., 2005	Ultrasonic bath	Ink mixture sonicated for 30 minutes.
Fernandez et al., 2005	Ultrasonic bath	No details.
Song et al., 2005	Mechanical stirring + Ultrasonic bath	Mechanically mixed then sonicated for 10 min.
Chisaka & Daiguji, 2006	Mechanical stirring + Ultrasonication	Magnetic stirring until viscous then sonicated for 15 minutes.
Rajalakshmi & Dhathathreyan, 2007	Ultrasonication	Sonicated until ink was well dispersed.
Xu et al., 2007	Ultrasonic bath	Ultrasonic bath for 6 hours.
Park et al., 2007	Ultrasonication	Pt/C dispersed in Nafion solution ultrasonically then solvent was added and further dispersed for several minutes.
Zhao et al., 2007	Ultrasonic probe	A pore forming agent + Solvent + Pt/C was ultrasonically mixed for 15 minutes, and then Nafion solution was added and further sonicated for 30 minutes.
Stampino et al., 2009	High shear stirring + Magnetic stirring	High shear stirred for 15 minutes then magnetic stirred for 1 hour.
Wannek et al., 2009	Ultrasonication	Sonication for 20-40 minutes.
Chaparro et al., 2010	Ultrasonic bath	Ink dispersed by sonication for 2 hours.
Kim et al., 2010	Ultrasonication	Sonication for 1 hour.
Therdthianwong et al., 2010	Ultrasonication	Ink mixture sonicated for 2 hours.
Cho et al., 2011	Magnetic stirring + High shear stirring	Catalyst ink was stirred for 30 min with a magnetic bar and then homogenised using a high shear stirrer.
Huang et al., 2011	High shear stirring	Ink mixed inside a high shear mixer for 1.5 minutes.
Millington et al., 2011	Ultrasonic bath	Ultrasonic bath at a power setting of 8 W.

Suzuki et al., 2011	Bead milling	The ink mixed using a churn for 30 min, and then small balls of zirconia were and the ink was further mixed for 1 min.
Yoon et al., 2011	Ultrasonication	Sonicated for 30 minutes.
Jung et al., 2012	Ultrasonication+ Magnetic stirring	Sonication whilst adding Pt/C to Nafion + Solvent solution then magnetic stirred overnight.
Tanuma & Kinoshita, 2012	Ultrasonication	No details.
Felix et al., 2013	Ultrasonic Probe	Ink sonicated for 5 minutes at 20 kHz and 40% power input.
Ngo et al., 2013	Ultrasonication	Mixed by sonication for 48 hours.
Su et al., 2014	Ultrasound	Ink sonicated for 1 hour.
Yudianti et al., 2014	Mechanical stirring + Ultrasonication	Nafion + solvent stirred for 15 minutes then Pt/C slowly added and then ink sonicated for 2 hours.
Liang et al., 2015	High shear stirring + Ultrasonic bath	Ink mixed in a HSS then in an ultrasonic bath.

Uchida et al., (1998) showed that when using two different mixing methods a performance difference is achieved. These methods are illustrated in Figure 14. In the first method ionomer was poured into a solvent forming a colloidal solution. The supported catalyst was then mixed with the colloidal solution; the mixture was then transformed into a paste by coagulation where ionomer chains were adsorbed on the catalyst by ultrasonic treatment. A second process was used to improve the paste process. The catalyst was first mixed with the solvent. The ionomer was then added (drop-wise) to the mixture whilst stirring. Using ultrasonic treatment the ink mixture was turned into a paste as with the previous method and spread over carbon paper.

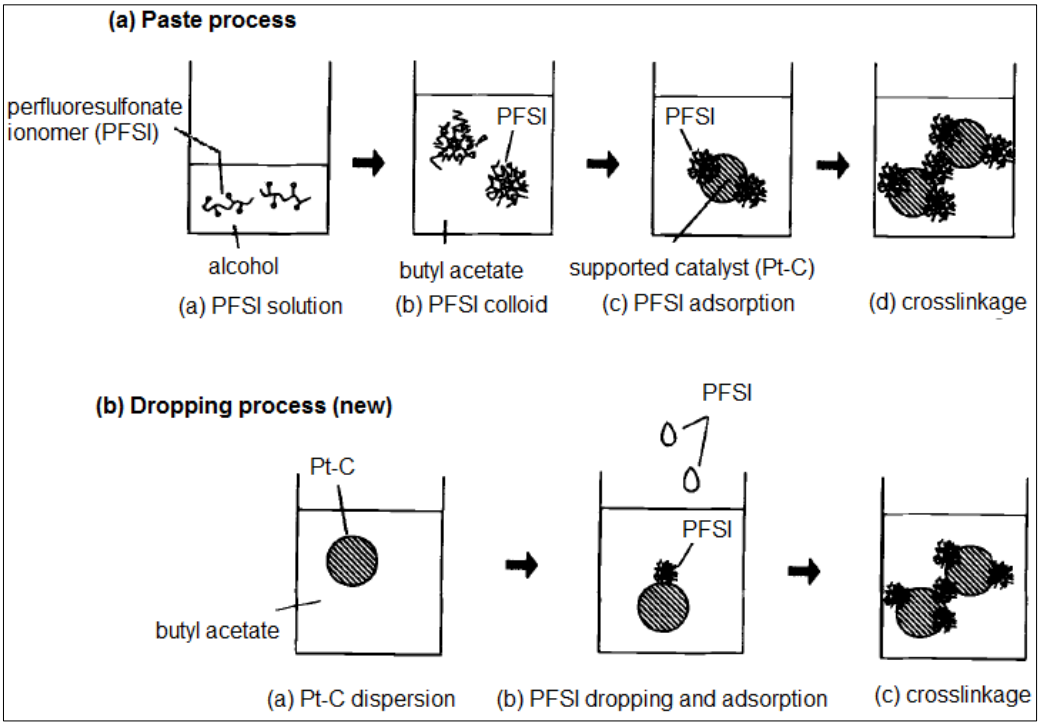

Figure 14: Preparation process of the catalyst layer (Uchida et al., 1998).

An increase in reaction area and a decrease in internal resistance were observed using the dropping method. Polarisation curves depicted the performance improved when using the dropping method. The authors suggest that it might be due to a reduced ionomer thickness on catalyst particles owing to the high level of dispersion achieved in the dropping method.

Lindermeir et al., (2004) studied the effect of different mixing techniques on carbon particle size for MPL preparation. Suspensions were prepared by intense magnetic stirring, ultrasound bath treatment or by using of a computer controlled wet-ball-mill. The authors noted the following:

i. Mixing by magnetic stirring is the simplest method to disperse the carbon but controlling the mixing parameters is difficult and the specific power input is low.
ii. Ultrasound enhances mixing due to the increased power input, but the results are dependent on parameters like the frequency and the geometric arrangement of the ultrasound source and therefore complex to adjust.
iii. Ball-milling is used in a vast scale of industrial applications; it is a well investigated mixing method and is simple to scale-up.

Particle size analysis (PSA) indicated that smaller particles re-agglomerate during the ultrasound treatment. This is attributed to cavitation events causing high tensions in the transient bubbles. This leads to particles breaking, however, ultrasonic treatment can enlarge particle agglomerates by an enhanced mobility of the solid compounds in the suspension. Although magnetic stirring produced smaller particle size, mixing was not effective due to broad distribution curves. When bead milling, larger agglomerates are destroyed efficiently and distribution becomes narrower. The extended milling duration causes only a slight continuation of size reduction. The authors concluded that milling is favourable amongst the other investigated mixing techniques as more stable inks were produced.

Lim et al., (2006) investigated the effect of using two different catalyst ink dispersion methods on the morphological changes in catalyst layer for DMFCs. In this case, unsupported PtRu black was dispersed by either UH or BM. Sonication was done for 1 hour and BM process was done for 2 hours using zirconia beads. The inks were applied to the MPL coated GDL using a spray gun. Their key findings were as follows:

i. X-ray diffraction showed that catalyst particles in the CL have a crystallographic ordered structure and have larger agglomerates compared to the unmixed PtRu powder.
ii. Shown in Figure 15, BM made catalyst particles form larger agglomerates as compared to ultra-sonication; observed during PSD and SEM.

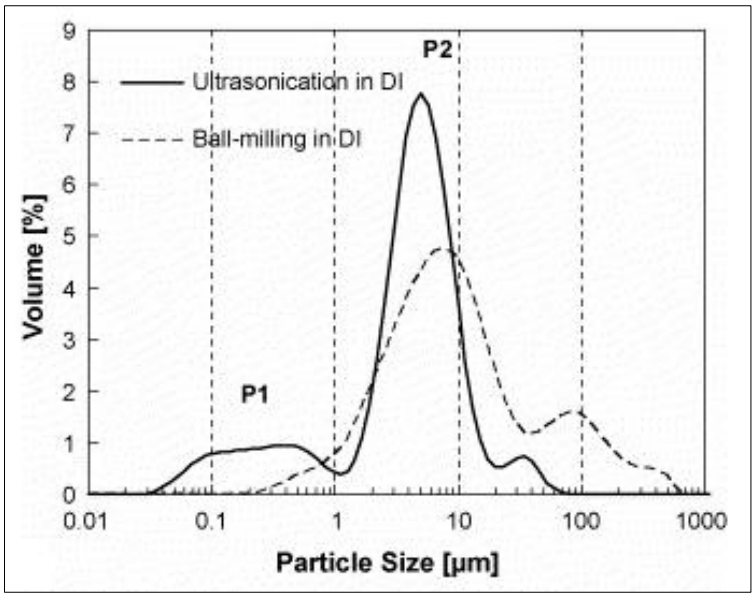

Figure 15: Comparison between particle size distributions of inks prepared using ball-milling and ultrasonication (Lim et al., 2006).

iii. In-situ performance showed MEAs prepared using BM having slightly higher current densities in the kinetic controlled region compared to UH, and the inverse for the diffusion controlled region.
iv. No difference in catalytic surface area was observed in the two mixing methods.

Wannek et al., 2010 investigated the use of high shear stirring; magnetic stirring and ultrasonic mixing on the properties of CLs and FC performance. Their results indicate ultrasonic mixing was the best in terms of producing: (i) Catalyst inks with narrow particle size distributions; (ii) high ink stability (shown in Figure 16); (iii) homogeneity of catalyst layer coating. However no influence of mixing techniques on overall fuel cell performance was observed.

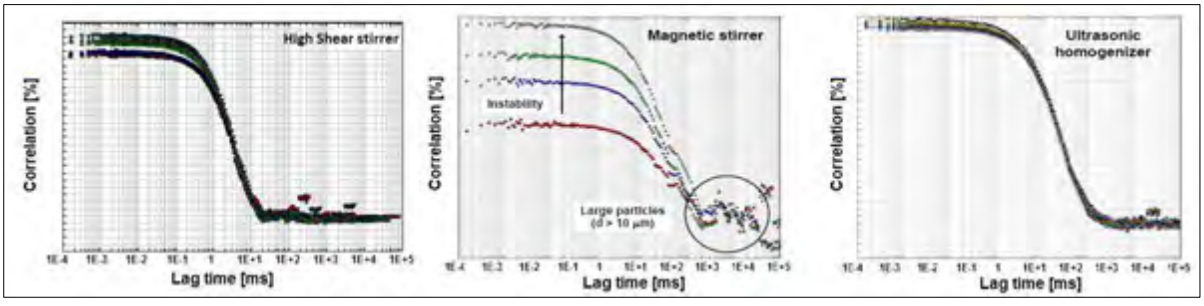

Figure 16: Photon cross correlation curves showing the stability of catalyst inks prepared with different dispersing techniques (adapted from Wannek et al., 2010).

Pollet & Goh, (2014) investigated the effects of ultrasound and HSS on performance of catalyst ink. They concluded the following:

i. Mixing is essential for homogenous catalyst ink.

ii. High ultrasonic power input reduces catalyst electrochemical surface area (ECSA); owing this to Pt delamination (as shown in Figure 17); agglomeration; ablation or dissolution of Pt nanoparticles.
iii. Short ultrasonic times (30 minutes) produced homogeneous inks and ECSA was higher compared to lengthened dispersion times (120 minutes)
iv. Performance of the ink using HSS was considerably lower compared to ultra-sonication.

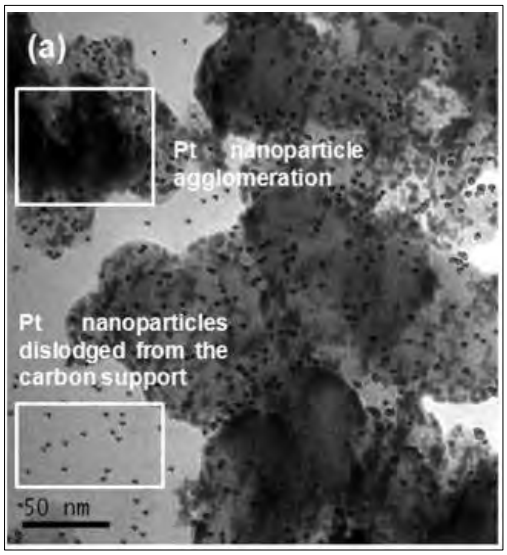

Figure 17: TEM image of a catalyst sample irradiated (20 kHz) for 30 min at 6.70 W showing the delamination of Pt nanoparticles (Pollet & Goh, 2014).

The authors suggest that mixing parameters should be carefully chosen and factors such as ink temperature, mixing power input and ink rheology should be monitored for reproducible ink formulations. It should be noted that the HSS was only conducted at one condition- 120 minutes at 19 000 rpm, whereas UH was evaluated at three different conditions.

Literature pertaining to catalyst ink/ MEA preparation was rigorously investigated, as shown in Table 3. Very little is usually discussed around the areas concerning ink formulation, especially the mixing parameters. However, it is clear that majority of studies are conducted using ultrasonication. Although ultrasonic dispersive methods such as the probe and bath are both popular choices, mixing conditions vary throughout literature for example: reported mixing times range between 1.5 minutes to 48 hours. This is a huge time gap and is especially a matter of concern as catalyst ink processing is a vital stage during MEA fabrication. Not only does this impact the total MEA fabrication time, but also the resulting ink formulations. Some authors process ink using a series of mixing steps. This could also be energy intensive, time consuming and potentially reduce ink recovery. Thus, knowledge in this particular area could be invaluable for MEA preparation optimisation.

3. Project Objectives

The move toward PEMFC commercialisation is inhibited by comprehensive knowledge of CL functioning, predominantly due to its complexity. From here, the fabrication of the CL involves a number of processes, all of which have an effect on its resulting quality. Specifically, the effect of catalyst ink mixing is an area which lacks knowledge in the FC field. The significance of the mixing step; the way by which mixing disperses catalyst agglomerates and distributes Nafion ionomer; and its effect on FC performance, are some of the factors that are not well understood. Many mixing methods are available and majority of the time, mixing methods and parameters are chosen without effectively conducting experimental research. This study therefore serves to contribute some knowledge into the field of MEA fabrication, and also serve to be a starting point when considering high throughput MEA production.

Based upon the findings outlined in literature, the following objectives were formulated:

1) Develop a systematic characterisation protocol in order to evaluate CL quality and in-situ performance.

2) Based upon 1) establish the link between the mixing method, physical properties of the catalyst layer and in-situ MEA performance.

3) Determine the effect of the catalyst ink mixing parameters on the catalyst layer properties: morphology, porosity, ionomer structure and distribution.

Before partaking on the study, a number of in-house fabrication considerations have to be evaluated and in some instances altered. Some of which are solvent selection, spraying parameters, decal parameters and testing conditions.

4. Experimental Procedures

This section will detail the experimental procedures and outline the preliminary work conducted during the course of this study. Figure 18 is an outline of the complete MEA preparation up to testing.

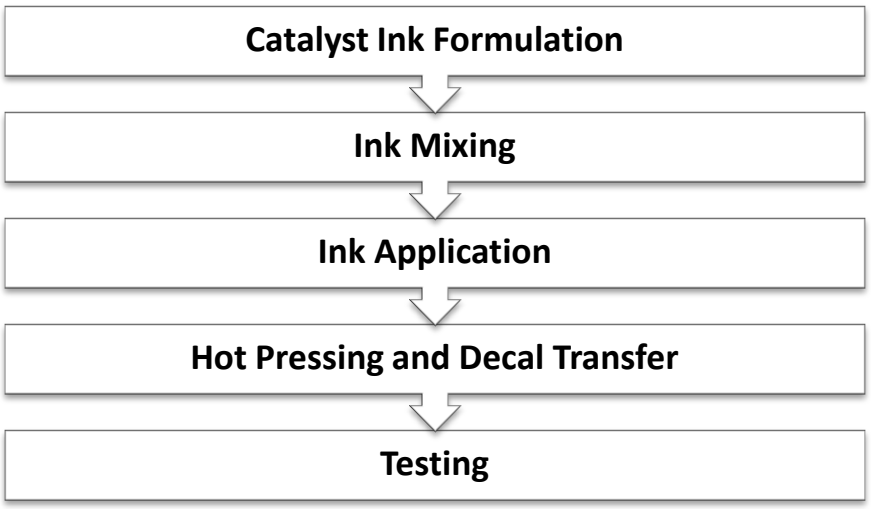

Figure 18: Outline of the MEA preparation procedure.

4.1. Catalyst Ink Formulation

Table 4: Chemical components and materials used during catalyst ink formulation and MEA preparation

Component	Description	Supplier
Catalyst	40 wt% Pt supported on Ketjenblack	Mintek
Solvent	Isopropanol (IPA) n-Propanol (NP) Water (H_2O)	Sigma-Aldrich
Solubilised Ionomer	15 wt % Nafion™ solution	Ion Power
Teflon	125 µm thick PTFE sheet	Fuel Cell Earth
Membrane	Nafion™ Membrane NR-212	Ion Power
GDL	SGL24BC	Ion Power

Table 4 and Figure 19 entail the list of components used during ink formulation. During the initial phase of the study, a high viscous catalyst ink (Isopropanol-IPA, Ethylene Glycol-EG and Glycerol-G) was used. This ink was later disregarded due to the following reasons:

- The addition of high viscosity solvents (EG & G) caused bubble formation during ink mixing and thereby greatly reduced catalyst ink recovery.
- The viscous ink caused frequent clogging of sprayer tubing thus more maintenance is required.
- Higher viscosity ink is more suited for GDL application.

The catalyst ink was prepared adding 0.9 g of catalyst powder to a 100 ml beaker followed by catalyst “wetting”. During wetting, 10 ml of H_2O was added, dropwise, to the surface of the catalyst in order to fully submerge the powder in water. This was to prevent combustion of the organic solvents added in the following step. The beaker was then swirled to ensure no dry catalyst powder remains. Subsequently, 10 ml of NP followed by 10 ml of IPA was added to the mixture. The beaker was then swirled to disperse the solvents into the ink mixture. The final component to add was 3.63 ml of the Nafion solution. This produced an ink mixture with an I/C ratio of 1.

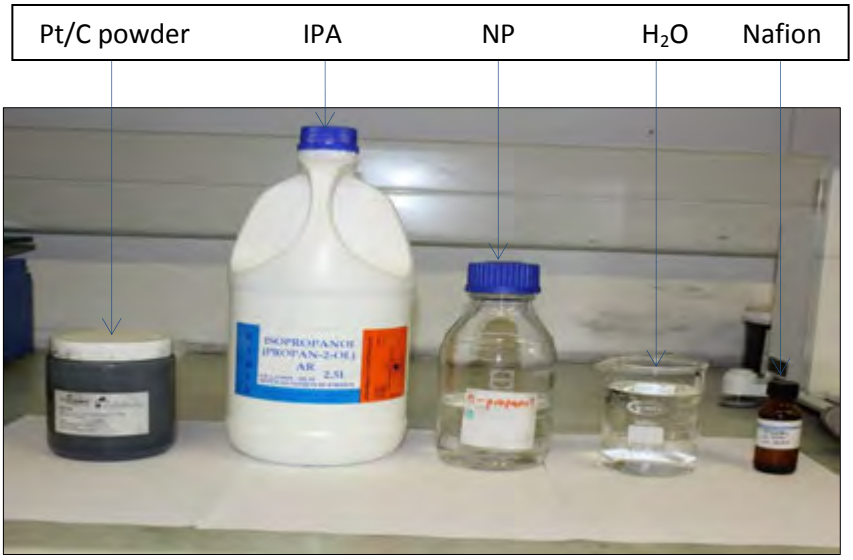

Figure 19: Catalyst ink components.

4.2. Ink Mixing

Catalyst ink mixing is the primary focus of this study. The choice of mixing equipment was done in such a manner as to investigate mixing procedures with completely different dispersing mechanisms. The choice of equipment was limited to what was available in-house. The following table represents the list of equipment used.

Table 5: Mixing equipment used through the duration of the project

Mixing Device	**Description**	**Specification**
Bead Mixers	Labcon Platform Shaker Model - SP-MP	50 rpm – 400 rpm
	Vortex Genie 2	600 rpm – 3200 rpm
High Shear Stirrer	Silverson High-shear mixer- L5M	0 rpm – 9900 rpm
Ultrasonic Horn	Bandelin SonoPlus-HD2200	HF-output of 200 W & 20 kHz

The influence of both mixing intensity and time was investigated in a 2 x 2 factorial design. For each mixing method, two points of mixing intensity and mixing time were selected such that it represents the extreme cases for each, see Figure 20. It is common for inks to be

dispersed for a period of 30 minutes and at this point, it is considered to be homogeneous, as stipulated by Pollet & Goh, (2014). They determined that mixing inks beyond 30 minutes might be detrimental to the ECSA of the catalyst. Catalyst ink formulation is a time consuming process so a shorter mixing time could greatly improve the efficiency of the process. The one extreme case for mixing time is therefore chosen to be 30 minutes, on the other extreme case, a mixing time of 5 minutes was chosen.

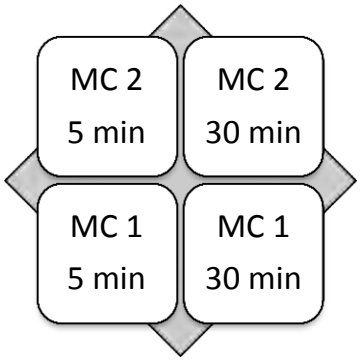

Figure 20: Shown above is the 2 x 2 factorial design matrix studied in each of the mixing processes. The horizontal axes represent the two mixing times (5 min and 30 min) and the vertical axes represent the two selected dispersive intensities (Mixing Condition -MC- 1 and 2; this will be specified in the later sections).

4.2.1. Bead Milling

During the process of BM, catalyst ink was transferred into a 100 ml plastic container, and 20 ml of 3.3 mm diameter zirconia toughened alumina beads were added (Figure 21).

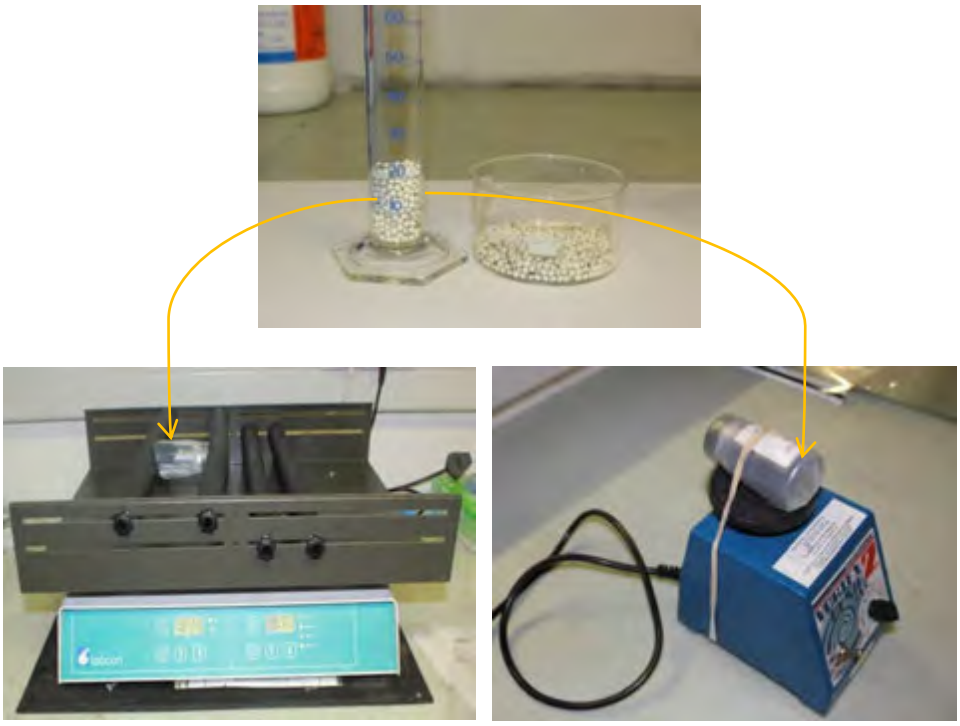

Figure 21: Top: Zirconia toughened alumina beads. Bottom-left: Bead mixing agitators, Labcon Platform Shaker and Bottom-Right: Vortex Genie 2.

The container was then tightly sealed and wrapped with Parafilm (in the event of ink spillage); then agitated using the Labcon Platform Shaker and Vortex Genie 2 for the 200 rpm and the 3000 rpm mixing condition respectively (Figure 22). Due to the difference in achievable rotation speed the two apparatus were used. It has been validated that both apparatus produce a similar agitation effect and therefore resulting formulation would not be affected by the change between apparatus. After mixing, the ink was recovered using a 1 mm diameter filtration sieve and funnelled through to the sprayer syringe. To optimise ink recovery a large sieve size, large bead size, a small bead volume and minimum ink transfer steps were used (Figure 23). Approximately 50 % of the initial ink volume is recovered after BM.

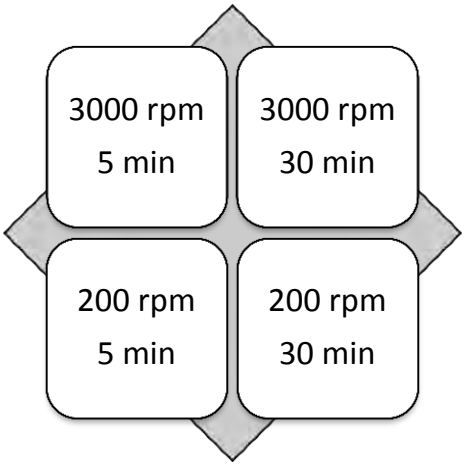

Figure 22: Shown here is the 2 x 2 factorial matrix for parameters studied using BM.

Figure 23: Left: Catalyst ink with beads transferred from container and ink collected in a syringe. Right: Beads collected after sieving.

4.2.2. High Shear Stirring

The high shear stirrer was set up by connecting the mixing unit and adjusting the Swiss Boy stand to an appropriate height. The mixing unit consists of a stationary outer casing together with an inner rotating shaft. After adding catalyst ink components to the beaker, it was then covered using Parafilm and is tightly sealed over the stirring rod to prevent the loss of ink solvents (Figure 24). For the matter of consistency and safety, the stirrer head was centred and raised 10 cm above the base of the beaker (Figure 26). After mixing according to the 2 x

2 factorial matrix (Figure 25), the catalyst ink was transferred into the sprayer syringe. During HSS, 80 % of the initial ink volume is recovered as some of the ink is lost to the head of the stirrer.

Figure 24: Experimental setup for high shear mixing during catalyst ink preparation. Shown here is the ink mixture contained in a 100 ml beaker on top of a Swiss Boy stand; with the mixing unit connected.

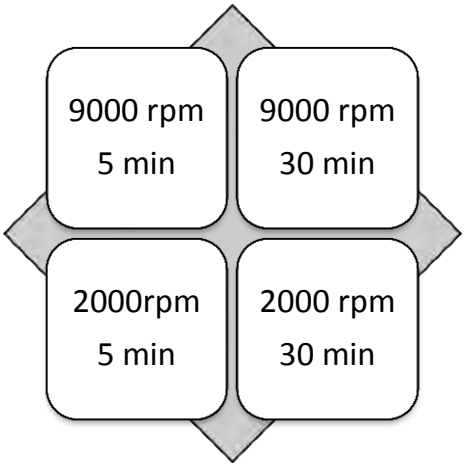

Figure 25: Shown here is the 2 x 2 factorial matrix for parameters studied using HSS

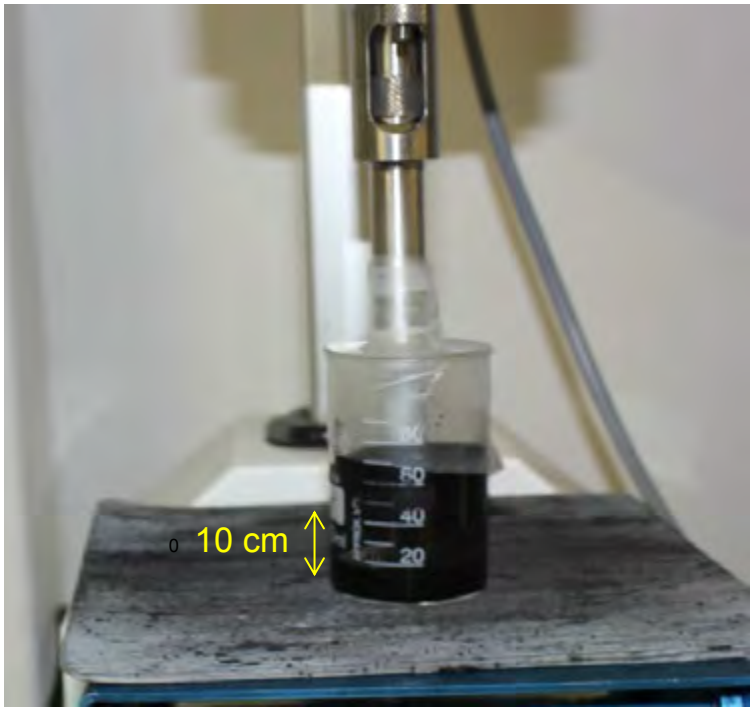

Figure 26: Equipment adjustment prior to mixing. Image shows the mixing unit raised 10 cm above the base of the beaker, with Parafilm connected to the stationary part of the mixing unit.

4.2.3. Ultrasonic Homogenising

After adding the components to the beaker, the catalyst ink is then set up to the UH as shown in Figure 27. The ultrasonic horn is raised 10 cm above the base of the beaker to avoid cracking during sonicating. The low mixing rate ink was dispersed at a 10 % power output and at a pulse mode cycle of 0.1 sec/0.9 sec of Active/Passive times respectively (abbreviated as: UH.1.10- x mixing time) (Figure 28). High intensity was mixed at 35 % power output and Active/Passive times of 0.4 sec/0.6 sec respectively (abbreviated as: UH.4.35- x mixing time). About 90 % of the ink is recovered during UH.

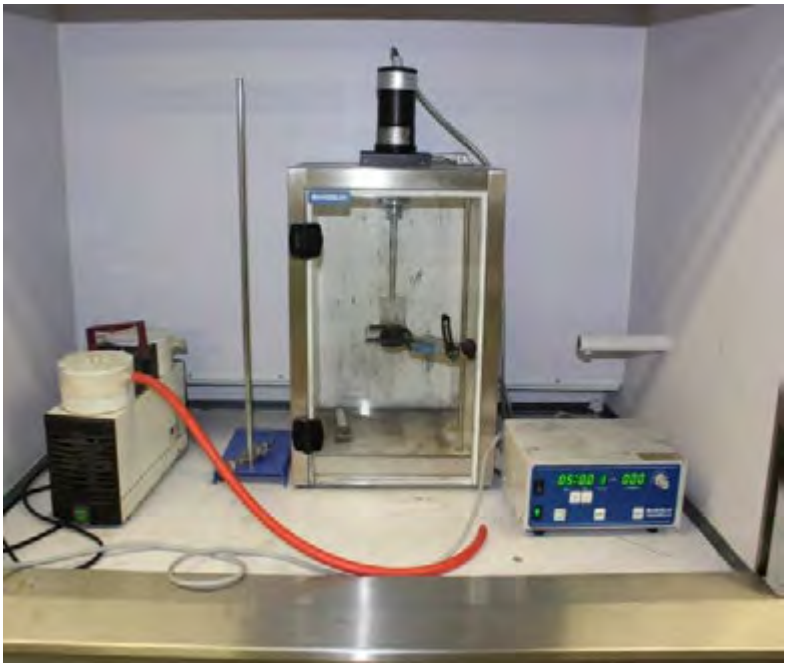

Figure 27: Experimental setup of ultrasonic homogenising during catalyst ink preparation.

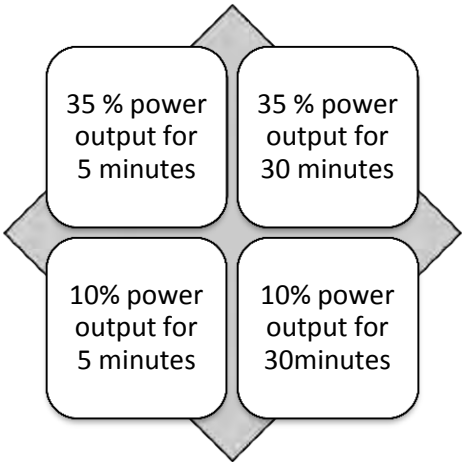

Figure 28: Shown here is the 2x 2 factorial matrix for parameters studied using UH

4.3. Ink Application

Immediately after mixing, the ink is transferred to the sprayer syringe. Spray coating is done using a PRISM Ultra-Coat 300 (Figure 29). The sprayer is programmed with conditions outlined in Table 6. The catalyst ink was sprayed onto 8 x 8 cm^2 PTFE substrates, coating four samples in a single run.

Figure 29: PRISM Ultra-Coat 300 sprayer used for catalyst ink application.

Table 6: Sprayer conditions

Sprayer Variable	**Details**
Sprayer nozzle height	60 cm
Heated table temperature	70 °C
Spray flow rate	1.02 ml/min
Spray speed	80 mm/s

During the spraying process (seen in Figure 30), the heating table is set to 70˚C. This was done to ensure that the catalyst ink coating was dry prior to the addition of a subsequent coat. An 8x8 cm^2 GDL was placed beneath the PTFE substrate. This was done to avoid ridges forming and to allow a vacuum to be drawn so that the substrate is flattened during spray process. The 8x8 cm^2 substrate is placed on top of the GDL and once all four substrates have been placed, the coating template is then positioned. In order to avoid ink from spreading, 8x8 cm^2 stencil plates are placed over each substrate.

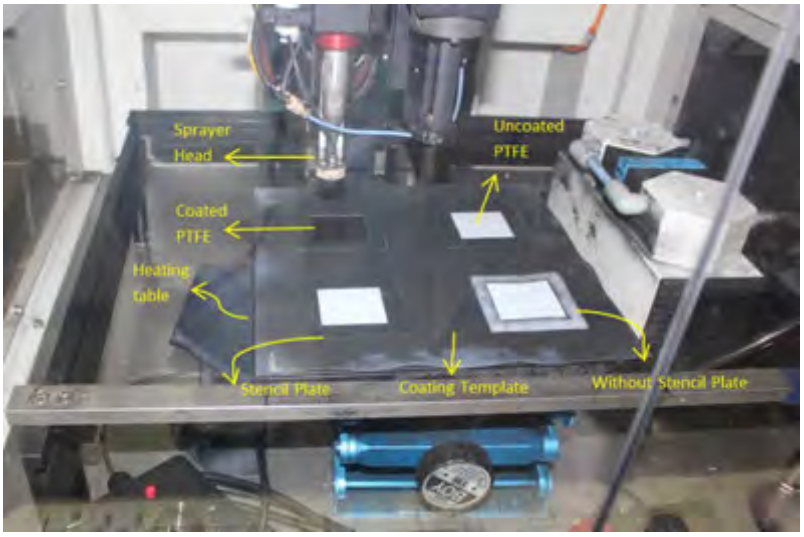

Figure 30: Schematic showing ultrasonic sprayer setup.

In order for the catalyst ink to be evenly spread across the substrate, the ink was sprayed in an in-house developed serpentine spraying pattern. The sprayer head moves in the motion as shown in Figure 31 where it starts at point A and moves to point B, then changes the direction of spray moving from point B through to point C. After the first sprayer motion (A-B) the CL coating is not completely uniform. Therefore, a bi-directional spray pattern was chosen to ensure complete coating of the sprayed substrate. Each substrate was coated either 3 or 4 times depending on the desired loading. Generally, anodic electrodes are coated 3 times, producing loadings in the range of 0.3 – 0.4 $mg.cm^{-2}$ and cathodic electrodes are coated 4 times, producing loadings in the range of 0.4 – 0.5 $mg.cm^{-2}$. After spraying, the coated substrates (shown in Figure 32) are labelled and air dried overnight, then stored in humidity controlled room until it is used.

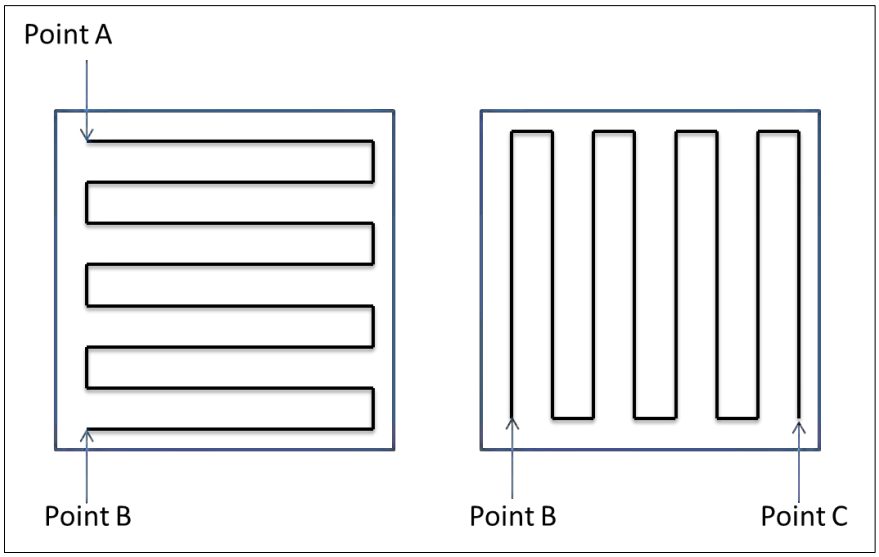

Figure 31: Serpentine sprayer-head-motion pattern used during spraying.

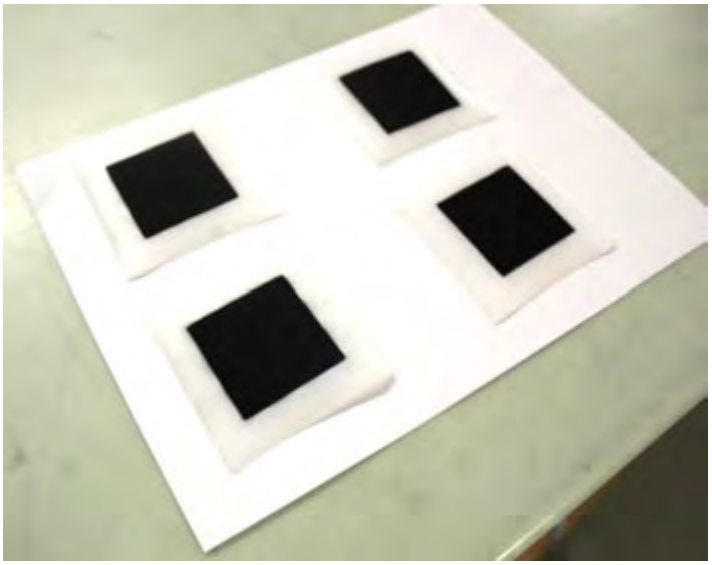

Figure 32: Sample of coated substrates after spraying.

4.4. Hot Pressing and Decal Transfer

When hot-pressing, the components are stacked in the order shown in Figure 33. The function of the big plate is to manage the rate of heat transferred to the sandwiched complex and to stabilise the complex within the press. The smaller plate is positioned for the placement of the other components and stabilises the sandwich. Filter paper cushions the sandwich and prevents melting of the PTFE. Blank PTFE serves as an additional cushioning layer. The anodic components are placed first and then a "*C.*" was labelled in the corner of the membrane to indicate the cathode side. Afterwards the membrane was placed, and then the cathode electrode and the remaining components are added to complete the complex.

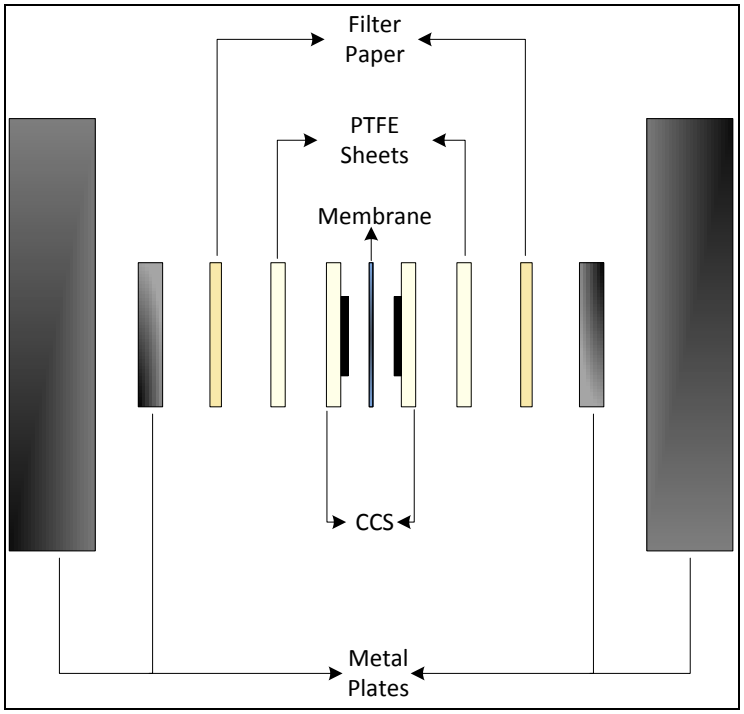

Figure 33: Hot-press complex containing the sandwiched electrodes (CCS in this figure).

Table 7 shows an outline of the hot-pressing parameters. After hot-pressing (setup shown in Figure 34), the heated complex was cooled for approximately 3 hours. Once cool, the sandwich was then removed and the CL was decaled from the PTFE substrate onto the membrane. The sandwich was placed under a ruler to apply some pressure whilst decaling takes place (Figure 35). Then each CL was carefully transferred by peeling away the PTFE substrate, and the result is the formation of a catalyst coated membrane (CCM).

Table 7: Outline of the hot-pressing parameters

Hot-pressing Parameter	**Details**
Temperature	130˚C
Pressure	20 MPa
Time	10 minutes

Figure 34: Hot pressing system used to prepare CCM's.

Figure 35: Peeling or Decal transfer process showing the second Teflon sheet being removed from the sandwiched complex. Here the substrate was gradually removed from the CCM using a metal plate to 'press-down' whilst peeling.

Figure 36 shows the residual CL after decaling in-house prepared CCM's, indicating that hot pressing pressure greatly influences CL transfer. Complete CL transfer is only obtained at a pressure of 20 MPa. As observed in literature, it is clearly not conventional to use hot pressing pressures greater than 15 MPa, however, a complete CL transfer is required to accurately examine the variables in this study, and to eliminate and additional aspects that could introduce variance. Thus, the pressure of 20 MPa was chosen as it produces 100 % CL transfer during decaling.

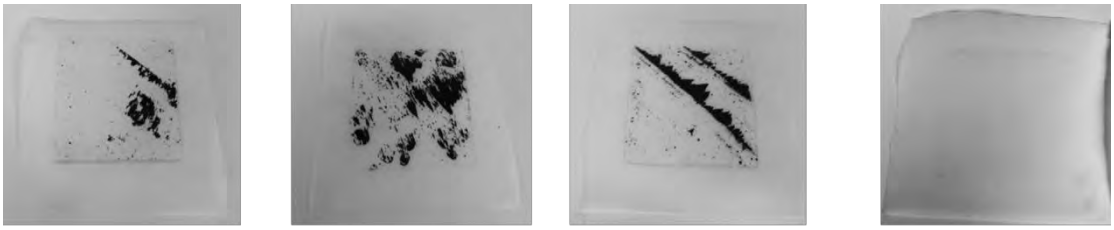

Figure 36: Residual catalyst layer on PTFE after decal at different pressures.

4.5. Characterisation

4.5.1. Particle Size Analysis

The particle size distribution of catalyst inks were characterised using a Mastersizer 2000 at the University of Cape Town, manufactured by Malvern Instruments. Particle size distribution is achieved by passing the dispersed sample through a measurement cell which uses Mie scattering to detect particle sizes (Malvern Instruments, 2006). The Mastersizer has capability of measuring particle size from 0.02 μm up to the millimetre domain and therefore is suitable to characterise catalyst aggregates. The measurement requires about 8 drops ($\sim 0.5\ ml$) of catalyst ink and each analysis run takes approximately 15 minutes to complete. The software is pre-programed to record five repeats of the analysed sample and tabulate the data which makes acquisition very simple.

4.5.2. Scanning Electron Microscopy

Catalyst layer morphology was characterised using FEI Nova NanoSEM 230, University of Cape Town. These are some of the NanoSEM features which make it suitable for CL characterisation: (i) it is equipped with a high resolution in-lens secondary detector; (ii) low voltage backscatter detector and (iii) an Oxford X-Max silicon drift energy-dispersive x-ray spectroscopy (EDX) detector. These together produce high resolution images with good contrast/image depth with the capability of producing high resolution elemental analysis (Wainwright, 2015). For every spray batch one sample of CCS and one sample of CCM were analysed.

Before CCS analysis, a 5 mm x 3 mm piece was cut from the bulk sample. When doing CCS cross sectional analysis the sample was first embedded in resin, died, sliced then polished to a mirror-like finish, and finally carbon coated to ensure good electrical conductivity. During CCM analysis, samples undergo cryofracturing after freezing in liquid nitrogen. This technique is much quicker than resin embedding but cannot be used to for the CCS as the Teflon would not break after freezing. For surface analysis both CCS and CCM samples were directly analysed.

4.5.3. Pore Volume Analysis

4.5.3.1. N_2 Physisorption

N_2 Physisorption experiments were measured with a TriStar II 3020 Version 2.00 by Micromeritics, University of Cape Town. Samples measuring 5 cm x 5 cm were cut up into strips and placed into a sample tube for testing. Prior to adsorption catalyst containing samples (CCS and CCM) was degassed at temperature of 110 °C for 12 hours. Both Teflon and N212 membrane were tested as blanks and the pore volumes were found to be negligible.

4.5.3.2. Hg-Porosimetry

Mercury intrusion porosity was measured using an AutoPore IV 9500 V1.09, University of the Western Cape. For each run, a 5 cm x 5 cm catalyst coated sample was analysed. The input Hg parameters were 130° for contact angle, 485 $mJ.m^{-2}$ surface tension and 13.5 $g.ml^{-1}$ density; and mercury filling was done at a pressure of 34.4 kPa.

4.5.4. In-Situ Performance

Fuel cell tests were conducted in a Fuel Con Evaluator C50 LT station. The testing station is equipped with an internal humidifier, temperature and pressure control, electronic flow and electronic load management allowing modular fuel cell testing. The system is equipped with an in-house developed script which is coded to run all the testing procedures sequentially.

4.5.4.1. Operating Conditions

The prepared CCM was placed into a Baltic fuel cell fixture (shown in Figure 37), sandwiched between two 5 cm x 5 cm GDLs. A die cutter was used to punch holes into the corners of the membrane so to accurately fit the CL in alignment with the flow field. The cell fixture was then sealed and connected to the testing station. The cell was pressurised to 4.8 bars and then undergo a leak test. During this, the system was pressurised with nitrogen gas by closing the outlet valves. Subsequently, the N_2 flow was closed and the system pressure drop was monitored. A leak is detected if pressure drop is greater than 0.07 bars over a period of 10 minutes (US DOE, 2007). If a leak is detected, troubleshooting needs to be done. The test is not allowed to commence without fixing the leak (e.g. sealing gasket, cell placement, gas line leaks etc.). The fuel cell was then set to the conditions as shown in Table 8 and testing commences once set point conditions equilibrates.

Table 8: Fuel cell testing conditions

Variable	**Set Point**
Cell Temperature / °C	80
Pressure / bars	1
Relative Humidity / % (both anode and cathode)	100
H_2 Flow / $l.min^{-1}$	0.39
Air Flow / $l.min^{-1}$	1.24
O_2 Flow / $l.min^{-1}$	1.24
N_2 Flow / $l.min^{-1}$	0.42

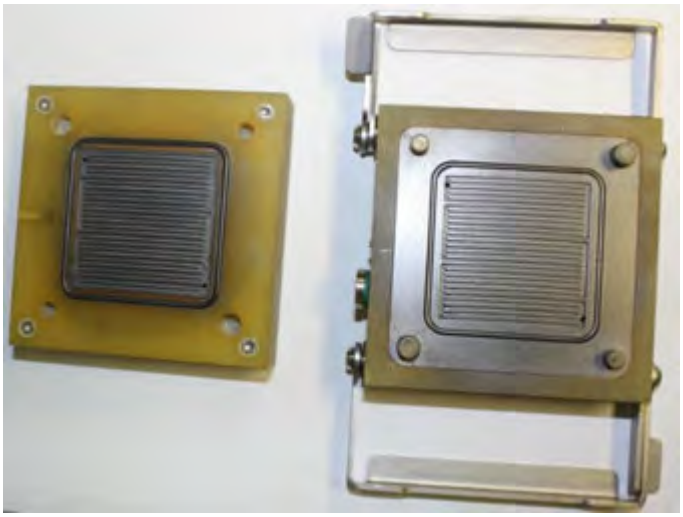

Figure 37: Baltic cell fixture used to test MEAs. Observe the serpentine flow field pattern and O-ring used to seal the cell.

4.5.4.2. Cyclic Conditioning

A newly fabricated fuel cell MEA has to be activated by incubation or breaking in so that the cell could perform at its peak performance. During conditioning, the voltage is swept between 0.3 V and 0.8 V whist the anode is kept at a stoichiometry of 1.5 and cathode 2. During this process, the MEA becomes hydrated and the CCM performance gradually increases up until a point where the performance plateaus, which happens after a period of about 2 hours (Yuan et al., 2012b).

4.5.4.3. Fuel Cell Polarisation

Polarisation curve testing commenced immediately after conditioning. The system is programmed to conduct two air and one oxygen polarisation curve. The tests are conducted at constant flow conditions at the flow rates specified in Table 8. The current step size during activation polarisation is 0.5 A, and 2 A in the ohmic polarisation region; which was chosen as such due to the relative sizes of each of these regions. After each set point, a 3 minute stabilisation period was allowed for the system to equilibrate and 3 repeat readings were recorded at each measurement point with 10 second intervals between.

4.5.4.4. Electrochemical Impedance Spectroscopy

In order to evaluate the relative contributions to the impedance of the fuel cell, electrochemical impedance spectroscopy (EIS) was conducted after polarisation curve measurement. Here the cell frequency was swept between 0.1 and 20 000 Hz. Impedance measurements were conducted at 100 $mA.cm^{-2}$ and 250 $mA.cm^{-2}$ whilst maintaining oxidant (air) and hydrogen flow rates as stated in Table 8.

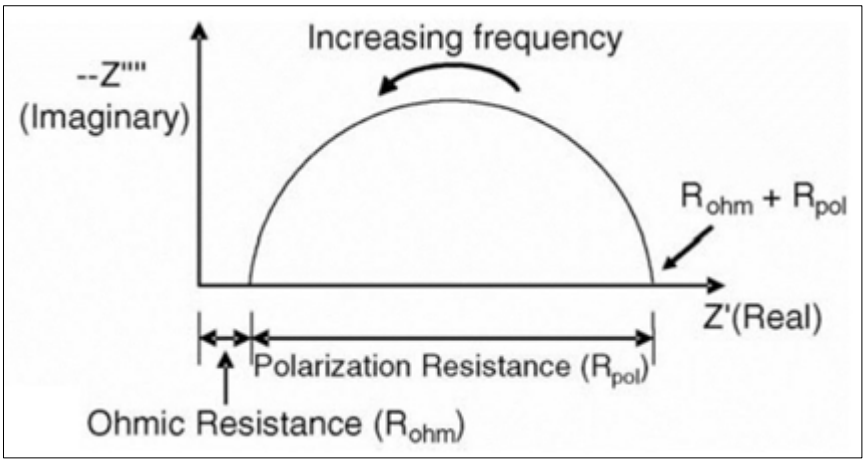

Figure 38: Nyquist plot showing the resistive contributions in PEMFCs (adapted from Cooper & Smith, 2006).

EIS involves applying a small sinusoidal voltage/current perturbation at steady state, measuring the resulting current/voltage and the phase angle. From this data, real and imaginary impedances could be calculated and plotted in a Nyquist impedance spectrum. This is the most common way of analysing impedance data in literature (Gomadam & Weidner, 2005). Using EIS, resistance and capacitance of each process in fuel cells can be separated according to the frequency dependencies (Jang et al., 2009). In this study, the concept of an equivalent circuit based analysis will be adapted to separate PEMFC resistances into diffusional losses, charge transfer resistance (polarisation resistance) and ohmic resistance, as shown in Figure 38.

At the high frequencies ohmic resistances dominate. The magnitude of this is determined by the high frequency intercept with Z'(Real). The factors contributing to the ohmic resistance are: membrane resistance; GDL, bipolar plate and contact resistances; bulk electronic and ionic resistance. Intermediate frequencies present charge transfer resistances and can be determined by the diameter of the arc. Charge transfer is dependent on the interfacial reaction kinetics, a consequence of the three phase reaction zone. At low frequencies diffusive resistances are dominant. These are due to mass transport resistance in the GDL, catalyst layer and the membrane (Gomadam & Weidner; 2005; Cooper & Smith, 2006; Wu et al., 2008; Jang et al., 2009). During FC performance tests, a well humidified membrane will result in very steep arcs ($\sim 90°$). At the conditions tested in this study, the anodic impedance can be neglected because the anodic kinetics are much faster than the cathodic kinetics (Jang et al., 2009).

4.5.4.5. Cyclic Voltammetry

The MEA's ECSA was determined by conducting cyclic voltammetry (CV) tests. CV measurement was done externally by connecting the terminals of a Metrohm AutoLab PGSTAT302N with a 10 A current Booster. Hydrogen flow rate was set to 0.15 $l.min^{-1}$ and the cathode was purged with nitrogen flowing at 0.42 $l.min^{-1}$. The cell voltage was monitored until the voltage dropped to 0.15 V. The CV measurement software Nova was opened and input parameters shown in Table 9 were set. When a voltage is applied, hydrogen is oxidised causing electrons to leave the electrode, generating a desorption charge. The ECSA was calculated by integrating the desorption charge over time (normalising it to the Pt

loading), and dividing this by the charge of monolayer hydrogen adoption on Pt of 210 $\mu C.cm^{-2}$.

Table 9: CV input parameters

Parameter	**Setting**
Upper vortex potential / V	0.90
Lower vortex potential / V	0.05
Start and stop potential / V	0.3
Step potential / V	0.001
Sweep rate / $mV.s^{-1}$	0.02
Number of crossings or repeats	2

5. Results

This section describes the results to evaluate the effect of mixing procedures of catalyst layer properties and in-situ performance using various characterisation techniques. After catalyst inks are mixed, particle size distribution is used to examine the influence comminution has on catalyst agglomerate size. Optical microscopy is used to determine CL quality and CL component distribution after application via ultrasonic spraying. Pore size distributions are measured using Hg-Porosimetry and N_2 Physisorption such that a large spectra of pore sizes could be evaluated. Finally, the prepared CCMs are tested in-situ by evaluation of polarisation (i-E) curves, impedance measurements and cyclic voltammetry.

The table below describes the abbreviations used. Mixing conditions and parameters where condensed to specifically denote the mixing condition, followed by the mixing intensity and at the end, the mixing time used. PSD is commonly used to describe both particle and pore size distribution, hence abbreviations where adapted here to distinguish between the two.

Table 10: Mixing conditions and abbreviations used in this section

Symbols used	**Meaning**
BM-200-5	Bead milling at 200 rpm for 5 minutes
BM-200-30	Bead milling at 200 rpm for 30 minutes
BM-3000-5	Bead milling at 3000 rpm for 5 minutes
BM-3000-30	Bead milling at 3000 rpm for 30 minutes
HSS-2000-5	High shear stirring at 2000 rpm for 5 minutes
HSS-2000-30	High shear stirring at 2000 rpm for 30 minutes
HSS-9000-5	High shear stirring at 9000 rpm for 5 minutes
HSS-9000-30	High shear stirring at 9000 rpm for 30 minutes
UH-1.10-5	Ultrasonication at a pulse mode cycle of 0.1 sec/0.9 sec at 10 % power input for 5 minutes.
UH-1.10-30	Ultrasonication at a pulse mode cycle of 0.1 sec/0.9 sec at 10 % power input for 30 minutes.
UH-4.35-5	Ultrasonication at a pulse mode cycle of 0.4 sec/0.6 sec at 35 % power input for 5 minutes.
UH-4.35-30	Ultrasonication at a pulse mode cycle of 0.4 sec/0.6 sec at 35 % power input for 30 minutes.
ParSD	Particle size distribution
PorSD	Pore size distribution

5.1. Effect of Different Mixing Procedures on CL Formulation and PEMFC Performance

Three distinct mixing methods were selected to study the effect of mixing on CL formulation and fuel cell performance. Here, the mixing methods used in this study are high shear stirring, bead milling and ultrasonic homogenisation.

5.1.1. Catalyst Ink Particle Size

The mechanical processes producing dispersion are unique for each mixing procedure. Subsequently this would result in ink formulations with different particle arrangements and sizes, and ultimately could result in variable PEMFC performance.

The graph below depicts the ParSD for dispersions produced using different mixing techniques.

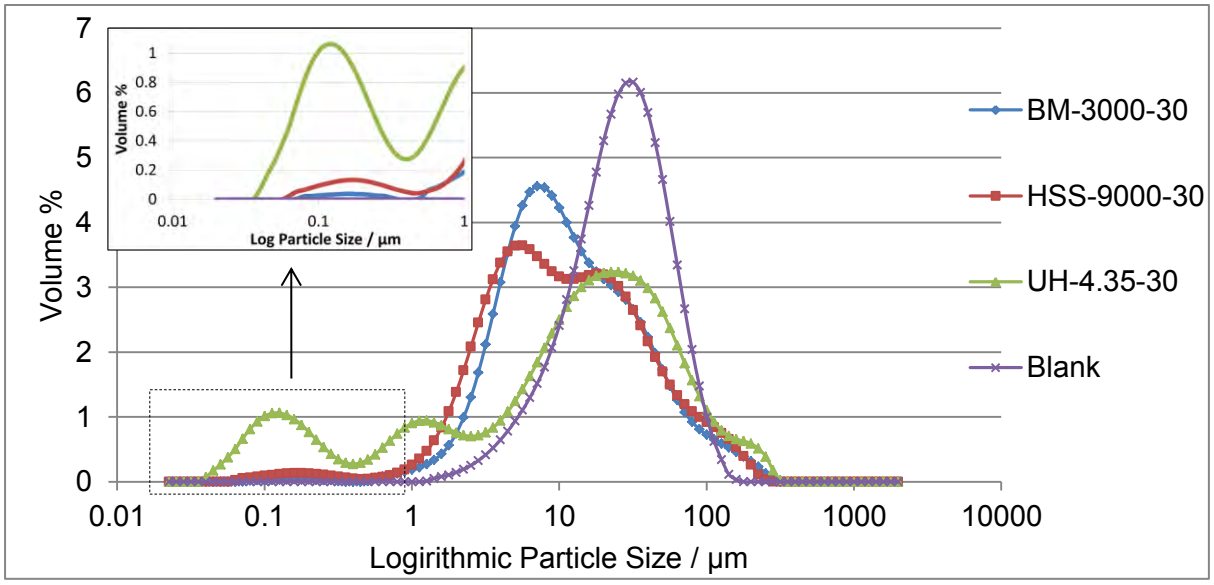

Figure 39: Particle size distributions for catalyst inks using BM, HSS and UH mixing techniques between 0.1-10 000 µm (main plot) and 0.02-1 µm (insert).

ParSD can assist in understanding how each technique mixes the inks and its impact on the latter formation of the CL. As stated by Özcan-Taskin et al., (2009), depending on the bond strength and interactive stresses amongst agglomerates, particle breakup can occur through three different mechanisms and can be evaluated using ParSD. The mechanisms described are as follows: 1. Erosion: Small fragments are progressively sheared off from large agglomerates, gradually leading to more small particles and the resulting ParSD is typically bimodal. 2. Rupture: Large agglomerates are broken down into smaller equisized agglomerates in a stepwise process resulting in monomodal ParSD. 3. Shattering: Very high energy dispersion could lead to large agglomerates breaking into minute particles without intermediate sizes (also) resulting in bimodal ParSD (Özcan-Taskin et al., 2009; Zhang et al., 2012). Figure 39 shows the ParSD for BM-3000-30, HSS-9000-30, UH-4.35-30 and a Blank, briefly hand stirred ink, representing non-mixed catalyst ink. In the particle size range of 0.02-500 µm, catalyst ink carbon agglomerate ParSD is observed. The mixed-ink curves show a reduction in the 30 µm peak and a leftward shift to smaller particle sizes. Therefore

by comparing the Blank to the other mixed-ink curves it is clear that comminution reduces particle size. The BM-3000-30 curve has a narrow distribution and has an observable peak at about 7 µm. The HSS-9000-30 curve shows a similar trend however, smaller particles are produced as observed by the leftward shift. Monomodal distribution are characterised by distribution curves with a single peak. From Figure 39, nearly monomodal distributions are produced by BM and HSS. Monomodal distribution is a result of very good mixing-energy distribution resulting in equivalent comminution rates throughout the mixture. Lindermeir et al., (2004) has noted that a monomodal and narrower ParSD lead to more stable suspensions by reducing sedimentation thus increasing catalyst ink processability. BM and HSS both use contact mechanical forces during ink dispersion. Therefore this could mean that particles respond similarly during comminution and could explain the similarity between the two curves. On the other hand, high intensity cavitation events during UH seem to produce very small particles. This is observed by the reduction of the 20 µm peak to a dispersed ink with peaks at 1 µm and 0.1 µm, as shown in the UH-4.35-35 ParSD curve. UH produces the greatest ParSD range and shows that the inks produced during sonication are not very stable.

5.1.2. Energies of Mixing

Each mixing method uses totally different techniques to distribute and disperse the ink constituents. Therefore, it would be useful to quantify the energy input to each technique. During the process of comminution particles collide and break down and this changes the energy state of the system. A direct way of calculating this energy input is by doing an energy balance whereby temperatures are recorded over the time period of mixing. Thus, using a feasible heat capacity for the ink mixture, the energy input could be calculated. The temperature change versus time was obtained for each mixing technique, and plotted as shown in Figure 40. It was observed that the temperature increased linearly versus mixing time; however, the temperature in the BM ink mixture did not show significant change. This indicated that the energy transfer as a result of bead agitation to catalyst ink is very low, producing a catalyst ink mixture with a low specific energy.

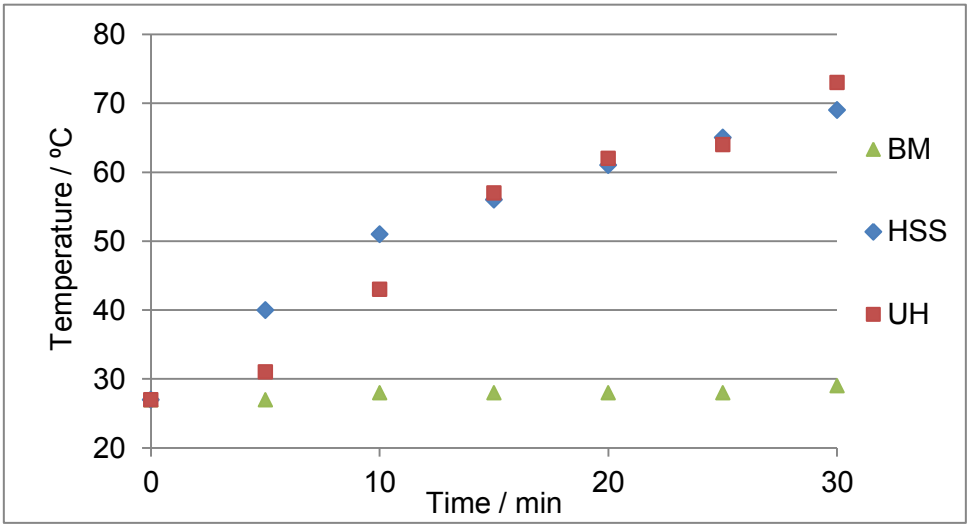

Figure 40: Temperature versus time graph comparing each mixing condition: BM-3000-30, HSS-9000-30 and UH-4.35-30. The temperatures where measured in the mixing solution during a period of 30 min and various power inputs, see Table 10.

5.1.3. Catalyst Layer Morphology

Figure 41 underneath shows the imaging analysis of the catalyst layer under SEM for the various mixing techniques.

BM-3000-30

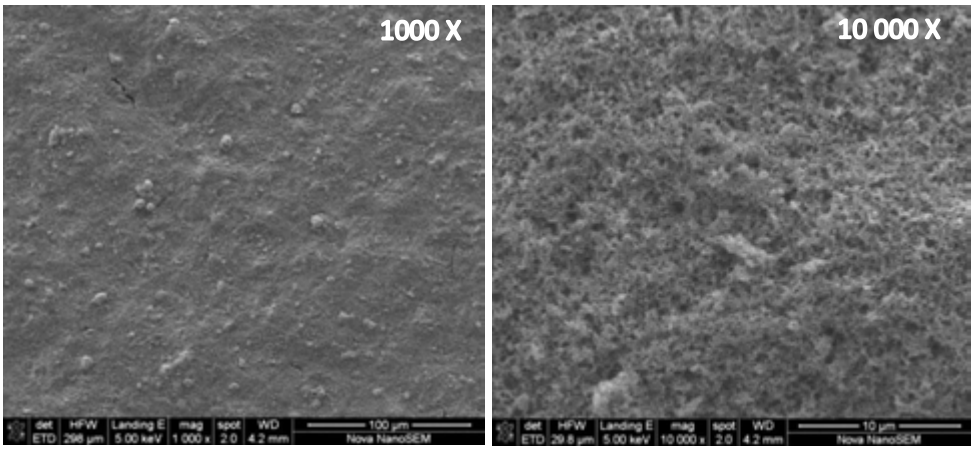

HSS-9000-30

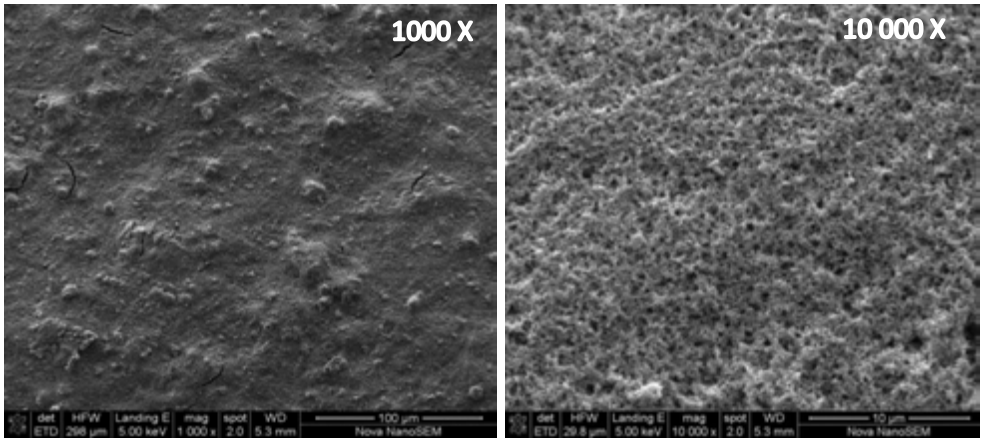

UH-4.35-30

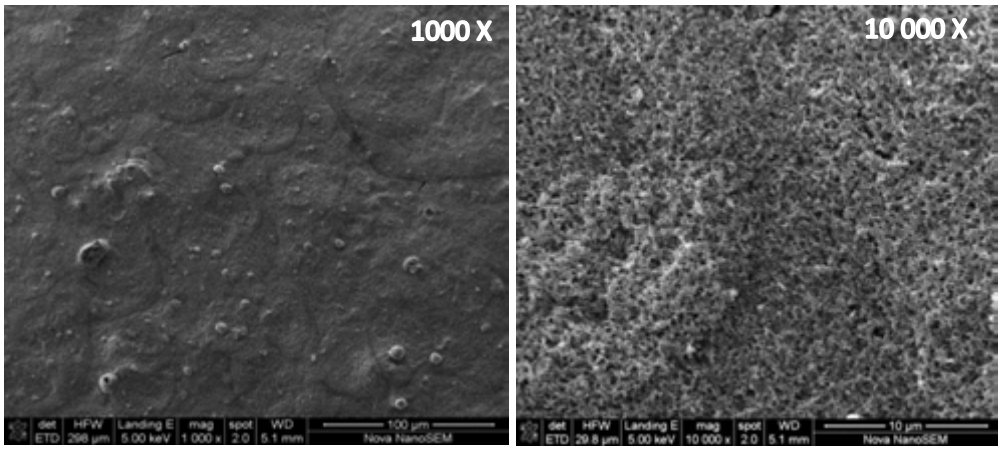

Figure 41: SEM analysis showing the topography of CLs produced using BM. HSS and UH at various times and powers at 1000 and 10 000 times magnification.

Each of the surfaces at 1000 times magnification appears to be quite smooth with no significant differences in their morphologies. However, it seems that at 10 000 times magnification, HSS-9000-30 and UH-4.35-30 show a very defined and uniform pore structure, whereas the BM-3000-30 pore structure appears irregular.

Catalyst coated onto Teflon was used to characterise CL properties, as subsequent steps might bring about changes in the CL properties formulated by mixing. CCM SEM images are shown in Appendix A. These show that the CL surfaces change after hot pressing and decaling. Therefore, this aspect should be considered when evaluating results.

5.1.4. Distribution of Catalyst Layer Components

To evaluate the distribution of catalyst layer components, EDX analysis was conducted on a sample of each CCS prepared by various mixing conditions. Elemental mapping by EDX is a commonly used technique to characterise the distribution of CL components. Fluorine and sulfur are both constituents of Nafion ionomer and both commonly used to map ionomer distribution (Scheiba et al., 2008). However, the substrate on which the CL has been coated onto is made of Teflon, of which fluorine is a component. Therefore, in this study we have focused on the sulfur signal. The analysis in Table 11 shows the mean weight percent and sample standard deviation (Stdev-S) of sulphur (S) and platinum (Pt) taken at four different sites (for each sample). Also shown is the ratio of S to Pt from the data obtained. This ratio serves as a representation of the availability of Nafion (which sulphur is a component of) to the platinum catalyst. It (i) serves as a unifying term representing the level of distribution for both catalyst and ionomer within the CL; (ii) gives a representation of the availability of Nafion to Catalyst, a numerical value for performance optimisation during SEM characterisation. Ideally, a distributed catalyst layer would have equal S to Pt ratios and if this is the case, would have a standard deviation of zero. Thus, the lower standard deviation could suggest a better distribution of components in the catalyst layer.

The table below shows the relative mean and Stdev-S wt. % of S and Pt for each of the mixing methods.

Table 11: EDX data of CL prepared using BM, HSS and UH

BM-3000-30	**S**	**Pt**	**S:Pt**
Mean (wt. %)	1.585	26.990	0.059
Stdev-S (wt. %)	0.047	0.306	0.0016
HSS-9000-30			
Mean (wt. %)	1.683	26.153	0.064
Stdev-S (wt. %)	0.077	0.223	0.0033
UH-4.35-30			
Mean (wt. %)	1.603	26.080	0.061
Stdev-S (wt. %)	0.092	0.768	0.0032

The data shows the quantities of Pt and S are equivalent in each CL which is to be expected as the ink components are added in identical quantities. BM tends to show a lower Stdev-S and thus, suggests a better distribution of CL components. However, in all cases the

magnitudes of S:Pt are relatively small, suggesting that at the operating conditions, each mixing method thoroughly distributes the catalyst inks.

5.1.5. Catalyst Layer Pore Structure

The porous structure of the catalyst layer is predominantly due to the agglomeration and internal structures of the carbon support material. N_2 physisorption was used to measure CL pores sizes in the range of 1 nm to 300 nm. Two distinct peaks are observable; those <10 nm represent the primary pores (micro pores) and those >10 nm represent secondary pores (meso pores). Hg-intrusion porosimetry was used to determine the higher end secondary pore structures or the macro pores of size > 1 µm. Together, N_2 physisorption and Hg-intrusion were used to span the entire CL pore regime in order to effectively evaluate the influence mixing has on CL formulation. The PorSD adsorption curves in Figure 42 shows the effect of different mixing procedures on micro and meso pore structures. All the curves shown have a similar shape which is expected as they represent CLs produced from the same catalyst material. There is a distinct difference between the meso and micro pore volumes of BM as compared to HSS and UH mixing techniques. Literature shows that the micro pores are dominated by the internal pores of the primary catalyst particle and are not a direct effect of CL formulation (Uchida et al., 1995, Shin et al., 2002). However, primary pores are affected by the nature of the secondary pores and CL constituents (Xie et al., 2004, Chisaka & Daiguji, 2006, Malek et al., 2007). Although BM micropore volume is relatively high, the secondary pores within the sample dominate thus lowering the total pore volume. Subsequently BJH Adsorption cumulative volume of pores in Table 12 shows that the BM CL has a lower total pore volume compared to HSS and UH.

Table 12: N_2 physisorption results for CCSs prepared by mixing inks at BM-3000-30, HSS-9000-30 and UH-4.35-30

Mixing Type	**BJH Adsorption cumulative volume of pores between 1.7 nm and 300 nm width / $cm^3.g^{-1}$**
BM-3000-30	0.010342
HSS-9000-30	0.010369
UH-4.35-30	0.010438

The table below depicts the total pore volume for CLs prepared using BM, HSS and UH using Hg-Intrusion Porosimetry.

Table 13: Hg-Intrusion Porosimetry Data for CL prepared using different mixing conditions

Mixing Type	**Intrusion Volume $cm^3.g^{-1}$**
BM-3000-30	0.066
HSS-9000-30	0.088
UH-4.35-30	0.090

Shown below are the PorSD curves obtained during N_2 Physisorption analysis (Figure 42) and Hg-Intrusion Porosimetry (Figure 43).

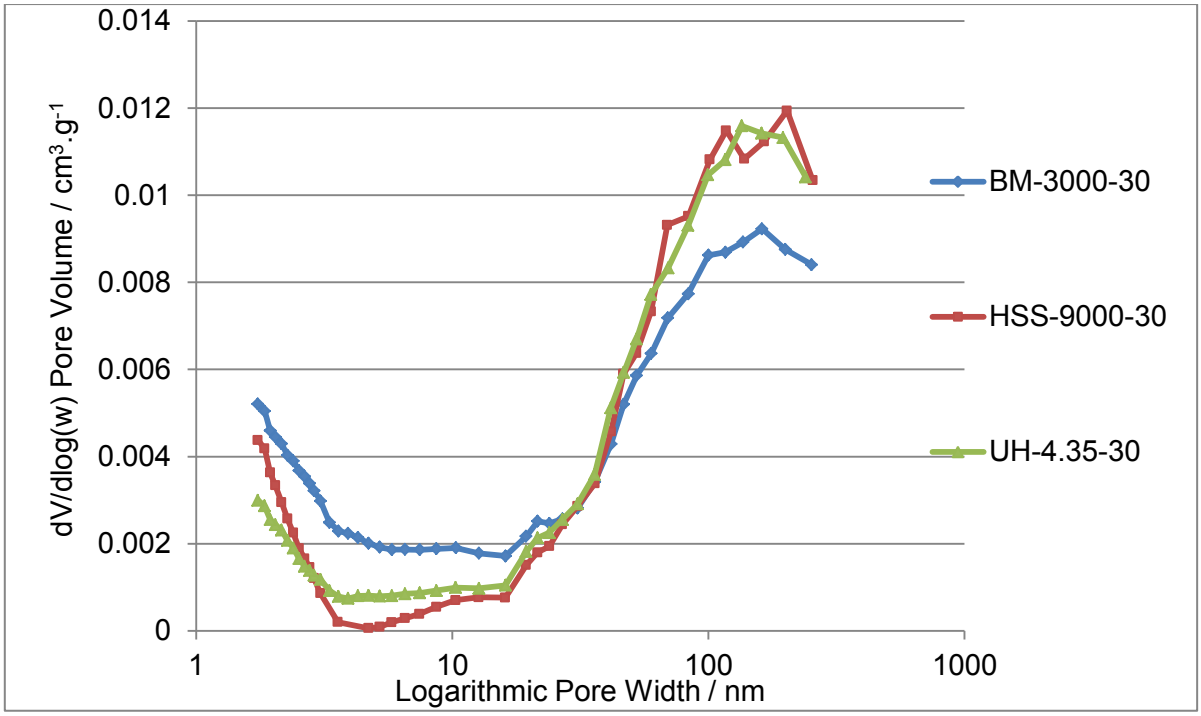

Figure 42: Adsorption PorSD plots for CCS prepared by mixing inks at BM-3000-30, HSS-9000-30 and UH-4.35-30.

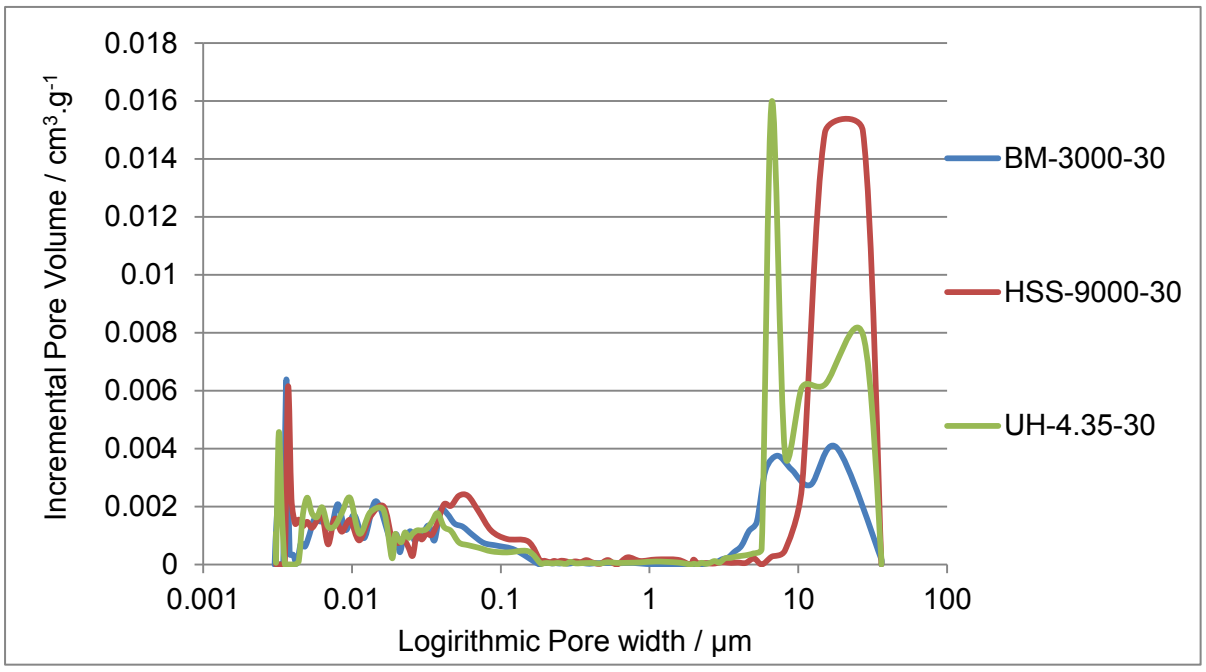

Figure 43: Pore Size distribution curves using Hg-Porosimetry.

The CL macropores (> 1 µm) were observed by Hg-Porosimetry for the different mixing conditions and the resulting intrusion volume is shown in Table 13 and Figure 43. From the result it can be determined that the macro pores are responsible for almost 90% of the total pore volume in CLs. Similarly to the N_2 Physisorption result, BM mixed sample produced a much lower pore volume compared to HSS and UM CLs. This correlates to the result observed under SEM which shows the BM CL resulted in a less porous structure. The data

depicts that CLs produced by BM have a lower porosity due to the absence of secondary porous structures. A possible explanation for this is that BM breaks down ionomer films by high impact collisions and grinding. This could diminish the connected network structure between ionomer films, causing it to block and fill secondary pores.

During HSS and UH, specific mixing energies are very high as compared to BM. As a consequence of the excess mixing energy, these catalyst ink slurries heats up. During HSS and UH mixing, catalyst ink temperature increase to over 70 °C (Figure 40). It has been reported that the morphology of Nafion is heat dependant and significantly changes with temperature. At low temperatures, Nafion fibres have a rigid-rod like structure, however; as temperature increases it transitions to a thinner, loose and entangled structure. Furthermore, contact between catalyst agglomerates and Nafion improves at higher temperatures (Yaun et al., 2012a). As depicted in Figure 44, at lower temperatures Nafion could cause blockage of pores due to the nature of its size whereas at higher temperatures, Nafion is elongated and exposes a larger area of pores.

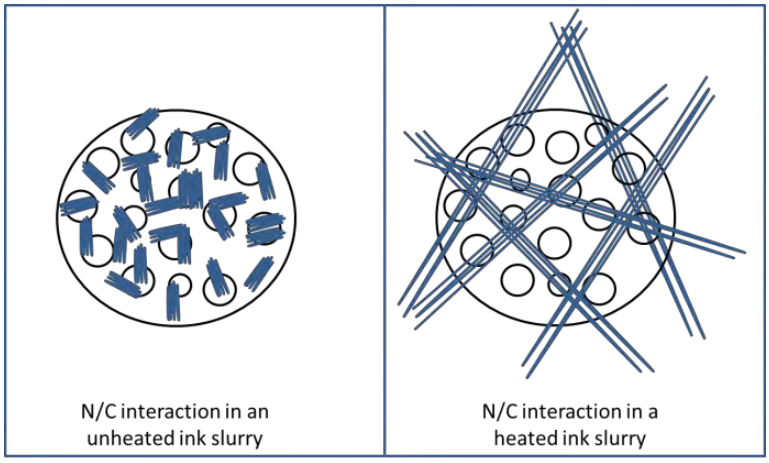

Figure 44: Representation of the Nafion-catalyst interaction in an unheated ink slurry (Left) and a heated ink slurry (right).

5.1.6. Electrochemical Performance Characterisation

After a conditioning for a period of 2 hours, polarisation curves were obtained whilst operating at 100 % RH, 1 bar back pressure, cell temperature of 80 ˚C and at constant flows of oxidant and hydrogen of 1.24 $l.min^{-1}$ and 0.39 $l.min^{-1}$, respectively. The i-E curves depicted in Figure 45 show a comparison between MEA performance of CLs prepared using different mixing techniques. In this study, two air and one oxygen i-E curve was recorded per sample. The mean i-E air curves were plotted and presented. Oxygen i-E curves are shown in Appendix BAppendix and in all cases, it correlates to the performance data obtained during performance with air and EIS (relative ohmic resistance). A clear performance difference is seen in the ohmic region (0.2 $A.cm^{-2}$ – 0.6 $A.cm^{-2}$) of the polarisation curves. A higher performance difference with HSS (compared to BM and UH) is due to the improved proton conductivity, and lower charge transfer resistance within the CL. The performance difference between HSS and BM in the range 0.6 $A.cm^{-2}$ – 0.8 $A.cm^{-2}$ are due to mass transfer resistance observed by lower porosity of the BM CL. Mass transfer losses for UH CL cannot be explained by the lack of CL porosity (prior to hot pressing), however this might be a consequence of CCM processing steps after CL formulation.

Figure 45 (below) shows the polarisation curves comparing the performance of MEAs prepared using the various catalyst ink mixing procedures.

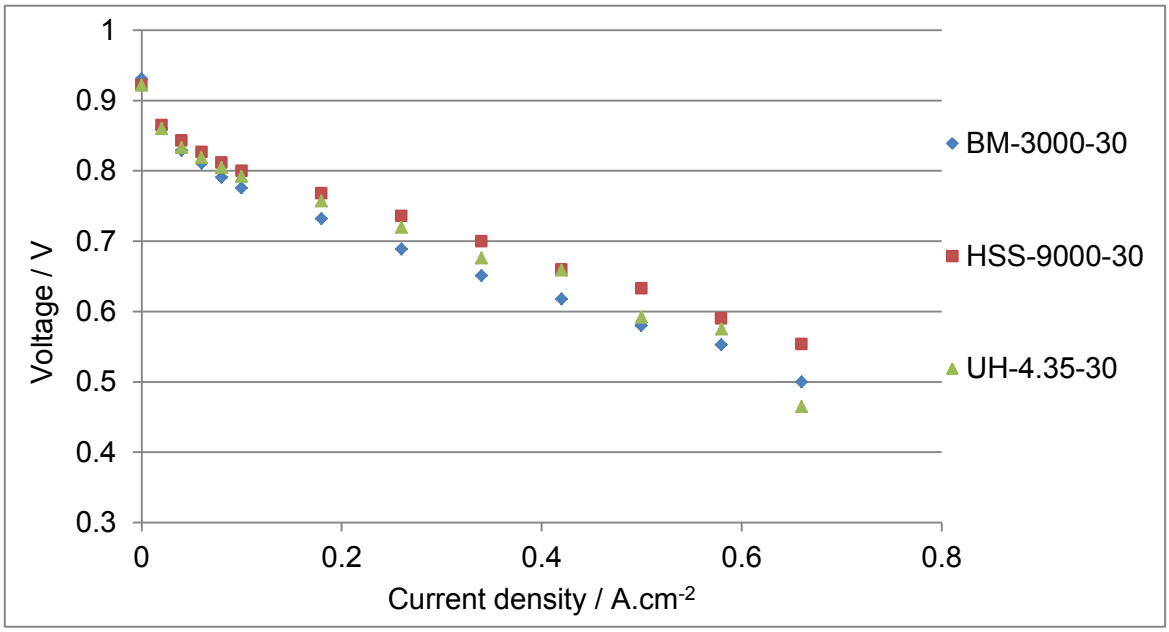

Figure 45: H_2/Air Polarisation curves for MEAs prepared by inks mixed with different techniques. N/C = 1 for all electrodes. Testing conditions: T_{cell}=80˚C, RH=100%, gases at 1 bar using N212 membrane and SGL24BC GDL.

Shown in Figure 46 (below) are the Nyquist plots of MEAs prepared using the various catalyst ink mixing procedures. These were plotted using EIS data, which was conducted immediately after polarisation tests.

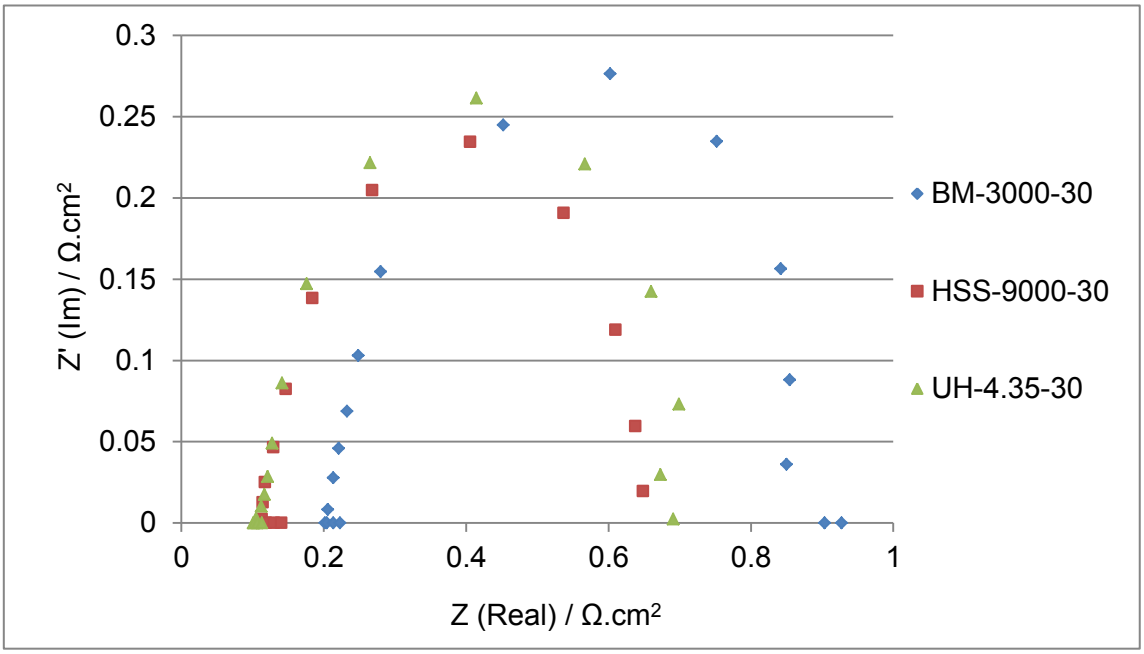

Figure 46: Nyquist plot at 100 mA.cm^{-2} for MEAs prepared by inks mixed by different techniques. N/C = 1 for all electrodes. Testing conditions: Frequency range: 20000 – 0.1 Hz, T_{cell}=80˚C, RH=100%, gases at 1 bar using N212 membrane and SGL24BC GDL.

Shown in the table below is the Pt-loading for each tested sample; the calculated ECSA; and the charge transfer resistance obtained from the Nyquist plots.

Table 14: ECSA and charge transfer resistance for MEAs prepared by inks mixed by different techniques

Sample Name	Anode Loading ($mg.cm^{-2}$)	Cathode Loading ($mg.cm^{-2}$)	ECSA ($m^2.g^{-1}$)	Charge transfer resistance at $100mA.cm^{-2}$ ($\Omega.cm^2$)
BM-3000-30	0.398	0.525	18.38	0.644
HSS-9000-30	0.363	0.542	29.40	0.532
UH-4.35-30	0.422	0.550	26.93	0.587

EIS was performed for each sample and represented as Nyquist plots- conducted at a low current density of 100 $mA.cm^{-2}$, and are shown in Figure 46. EIS characterisation can be conducted at any point along the (i-E) curve. At low current densities, activation kinetics dominate and the resulting impedance response largely depicts the ohmic and activation losses due to the cathode (as cathode activation >> anode activation) (Jang et al., 2009). Depicted here is a typical semi-circular shaped graph where the left intercept with Z (Real) represents the ohmic resistance and the diameter of the loop represents the charge transfer resistance. Ohmic resistances are predominantly due to the transfer of electrons from the anode to the cathode in the circuit loop, and the membrane resistance. The result shows membrane resistance was negligible as seen from the consistent steep slope of the arc, as cell conditioning and RH were kept constant during all tests. Charge transfer resistance is a matter of importance when characterising the Nafion/carbon interaction. Charge transfer represents the resistance to the charge-transfer process at the electrode surface influencing both ionic and electronic conduction and therefore impact the reaction kinetics (Cooper & Smith, 2006). From the EIS and ECSA data shown in Table 14, the BM sample performs the poorest, followed by UH and then HSS. This result correlates with the performance observed by the i-E plots. A significant ohmic loss is observed when testing the BM MEA sample. This is a result of inefficient electron transfer as membrane hydration is kept constant among all tests. This could be an effect of ionomer films blocking contact between adjacent agglomerates shielding electron transfer. In addition, ParSD indicates BM has larger particles (graph shows log scale so the difference of BM sample might be significant) which results in a lower total contact area which could decrease electron transfer. Charge transfer resistance can be a consequence of a poor three phase contact between electrolyte, catalyst layer and a poor diffusion of reactant gases. On a microscopic level, an ionomer network that is not well established could limit the transfer of H^+. As noted in the previous section, BM could result in breaking down of ionomer films and therefore disturb the contact between adjacent ionomer films. Passalacqua et al., (2000) used the percolation model to describe the effect of Nafion content on ionic and electronic conduction in the CL. Here a conductive/percolating path can only be formed if there is an uninterrupted chain of catalyst particles or Nafion network for electronic and ionic conduction to be possible, respectively. As seen in Figure 44, an elongated chain is more likely to produce an interconnected Nafion network in the CL. Consequently, this would improve H^+ transfer and thus, enhance PEMFC performance. Therefore, it is proposed that such networks are more likely to appear in HSS and UH catalyst inks due to the nature of Nafion at higher temperatures during catalyst ink mixing. Numerous studies have been done on the effect of Nafion morphology on PEMFC

performance. It has been observed that when Nafion is stretched, the proton conductivity increases enhancing FC performance (Allahyarov & Taylor, 2008).

The data suggests that HSS of catalyst inks is the most ideal form of mixing, in the range of parameters studied. From this, it is likely to conclude that a monomodal ParSD and a highly porous electrode are beneficial to establishing a CL with desirable characteristics, which results in low mass transfer losses and low charge transfer resistance, ultimately improving overall FC performance.

Comparisons drawn up to this point does not incorporate comprehensive details pertaining to the mechanisms of mixing and these might play a substantial role to the observed results. In addition, mixing energies and parameter ranges studied were very different which ultimately affects the formulations produced after mixing (as observed by: Lindermeir et al., 2004; Lim et al., 2006 and Pollet & Goh, 2014). To therefore gain insight on how catalyst inks are influenced by the individual techniques, each mixing method was studied separately. In this study we determine the effect of these individual mixing techniques by varying mixing intensity and mixing time in a 2 x 2 factorial design. From here we can then conclude which technique is favourable based upon its individual effect on CL formulation.

5.2. The Influence of Mixing Parameters on Catalyst Layer Properties and Fuel Cell Performance Using Design of Experiments

5.2.1. BM of Catalyst Inks

Bead-particle collisions generate impact forces during bead milling. Throughout catalyst ink mixing, these forces grind carbon agglomerates to smaller particle sizes. The extent to which particles are milled depends on the intensity of the local bead-particle collisions and also the time to which the milling process is allowed to proceed. In order to optimise catalyst ink distribution it is necessary to study the effect of both time and mixing intensity. Shown in Figure 47 is the 2 x 2 factorial design matrix depicting the parameters on which the study of BM was based.

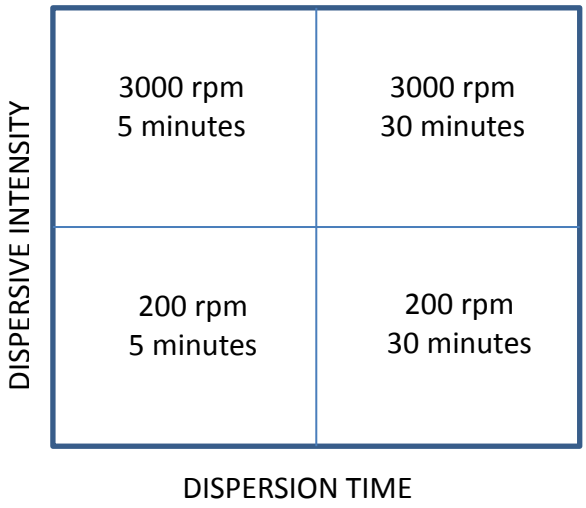

Figure 47: 2 x 2 factorial design matrix depicting the magnitudes of mixing intensity and mixing time in evaluating the effect of BM on CL formulation and PEMFC performance

5.2.1.1. Catalyst Ink Particle Size

Particle size analysis shown in Figure 48 depicts the dispersions produced after BM at different parameter settings.

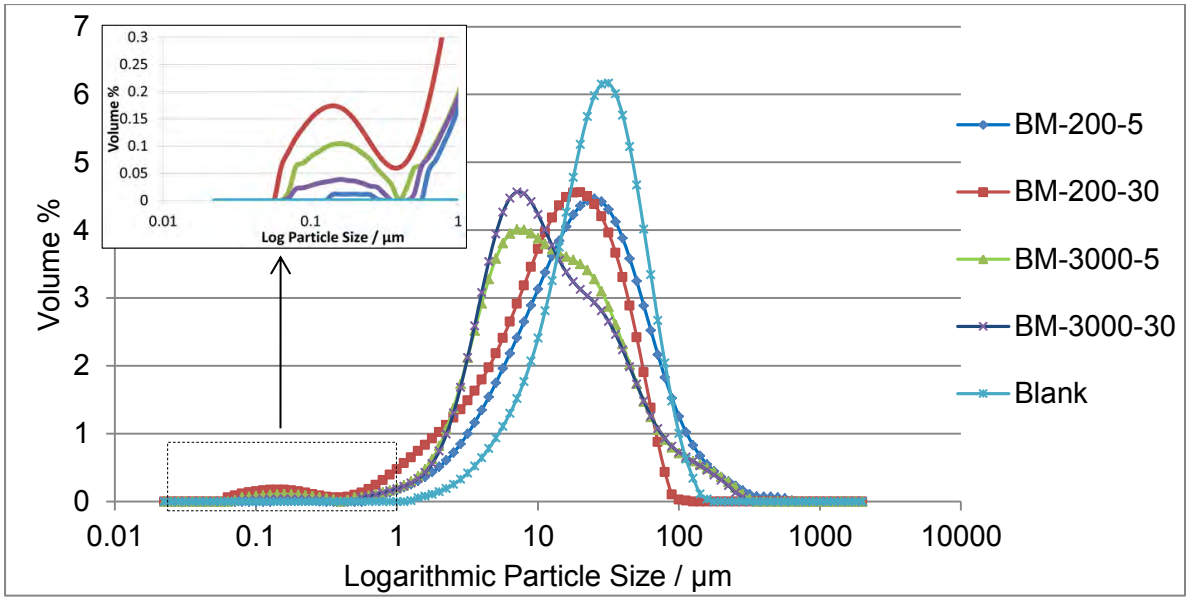

Figure 48: Particle size distributions for catalyst inks mixed using variable parameters of BM between 0.1-10 000 µm (main plot) and 0.02-1 µm (insert).

It is clear that BM has an impact on the reduction of ParSD as seen from the difference between the mixed and unmixed sample (Blank). Comparing samples BM-200-5 and BM-200-30, it can be seen that the graph slightly shifts to the left at a higher mixing time-observed by the peak shift from 20 µm to 17 µm, respectively. Similarly, the shoulder of graph BM-3000-5 (at 17 µm) is retracted as mixing time is increased producing the BM-3000-30 curve. However, agglomerate size reduction is significantly affected when the agitation rate is increased from 200 rpm to 3000 rpm observing peak shifts of > 10 µm. This result shows that mixing intensity governs the rate of which agglomerates break down as compared to mixing time owing to its greater influence to particle size reduction. The mechanism of mixing as determined from the ParSD suggests that BM rupture catalyst agglomerates during the dispersion process (adapted from mechanisms conceptualised by Özcan-Taskin et al., 2009; Zhang et al., 2012).

5.2.1.2. Catalyst Layer Morphology

Structural characterisation by SEM shows the effect of mixing on the morphology of the CL as shown in Figure 49. Shown here are the CLs coated onto Teflon sheets. Seen from 1000 x magnification image, BM-200-5 sample CL has bumps of agglomerates protruding from the surface (circle in red). This indicates larger agglomerates pushing out during the drying process. Seen from the 10 000x magnification image, the pore structure appears to be intermittent. Further, ridges are observed (circle in yellow) in the CL likely due to irregular shaped particles. As compared to BM-200-5, BM-200-30 has a smoother surface with smaller lumps protruding from the CL (circle in red). From the 10 000x image (circle in yellow) it can be seen that irregular structures develop due to larger agglomerates stacking up. The pore structure of the BM-3000-5 (10 000x image) appears to be more regular as finer particles are produced thus resulting in a more evenly layered pore structure; however, the cracked surface seen at lower magnification (1000x) is likely due to rapid drying (Seland et al., 2006; Huang et al., 2011). The most even CL surface and a well-defined pore

structure is produced from BM-3000-30. This is likely caused by smaller particles formed from prolonged mixing time and more intense agitation rate (as seen in Figure 48).

BM-3000-5

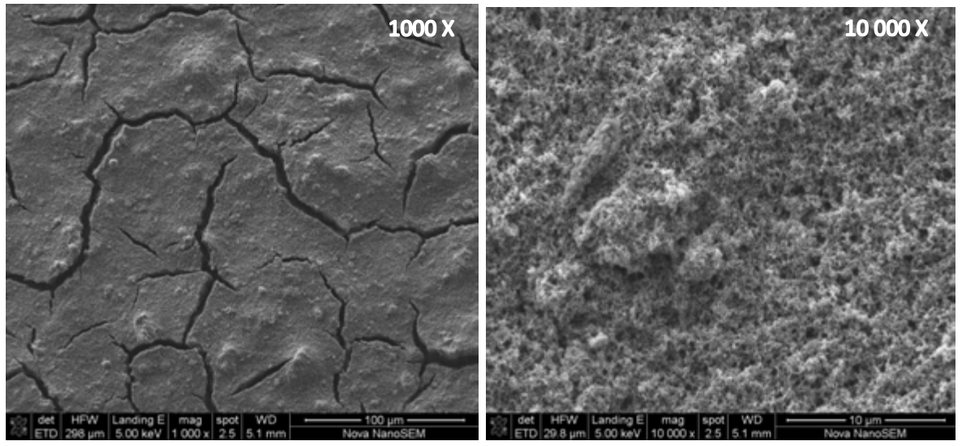

BM-3000-30

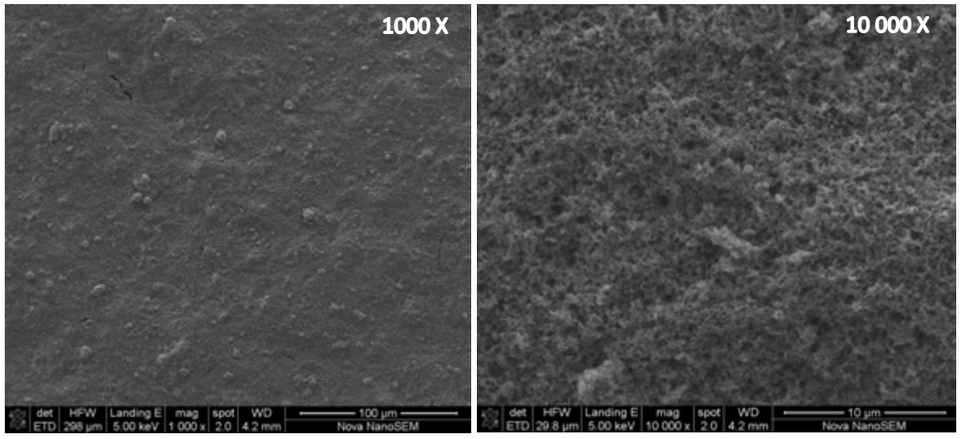

BM-200-5

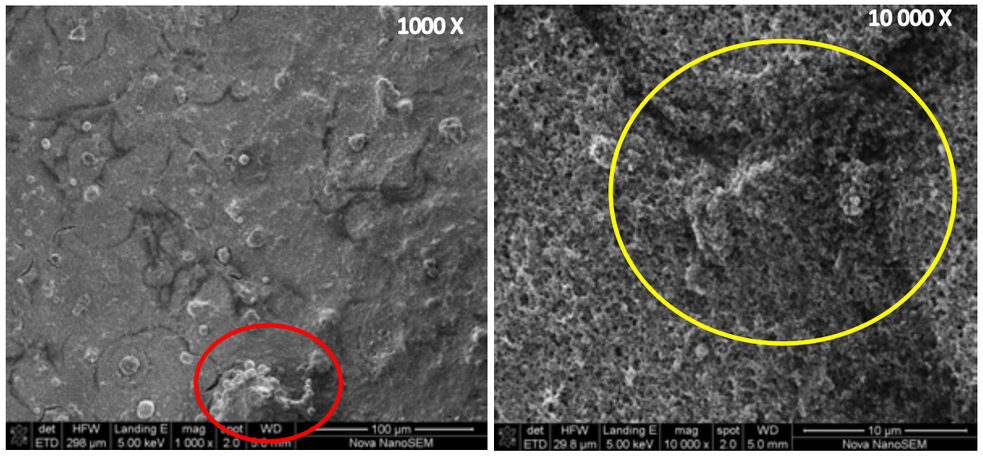

BM-200-30

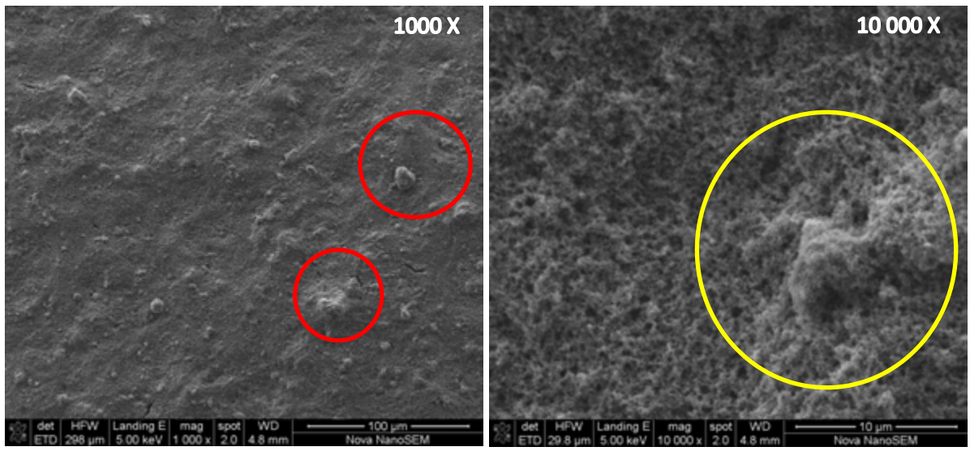

Figure 49: SEM analysis for CCSs produced using variable parameters of the BM mixing technique.

5.2.1.3. Distribution of Catalyst Layer Components

The catalyst:Nafion ratio was evaluated using EDX as described above (section 5.1.4). The results are summarised in the table underneath.

Table 15: EDX analysis showing the elemental distribution on the surface of a CCS produced using variable parameters of the BM mixing technique

BM-3000-5	**S**	**Pt**	**S:Pt**
Mean (wt. %)	1.508	24.690	0.061
Stdev-S (wt. %)	0.101	0.425	0.0032

BM-3000-30	**S**	**Pt**	**S:Pt**
Mean (wt. %)	1.585	26.990	0.059
Stdev-S (wt. %)	0.047	0.306	0.0016

BM-200-5	**S**	**Pt**	**S:Pt**
Mean (wt. %)	1.548	23.998	0.064
Stdev-S (wt. %)	0.251	0.809	0.0102

BM-200-30	**S**	**Pt**	**S:Pt**
Mean (wt. %)	1.510	28.345	0.053
Stdev-S (wt. %)	0.084	0.506	0.0039

The figure below (Figure 50) shows a volume element representing the difference between a poorly and well mixed catalyst ink. Poorly mixed inks contains large differences in agglomerate sizes, however, a well-mixed ink would produce uniformly distributed ink components. Therefore, EDX analysis over randomly chosen regions would show almost identical amounts of components in every sample, and result in a very low S:Pt Stdev-S.

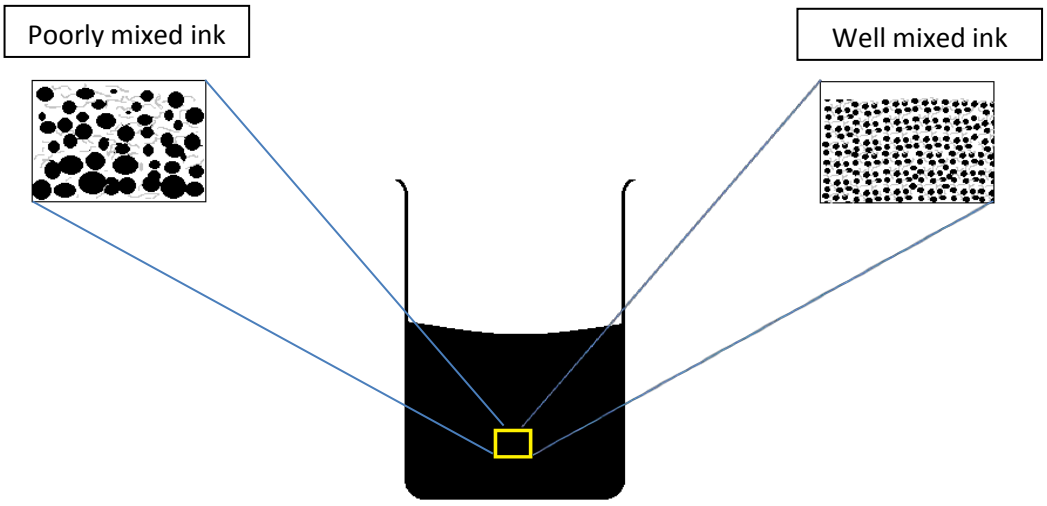

Figure 50: Comparison between the effectiveness of mixing to produce catalyst ink distributions.

The quantities of sulphur amongst the various data sets are almost equal whereas the Pt content varies quite significantly. In some instances during mixing, clusters of catalyst

agglomerates aggregate due to ineffective distribution (see Figure 50). The level of dispersion is dependent on the nature of the mixing process. An ineffective dispersion leads to a inhomogeneous distribution of elements, and therefore a high variation of S:Pt values for different sample areas. On the other hand, a well distributed catalyst layer would have identical quantities of components at any given area analysed, thus produce a low Stdev-S.

Compared to the other samples shown in

Table 15, BM-200-5 produced a relatively high Stdev-S of 0.251 wt. % and 0.809 wt. % for both S and Pt respectively. This could be attributed to insufficient dispersion power and time thus resulting in a high S: Pt ratio of 0.0102 wt. %. Sample BM-200-30, has prolonged mixing time compared to the former sample; therefore enhanced dispersion led to a reduction in S:Pt Stdev-S to 0.0039 wt. %. Samples BM-3000-5 and BM-3000-30 produced the lowest S:Pt Stdev-S ratio of 0.0032 wt. % and 0.0016 wt. % respectively, and is attributed to the effect of increased mixing intensity. This shows that as mixing time and intensity are increased the distribution of components becomes more ideal. The result also shows that a change in mixing intensity produces more evenly distributed samples as compared to mixing time.

BM-3000-5	**S**	**Pt**	**S:Pt**
Mean (wt. %)	1.508	24.690	0.061
Stdev-S (wt. %)	0.101	0.425	0.0032

BM-3000-30	**S**	**Pt**	**S:Pt**
Mean (wt. %)	1.585	26.990	0.059
Stdev-S (wt. %)	0.047	0.306	0.0016

5.2.1.4. Catalyst Layer Pore Structure

Pore size distribution was conducted for CL coated on PTFE for BM mixing conditions indicated in the two-factorial design method. N_2 physisorption and Hg-Intrusion Porosimetry PorSD plots are shown in Figure 51 and Figure 52, respectively. These show the effect of catalyst ink mixing parameters on CL pore volume.

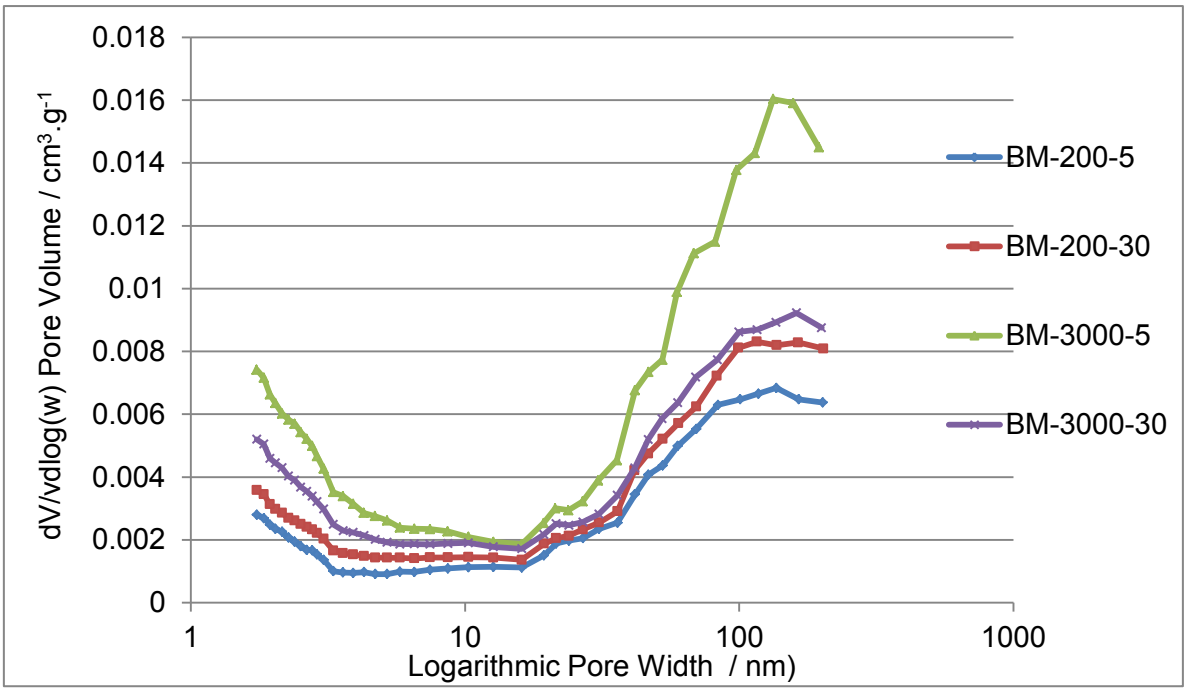

Figure 51: Pore size distribution for BM prepared CL coated onto PTFE.

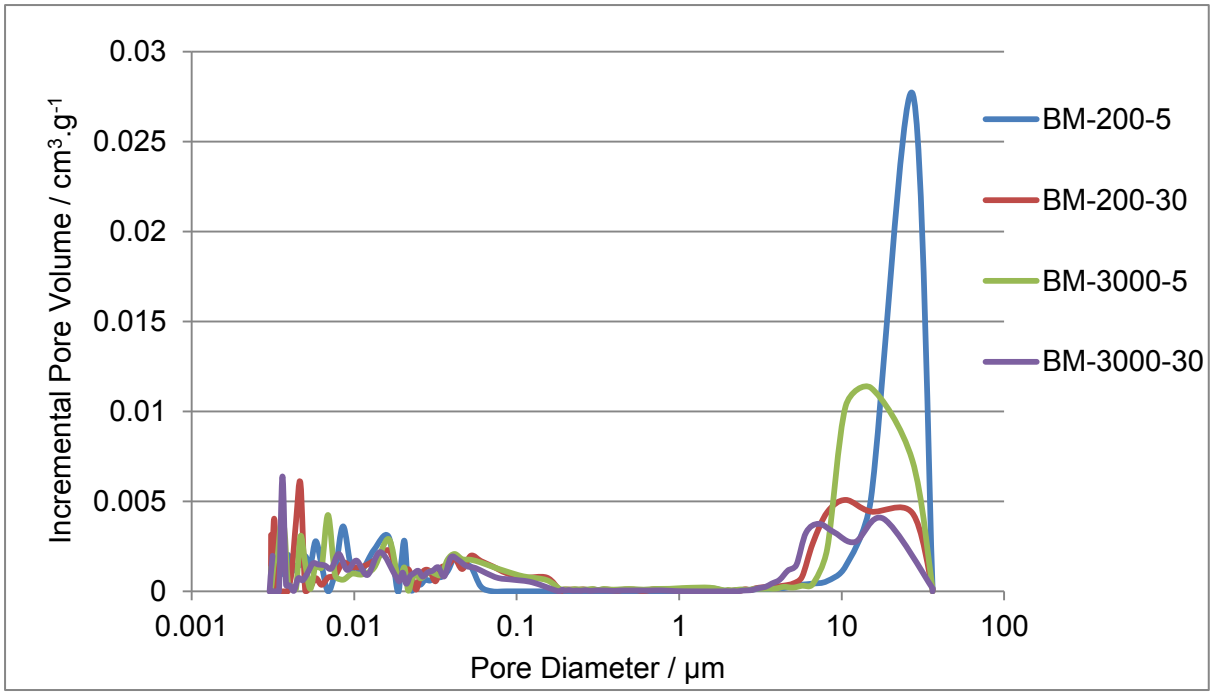

Figure 52: Pore Size distribution curves using Hg-Porosimetry for CCS prepared by BM mixing technique.

The figures below represents the 2 x 2 factorial matrix showing the **total pore volume** for CLs prepared using the BM mixing technique using N_2 Physisorption (left) and Hg-Intrusion Porosimetry(right). The pore volume data is represented in a matrix array to simplify comparison.

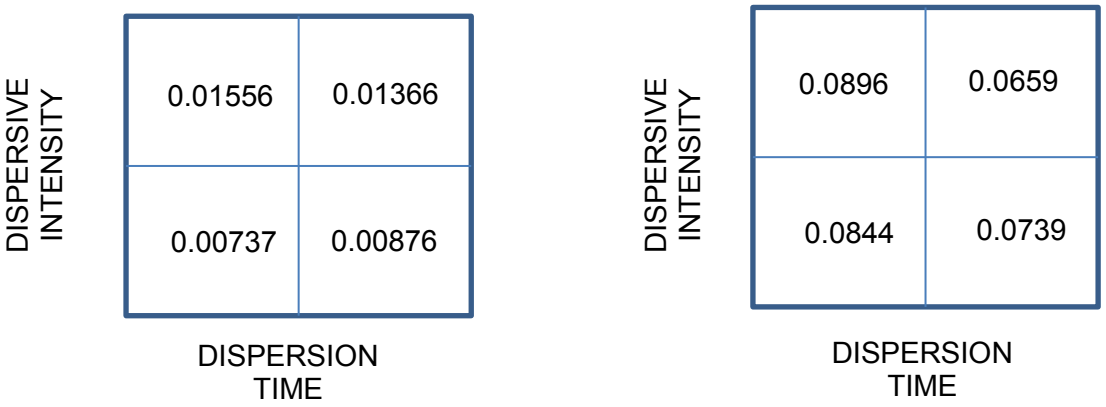

Figure 53: Left: BJH Adsorption cumulative volume of pores between 1.7 nm and 300 nm width ($cm^3.g^{-1}$). Right: Hg-Intrusion Porosimetry Pore volume ($cm^3.g^{-1}$) for CL prepared using different mixing conditions for BM.

It can be seen that the micro and meso pore volumes (Figure 51 and Figure 53) are both proportionally influenced by a change in mixing parameters. The total energy input is characterised by a combination of mixing intensity and mixing time. As the energy input is increased, pore volumes increase: pore volume of BM-200-5 < BM-200-30 < BM-3000-5. However, it appears that an optimum mixing condition exists, after which the catalyst layer porosity diminishes. This is observed by the sudden collapse in the pore volume at BM-3000-30. The Hg-intrusion results in Figure 52 and Figure 53 show a similar observation. This result is likely an effect of too intense grinding over a prolonged time period causing breaking down of ionomer films. These minute films then easily migrate, filling secondary pores and obstructing the flow of substances to both primary and secondary pores. It can be seen that secondary pores are more affected by mixing in comparing the trends in Figure 51 and Figure 52 together with the total pore volumes in Figure 53. When comparing BM-3000-5 and BM-3000-30, the macro pores undergo a large change in volume whilst the meso pores remain slightly affected as it is significantly smaller (supported by the finding of Uchida et al., 1995). Ultimately, mixing time has a greater effect on the resulting pore volume at a higher mixing intensity.

5.2.1.5. Electrochemical Performance Characterisation

The i-E curves in Figure 54 show the performance comparison of MEAs with CLs manufactured at different BM mixing parameters.

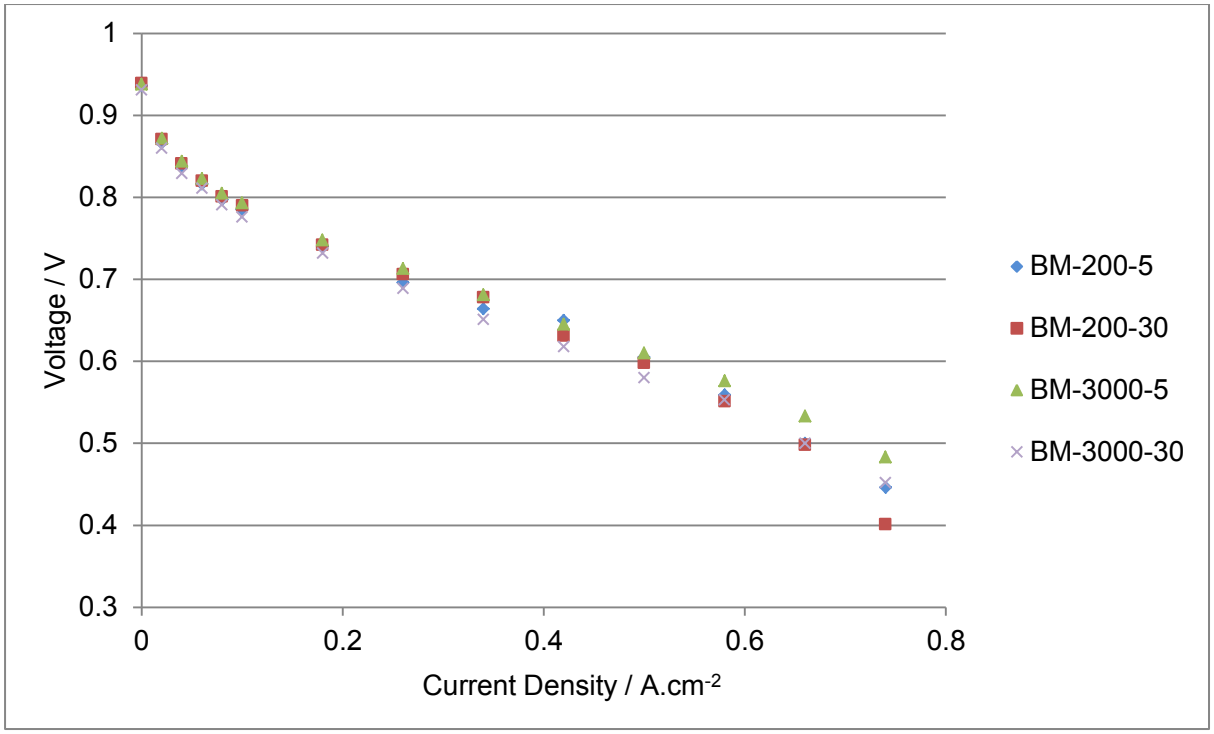

Figure 54: H_2/Air Polarisation curves for MEAs prepared by inks mixed using BM. N/C = 1 for all electrodes. Testing conditions: T_{cell}=80˚C, RH=100%, gases at 1 bar using N212 membrane and SGL24BC GDL.

Shown below are the Nyquist plots of MEAs prepared using the BM mixing technique. These were plotted using EIS data, which was conducted immediately after polarisation tests.

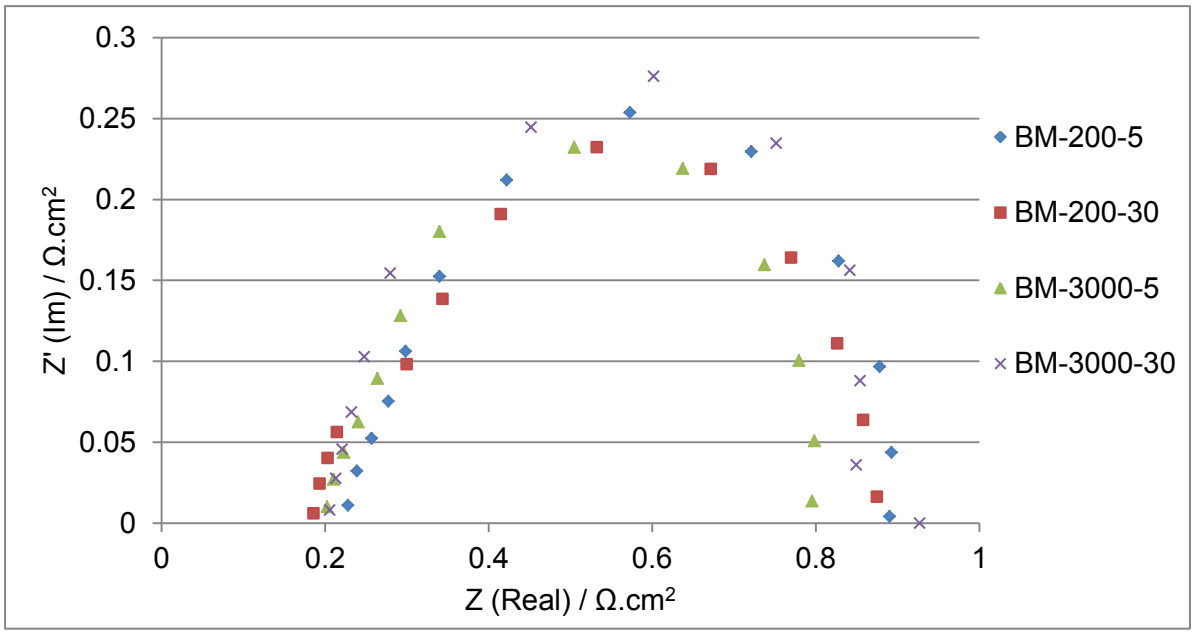

Figure 55: Nyquist plot at 100 mA.cm^{-2} for MEAs prepared by inks mixed using BM at various mixing conditions. N/C = 1 for all electrodes. Testing conditions: Frequency range: 20000 – 0.1 Hz, T_{cell}=80˚C, RH=100%, gases at 1 bar using N212 membrane and SGL24BC GDL.

Shown in the table below is the Pt-loading for each tested sample; the calculated ECSA; and the charge transfer resistance obtained from the Nyquist plots.

Table 16: ECSA and charge transfer resistance for MEAs prepared by inks mixed using BM

Sample Name	Anode Loading ($mg.cm^{-2}$)	Cathode Loading ($mg.cm^{-2}$)	ECSA ($m^2.g^{-1}$)	EIS at $100mA.cm^{-2}$ ($\Omega.cm^2$)
BM-200-5	0.394	0.51	31.03	0.651
BM-200-30	0.416	0.557	36.97	0.689
BM-3000-5	0.421	0.515	33.47	0.574
BM-3000-30	0.398	0.525	18.38	0.644

The performance variation between the various mixing parameters occurs predominantly due to differences in ohmic (0.55 V – 0.75 V) and mass transfer (0.40 V - 0.55 V) resistances (Figure 54). BM inherently changes the nature of the ionomer structure and catalyst agglomeration. This inevitably affects the way ions are transported and how gases diffuse through the catalyst layer. Highly porous electrodes facilitate mass transport through the CL as can be seen for sample BM-3000-5. It has been observed that a cracked surface (such as BM-3000-5, refer to Figure 49) does not necessarily disadvantage PEMFC performance; in fact the converse has been observed by Manahan et al., (2009). BM-200-5, BM-200-30 and BM-3000-30 are significantly affected in the mass transfer regions. This is attributed to the low pore volume of these samples, which obstructs the flow of gases and inhibits water removal from the catalyst layer.

Table 16 shows the calculated ECSA and EIS data for the samples. BM-3000-5 shows superior performance as ionomer networks are well established, therefore producing optimal H^+ transport and improving surface charge transfer. ECSA seems to decrease going from lower to higher end mixing conditions.

5.2.2. HSS of Catalyst Inks

High shear mixing is characterised by very large rotation speeds, high shear rates and highly localised energy dissipation rates at the mixing head (Zhang et al., 2012). The effect of HSS was evaluated in a 2 x 2 factorial design matrix by a variation of mixing intensity and mixing time as shown in Figure 56.

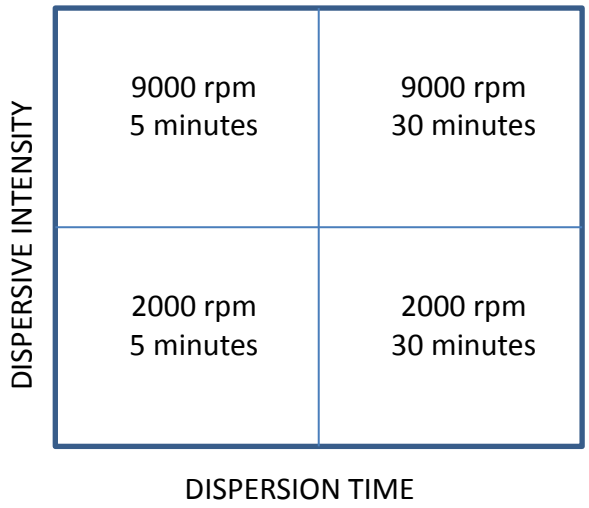

Figure 56: 2 x 2 factorial design matrix depicting the magnitudes of mixing intensity and mixing time, used to evaluate the effect of BM on CL formulation and PEMFC performance

5.2.2.1. Catalyst Ink Particle Size

The effect of various mixing conditions following the factorial matrix (Figure 56) on the ParSD curves for catalyst inks can be seen in Figure 57.

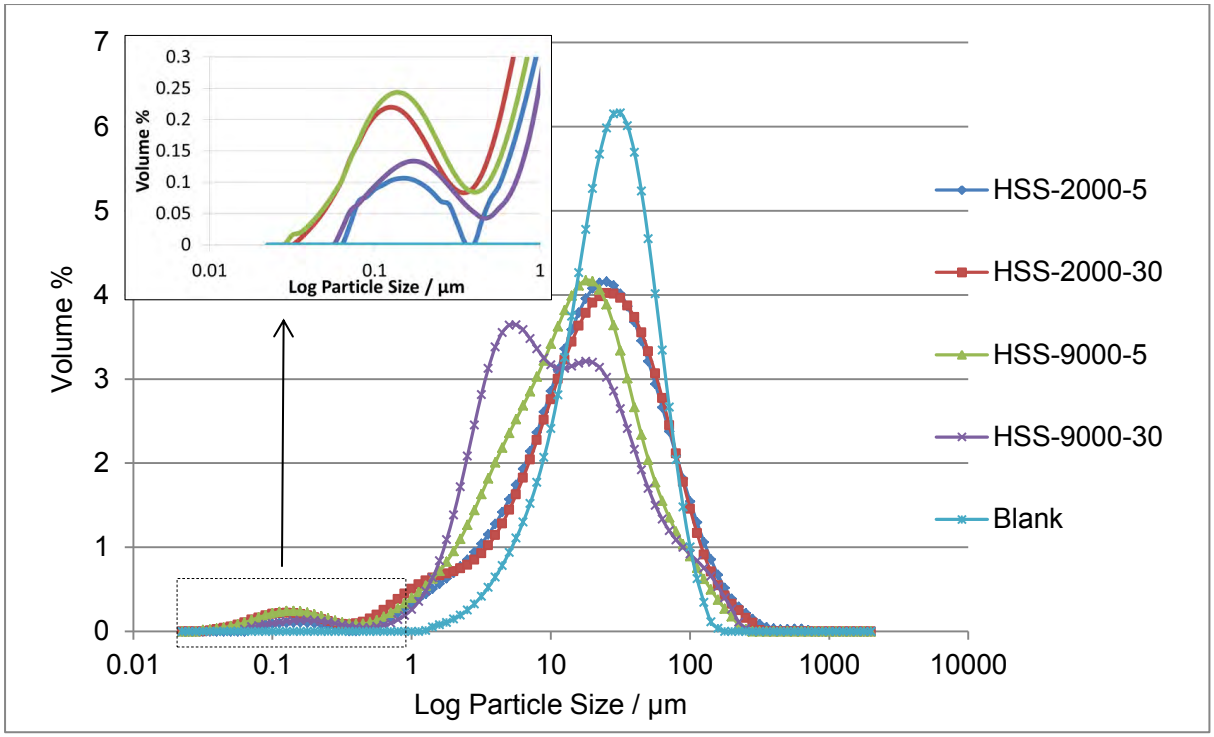

Figure 57: Particle size distributions for catalyst inks mixed using variable parameters of HSS between 0.1-10 000 µm (main plot) and 0.02-1 µm (insert).

It is very clear from the data that the high intensity mixing breaks down agglomerates and thus produces a catalyst ink with a large volume of small particles. This can be seen by the leftward shift of the HSS-9000-5 and HSS-9000-30 ParSD peaks, compared to the blank sample. At low intensity mixing (2000 rpm), time has a negligible effect on agglomerate size reduction. However, the effect of mixing time becomes more noticeable at higher mixing intensity. This result shows that mixing intensity is a dominating factor for HSS mixing technique with regards to particle size reduction. The mechanism of mixing as determined from the ParSD suggests that HSS rupture catalyst agglomerates during the dispersion process (adapted from mechanisms conceptualised by Özcan-Taskin et al., 2009; Zhang et al., 2012).

5.2.2.2. Catalyst Layer Morphology

SEM imaging was performed on the CL coated onto Teflon substrates for each of the mixing conditions outlined in the 2x2 factorial matrix, and shown in Figure 58. The HSS-2000-5 sample has a very cracked catalyst layer topography. Large number of cracks in the catalyst layer is indicative of vapours forcibly removed from the CL, suggesting that insufficient passages are available for solvent removal. Samples HSS-9000-5 and HSS-2000-30 show a more continuous CL and cracks are less apparent. It is observed that HSS-9000-5 display smaller bumps compared to HSS-2000-30 which are indicative of finer particle agglomerates as a result of the more aggressive mixing speed. Sample HSS-9000-30 presents a very smooth and continuous CL surface and seen from the 10 000 x magnification image, it has a very defined and distributed pore structure.

HSS-9000-5

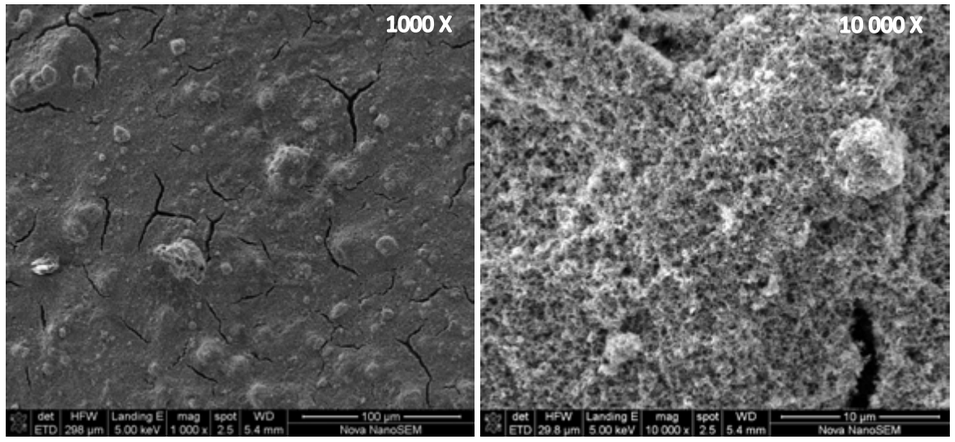

HSS-9000-30

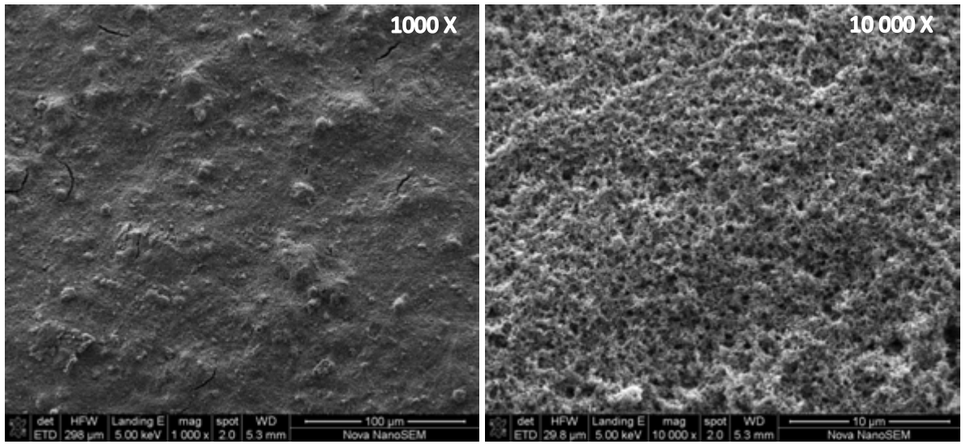

HSS-2000-5

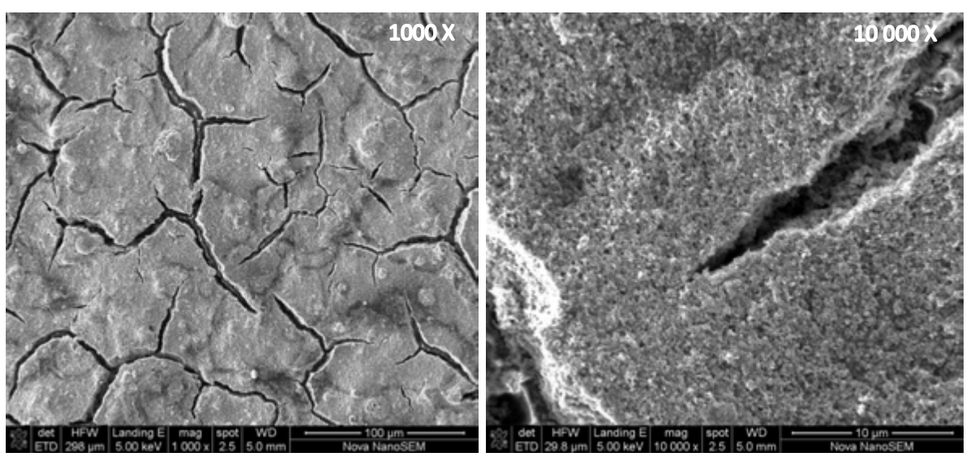

HSS-2000-30

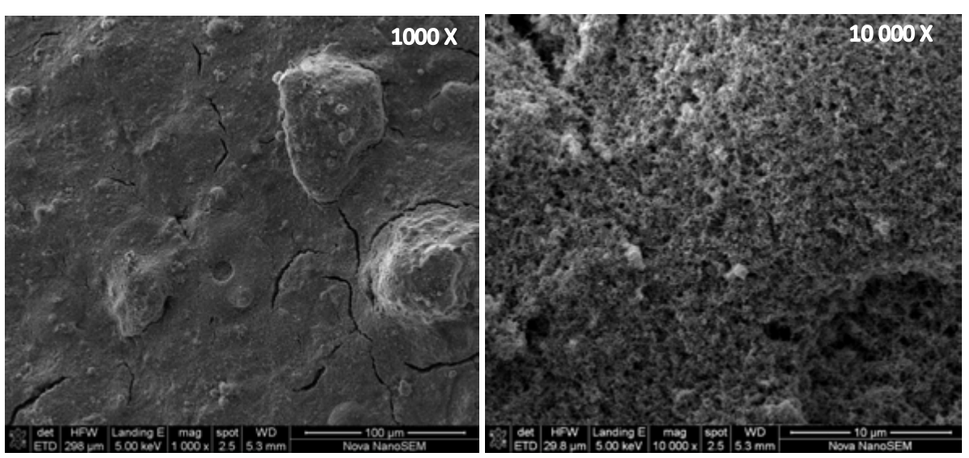

Figure 58: SEM analysis for CCSs produced by a variation in parameters (Figure 56) of the HSS mixing technique.

5.2.2.3. Distribution of Catalyst Layer Components

An EDX analysis was conducted on the surface of the CCS and the data is shown in

Table **17**.

HSS-9000-5	S	Pt	S:Pt
Mean (wt. %)	1.625	25.010	0.065
Stdev-S (wt. %)	0.101	0.629	0.0052

HSS-9000-5	S	Pt	S:Pt
Mean (wt. %)	1.625	25.010	0.065
Stdev-S (wt. %)	0.101	0.629	0.0052

HSS-2000-5	S	Pt	S:Pt
Mean (wt. %)	1.735	23.603	0.074
Stdev-S (wt. %)	0.091	0.509	0.0048

Table 17: EDX analysis showing the elemental distribution on the surface of a CCS produced using the HSS mixing technique

HSS-9000-30	S	Pt	S:Pt
Mean (wt. %)	1.683	26.153	0.064
Stdev-S (wt. %)	0.077	0.223	0.0033

HSS-2000-30	S	Pt	S:Pt
Mean (wt. %)	1.610	26.660	0.060
Stdev-S (wt. %)	0.123	0.484	0.0045

Four regions were analysed on each of the samples and shown in the data (

Table **17**) is the mean and standard deviation of S, Pt and Pt:S ratios. The data suggests that mixing time produces an enhanced dispersion of the CL components. The quantities of each element are identical in each of the data sets suggesting that HSS evenly disperses CL components, i.e. CL particles did not lump in all cases. At the higher end mixing condition (high dispersion and prolonged time) HSS-9000-30 produced superior mixing as the element ratio of S:Pt has the lowest Stdev-S of 0.0033 wt. %. This result suggests that a more aggressive and prolonged mixing when using HSS could produce an enhanced microstructural distribution of CL components.

HSS-9000-5	S	Pt	S:Pt
Mean (wt. %)	1.625	25.010	0.065
Stdev-S (wt. %)	0.101	0.629	0.0052

5.2.2.4. Catalyst Layer Pore Structure

PorSD was conducted for CL coated on PTFE for HSS mixing conditions, as indicated in the two-factorial design method (Figure 56). N_2 physisorption and Hg-Intrusion Porosimetry PorSD plots are shown in Figure 59 and Figure 60 respectively. These show the effect of catalyst ink mixing parameters on CL pore volume.

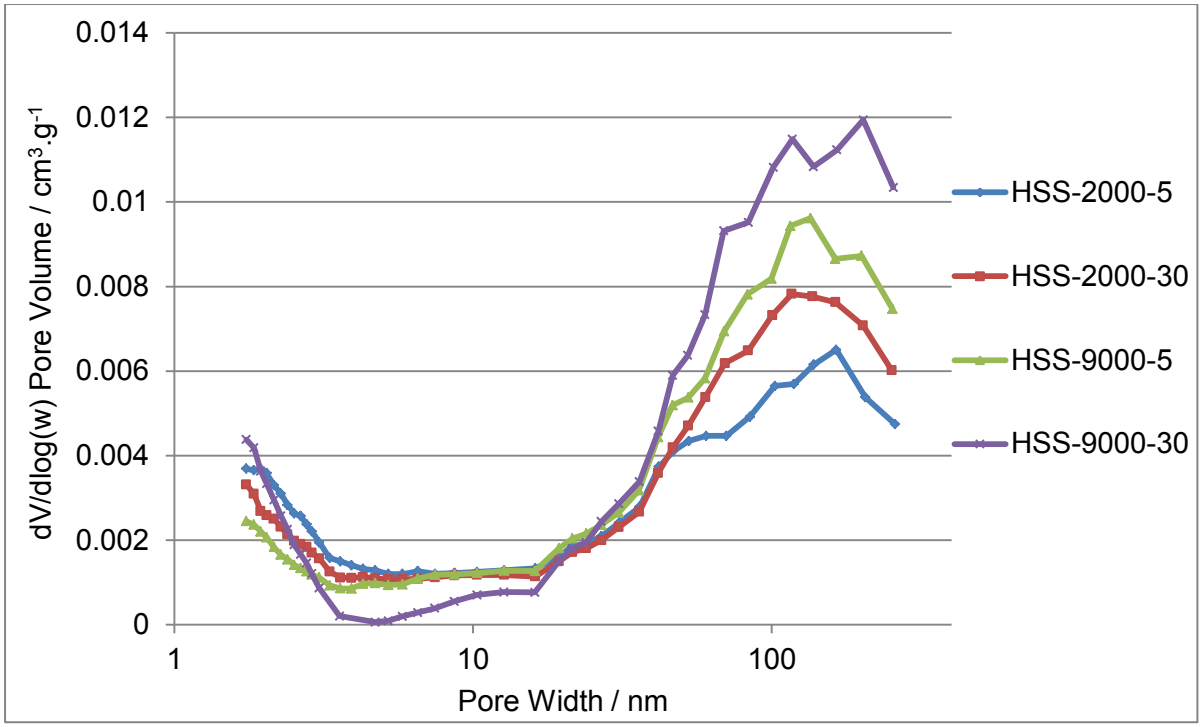

Figure 59: BJH Adsorption dV/dlog(w) Pore Volume for HSS mixed CL samples coated onto PTFE.

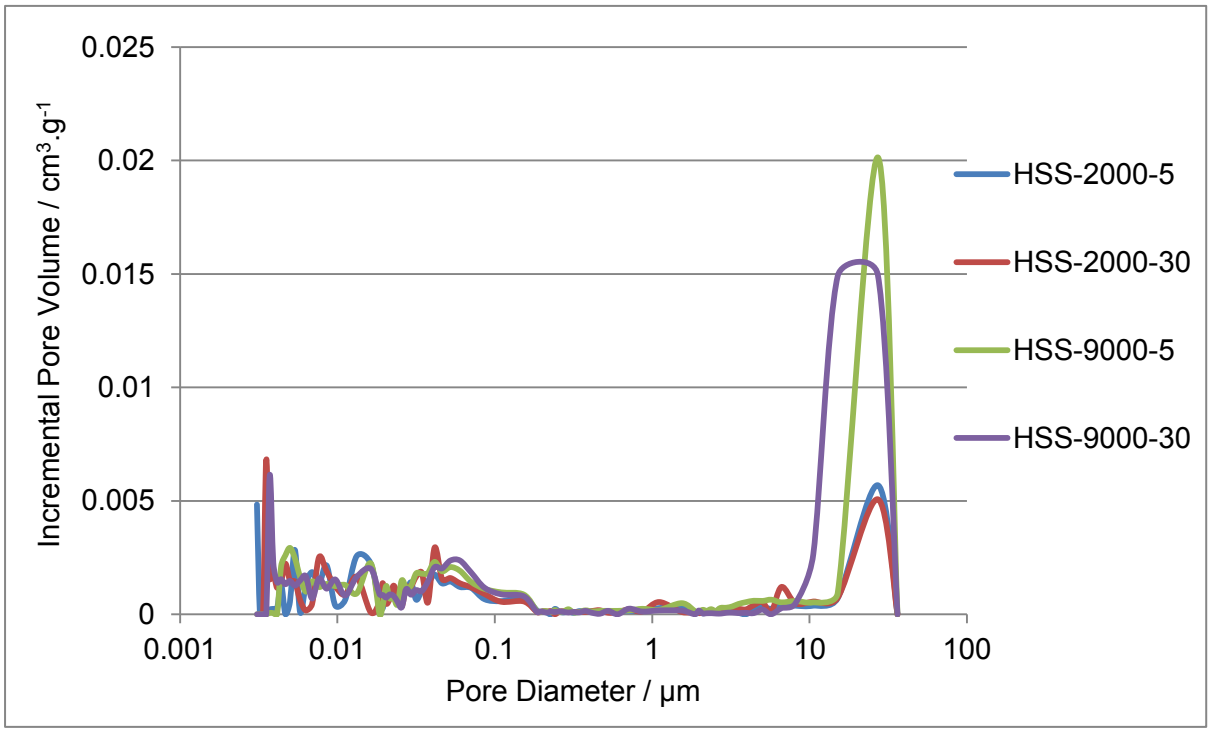

Figure 60: PorSD curves using Hg-Porosimetry for CCS prepared by HSS mixing technique. Mixing time and intensity has been varied according to Figure 56.

The figures below represents the 2 x 2 factorial matrix showing the **total pore volume** for CLs prepared using the HSS mixing technique using N_2 Physisorption (left) and Hg-Intrusion Porosimetry (right). The pore volume data is represented in a matrix array to simplify comparison.

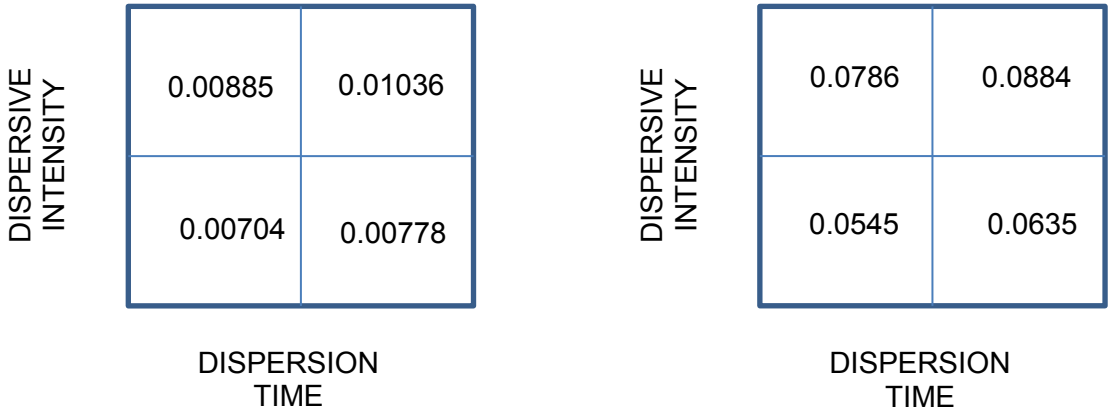

Figure 61: Left: BJH Adsorption cumulative volume of pores between 1.7 nm and 300 nm width / cm³.g-1 Right: Hg-Intrusion Porosimetry Pore volume for CL prepared using different mixing conditions for HSS.

PorSD obtained from N_2 Physisorption and Hg-intrusion are shown in Figure 59 and Figure 60 respectively. From the figures it can be seen, that the macro pore volumes are more affected by a change in mixing parameters followed by the meso-pores. Only small changes in the micro pores are observed. Mixing at low intensity (2000 rpm) produces low pore volume electrodes. However, high mixing intensity significantly increases pore volumes. Observed is that mixing intensity has a greater effect on the total pore volumes compared to mixing time as seen in Figure 61. High intensity mixing causes rapid de-agglomeration which results in very finely dispersed particles (seen by ParSD in Figure 57). Prior to mixing, the catalyst slurry has a low viscosity and therefore the mixing process is predominantly dependent on impact processes. However, prolonged mixing increases ink viscosity and shear forces become more important (Tadros, 1987). High shear forces allow stretching of ionomer, creating thinner Nafion films which results in a higher exposed agglomerate surface area and consequently, increases pore volume (depicted in Figure 44).

5.2.2.5. Electrochemical Performance Characterisation

The i-E curves in Figure 62 shows the performance comparison of MEAs with CLs manufactured at different HSS mixing parameters.

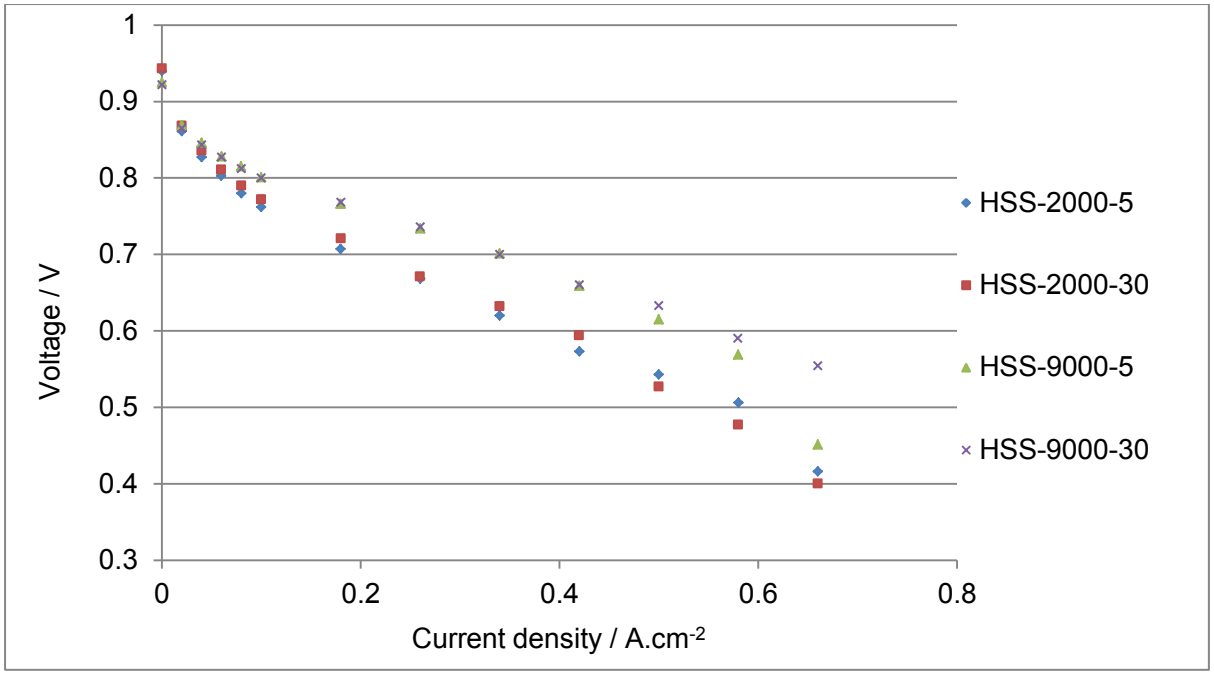

Figure 62: H_2/Air Polarisation curves for MEAs prepared by inks mixed using variable parameters of HSS. N/C = 1 for all electrodes. Testing conditions: T_{cell}=80˚C, RH=100%, gases at 1 bar using N212 membrane and SGL24BC GDL.

Shown below are the Nyquist plots of MEAs prepared using the HSS mixing technique. These were obtained and plotted using EIS data, which was conducted immediately after polarisation tests.

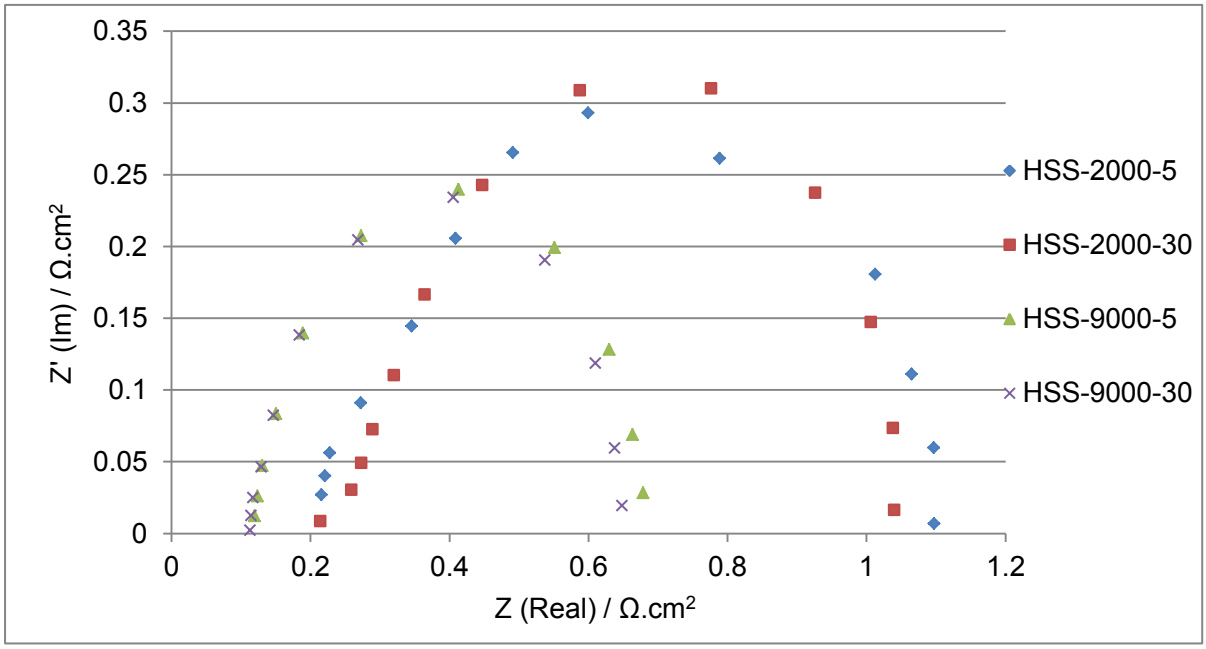

Figure 63: Nyquist plot at 100 mA.cm^{-2} for MEAs prepared by inks mixed using variable parameters of HSS. N/C = 1 for all electrodes. Testing conditions: Frequency range: 20000 – 0.1 Hz, T_{cell}=80˚C, RH=100%, gases at 1 bar using N212 membrane and SGL24BC GDL.

Shown in the table below is the Pt-loading for each tested sample; the calculated ECSA; and the charge transfer resistance obtained from the Nyquist plots.

Table 18: ECSA and charge transfer resistance for MEAs prepared by inks mixed using HSS

Sample Name	Anode Loading ($mg.cm^{-2}$)	Cathode Loading ($mg.cm^{-2}$)	ECSA ($m^2.g^{-1}$)	EIS at 100mA.cm^{-2} ($\Omega.cm^2$)
HSS-2000-5	0.456	0.525	27.180	0.886
HSS-2000-30	0.432	0.512	35.400	0.825
HSS-9000-5	0.435	0.549	29.574	0.560
HSS-9000-30	0.3632	0.542	29.398	0.532

The i-E performance curves for MEAs prepared using HSS mixing are shown in Figure 62. CLs prepared at 9000 rpm show superior performance to those prepared at 2000 rpm. Mixing intensity had a distinct impact on the ohmic resistance which could be a direct effect of the difference in electrode porosity contributing to a change in the conductive pathways. The effect of mixing time on MEA performance is negligible; however, HSS-9000-5 presents significant mass transfer losses at 0.55 V which is a result of lower total porosity compared to HSS-9000-30. ECSA and charge transfer resistance data are shown in Figure 63 and Table 18. High intensity mixing enhances the formation of the ionomer network due to the high shear forces stretching ionomer. This suggests an improved three phase contact at the agglomerate surface; and enhanced ionic conduction, seen by charge transfer and ohmic resistances respectively. The ECSA measurement does not directly compare to the measured performance and might be a consequence of conducting the measurement externally and at different conditions to polarisation tests. However, ECSA does seem to decrease going from lower to higher end mixing conditions.

5.2.3. UH of Catalyst Inks

During UH, ultrasonic pulses produce high energy cavitation events which generate immense shear and impact forces in the catalyst ink mixture. Figure 64 shows the 2 x 2 factorial design matrix depicting the parameters by which the study of UH was based upon.

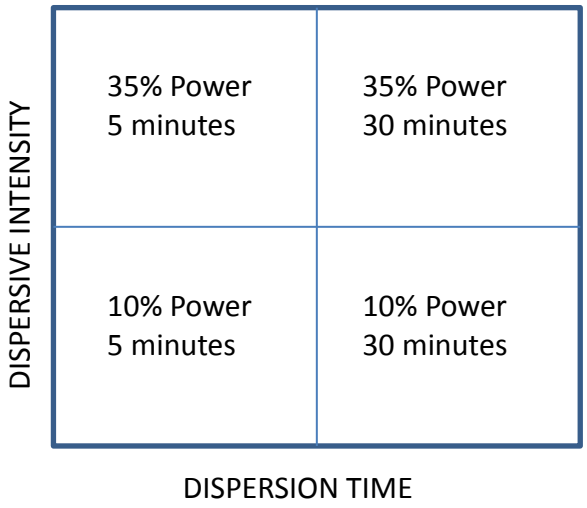

Figure 64: 2 x 2 factorial design matrix depicting the magnitudes of relative mixing intensity and mixing time in evaluating the effect of UH on CL formulation and PEMFC performance

5.2.3.1. Catalyst Ink Particle Size

Particle size analysis shown in Figure 65 depicts the dispersions produced after UH at different parameter settings.

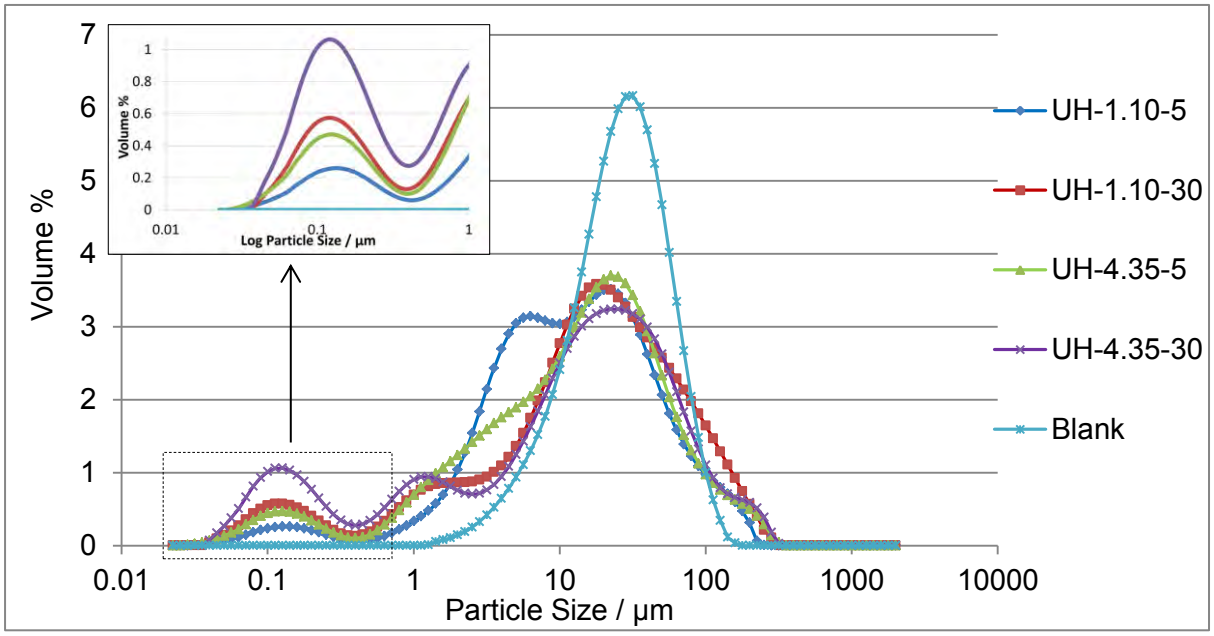

Figure 65: Particle size distributions for catalyst inks mixed using variable parameters of UH between 0.1-10 000 µm (main plot) and 0.02-1 µm (insert).

As ultrasonic power and dispersion time increase, particle size reduction is enhanced as seen in Figure 65. The shoulder at 5 µm diminishes as both ultrasonic power and dispersion time is increased. However, it appears that mixing time has a greater effect on particle size reduction. This is observed by the differences in volume % between UH-1.10-5 and UH-1.10-30 being much greater than UH-1.10-5 and UH-4.35-5, and similarly for the difference at 35% power input. From the data we deduce that UH has an extremely significant effect on particle size reduction as it reduced agglomerates to less than 1 µm. Adapting the mechanisms conceptualised by Özcan-Taskin et al., (2009) and Zhang et al., (2012); ultrasonic dispersion causes an erosive particle size reduction as observed by the bimodal ParSD curves for each setting, and correlates with findings stated by Hielscher, (2007). This is an effect of ultrasonic cavitation causing particle collision and shear dispersion (Suslick & Price, 1999). Cavitation explosions forces agglomerate particles to collide. Collisions are completely random and so are the shear forces generated in the ink mixture. This causes agglomerate particles to break down in an inhomogeneous manner, producing dispersions with a large particle size variation and therefore unstable catalyst inks. Thus UH is not a good technique to control agglomerate particle size as ultrasonic parameters are complex to adjust, also noted by Lindermeir et al., (2003).

5.2.3.2. Catalyst Layer Morphology

Structural characterisation of the CL topography using SEM is shown in Figure 66. At 1000 x magnification, the images show that a more uniform CL surface is achieved at higher ultrasonic power. The protrusions from UH-1.10-5 CL are very apparent and are characteristic of the larger particle sizes. At 10 000 x magnification, pore structures are quite similar however, appears more uniform for samples at high intensity mixing.

UH-4.35-5

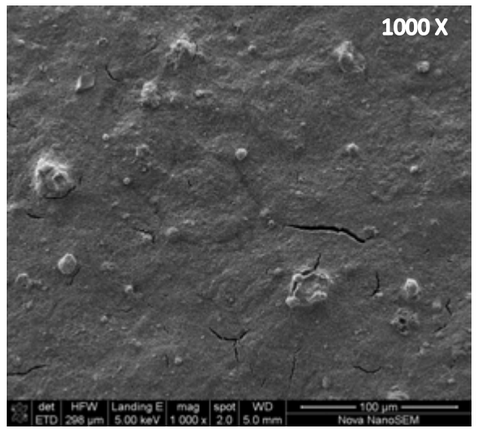

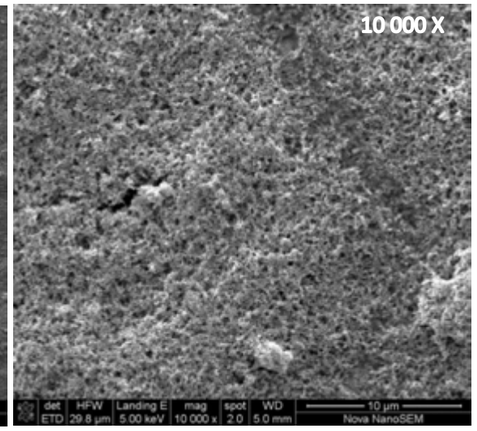

UH-4.35-30

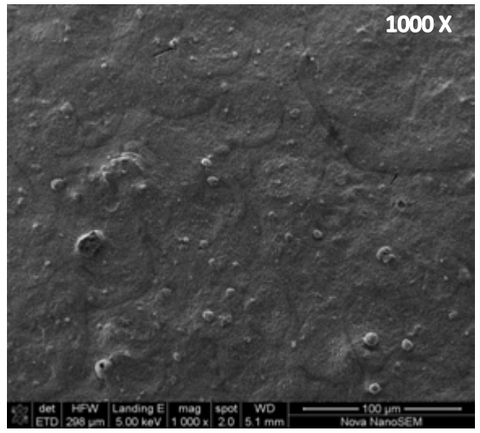

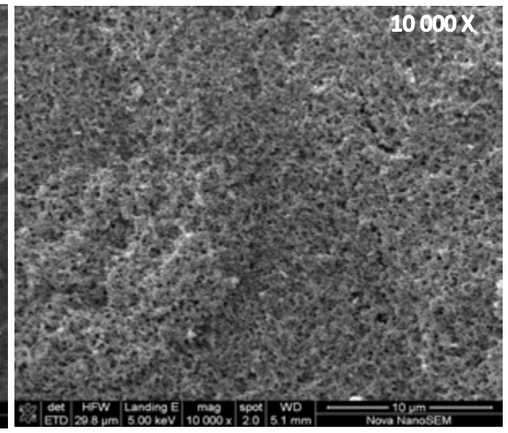

UH-1.10-5

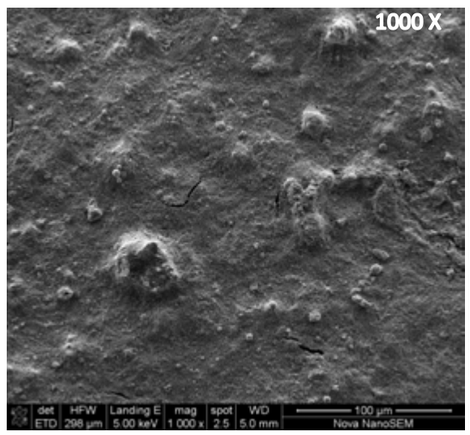

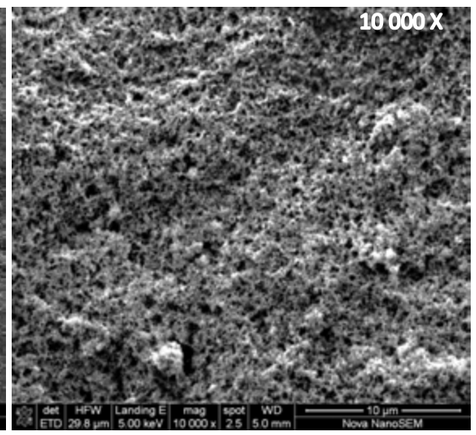

UH-1.10-30

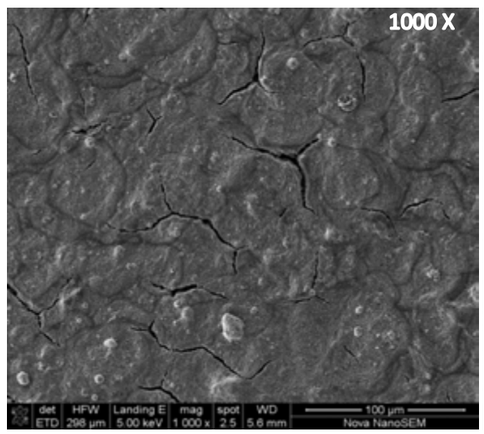

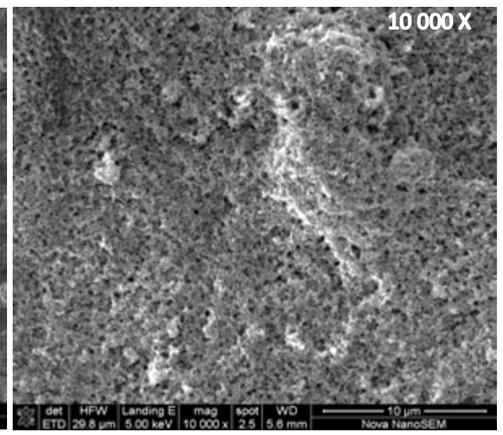

Figure 66: SEM images for CCSs produced by a variation in parameters of the UH mixing technique.

5.2.3.3. Distribution of Catalyst Layer Components

The effect of UH on CL component distribution is evaluated by EDX sampled at four points per dataset and summarised in
Table **19**.

Table 19: EDX analysis showing the elemental distribution on the surface of a CCS

UH-4.35-5	S	Pt	S:Pt
Mean (wt. %)	1.595	25.403	0.063
Stdev-S (wt. %)	0.095	0.432	0.0048

UH-4.35-30	S	Pt	S:Pt
Mean (wt. %)	1.603	26.080	0.061
Stdev-S (wt. %)	0.092	0.768	0.0032

produced using variable parameters of the UH mixing technique

UH-1.10-5	S	Pt	S:Pt
Mean (wt. %)	1.508	25.880	0.058
Stdev-S (wt. %)	0.111	0.522	0.0048

UH-1.10-30	S	Pt	S:Pt
Mean (wt. %)	1.698	26.315	0.065
Stdev-S (wt. %)	0.165	0.897	0.0082

The effect of UH on CL component distribution is evaluated by EDX sampled at four points per dataset and summarised in

Table **19**. The average quantities of Pt and S in all samples are almost identical; however, there are some differences in the distribution. Sample UH-1.10-5 and UH-4.35-5 has S: Pt ratio of 0.0048 wt. %. This suggests that the effect of ultrasonic mixing intensity in a on the

UH-4.35-5	S	Pt	S:Pt
Mean (wt. %)	1.595	25.403	0.063
Stdev-S (wt. %)	0.095	0.432	0.0048

UH-4.35-30	S	Pt	S:Pt
Mean (wt. %)	1.603	26.080	0.061
Stdev-S (wt. %)	0.092	0.768	0.0032

distribution of CL components for a short time interval is negligible. However, when mixing time is increased, there is an observable difference in the level of component distribution when comparing UH-1.10-5 and UH-1.10-30 with S:Pt of 0.0048 wt. % and 0.0082 wt. %, respectively. Similarly, the effect of time is observed between UH-4.35-5 and UH-4.35-30. This suggests that the effect of mixing is more apparent over a longer mixing time. This is expected during ultrasonication as no mechanical movement is induced (eg. Using a shaft), hence longer time intervals allow the system to naturally distribute, an effect of cavitation. Ultimately, more intense mixing and longer mixing time produced the most distributed catalyst layer as seen in UH-4.35-30.

5.2.3.4. Catalyst Layer Pore Structure

PorSD was conducted for CL coated on PTFE for UH mixing conditions indicated in the two-factorial design method (Figure 64). N_2 physisorption and Hg-Intrusion Porosimetry PorSD plots are shown in Figure 67 and Figure 68 respectively. These show the effect of catalyst ink mixing parameters on CL pore volume.

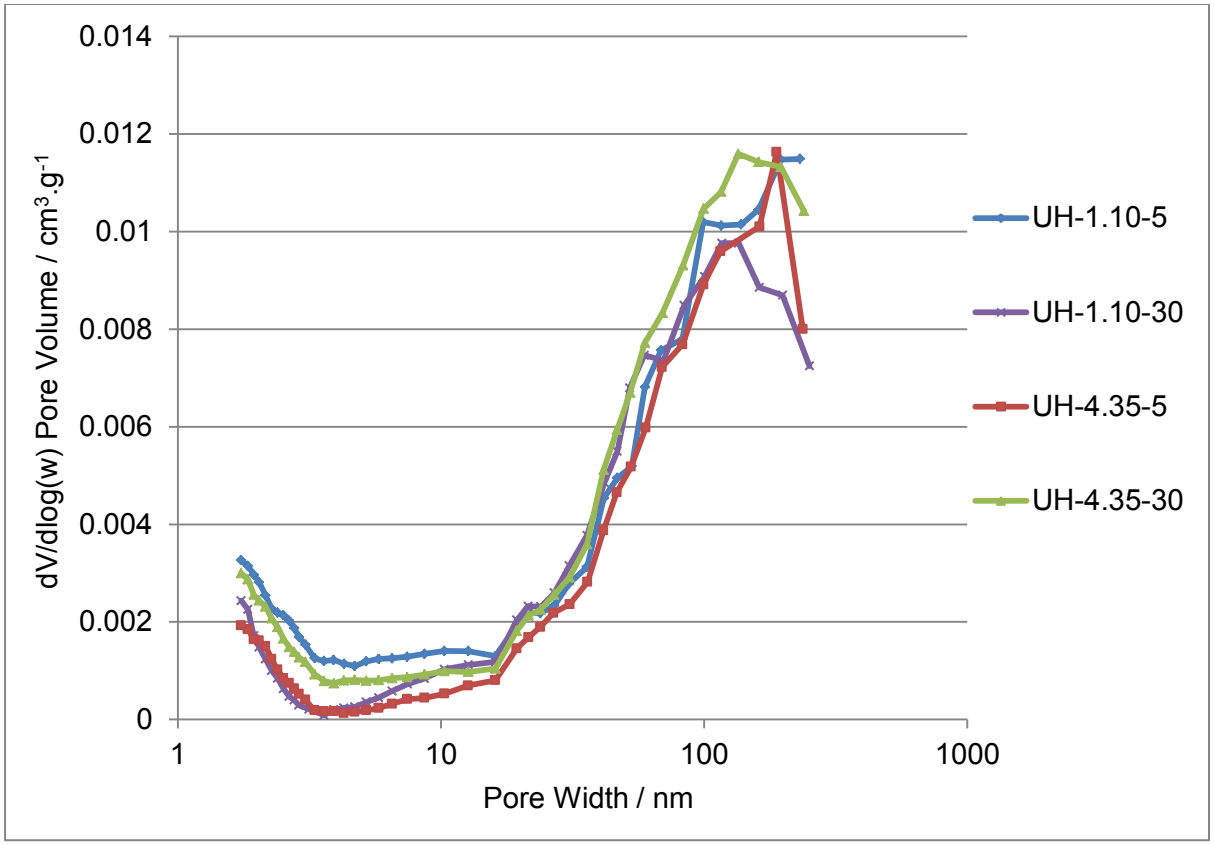

Figure 67: BJH Adsorption dV/dlog(w) Pore Volume for UH mixed CL samples coated onto PTFE.

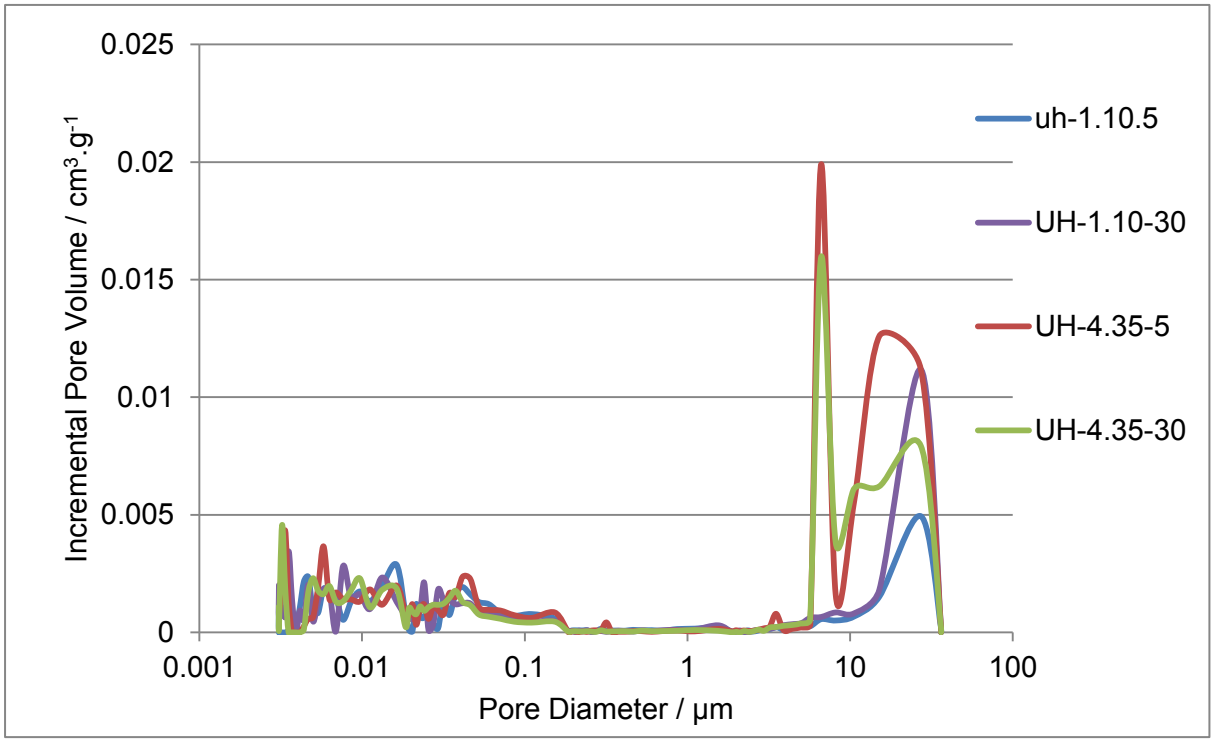

Figure 68: Pore Size distribution curves using Hg-Porosimetry for CCS prepared by UH mixing technique.

The figures below represents the 2 x 2 factorial matrix showing the **total pore volume** for CLs prepared for the UH mixing technique using N_2 Physisorption (left) and Hg-Intrusion Porosimetry(right). The pore volume data is represented in a matrix array to simplify comparison.

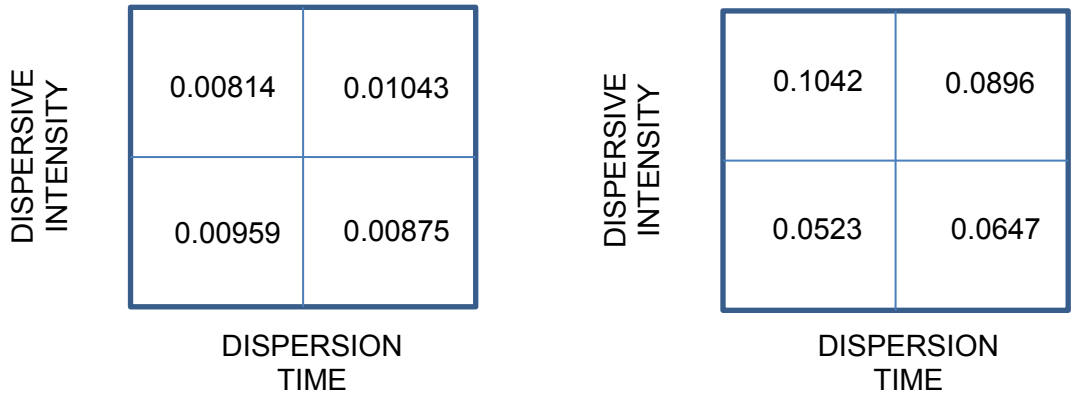

Figure 69 : Left: N2 physisorption and Right: Hg-Intrusion Porosimetry Data for CL prepared by variable parameters according to Figure 64 of UH showing the total volume in each CL.

Pore volume information conducted by N_2 physisorption for UH samples are shown in Figure 67. It is observed that micro and meso pores are not much affected by a change in ultrasonic parameters. No clear trend is observed on the influence of UH mixing parameters on pore volume. However, the combination of the data shown in Figure 68 and Figure 69 suggests that a higher dispersive intensity increases CL pore volumes, particularly the macro pores. This could be an effect of ionomer dispersion elongating Nafion fibres at elevated power inputs producing high shear forces. The effect of elevated temperatures at higher mixing intensity may also play a role to the alteration of Nafion morphology and in effect, change the permissible placement of Nafion within the agglomerate.

5.2.3.5. *Electrochemical Performance Characterisation*

The i-E curves in Figure 70 shows the performance comparison of MEAs with CLs manufactured at different UH mixing parameters.

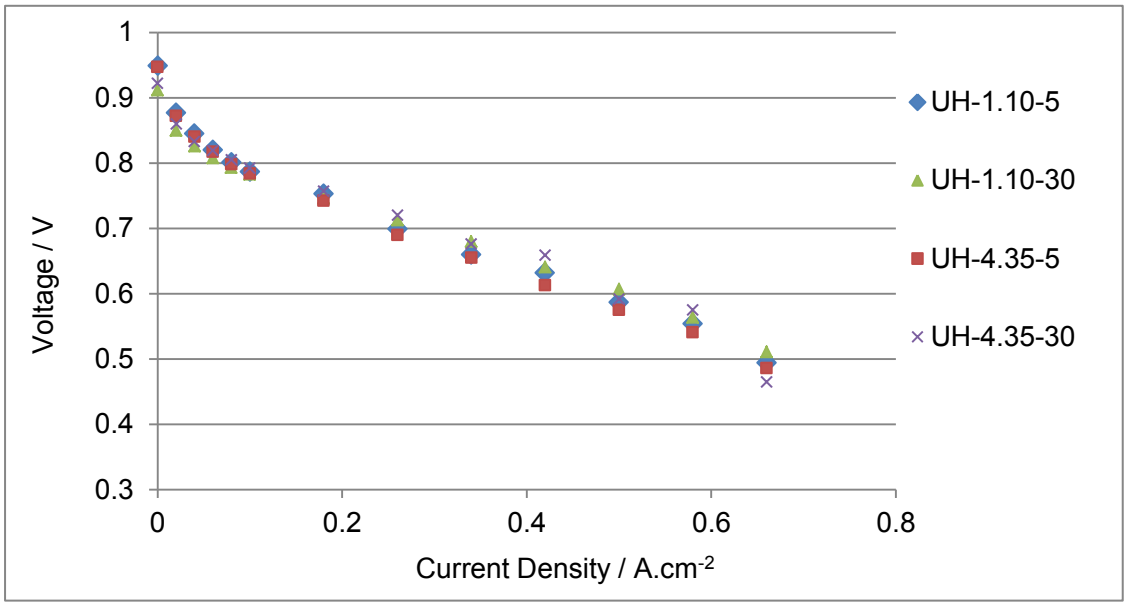

Figure 70: H_2/Air Polarisation curves for MEAs prepared by inks mixed using variable parameters of UH. N/C = 1 for all electrodes. Testing conditions: T_{cell}=80˚C, RH=100%, gases at 1 bar using N212 membrane and SGL24BC GDL.

Shown below are the Nyquist plots of MEAs prepared using the UH mixing technique. These obtained plotted using EIS data which was conducted immediately after polarisation tests.

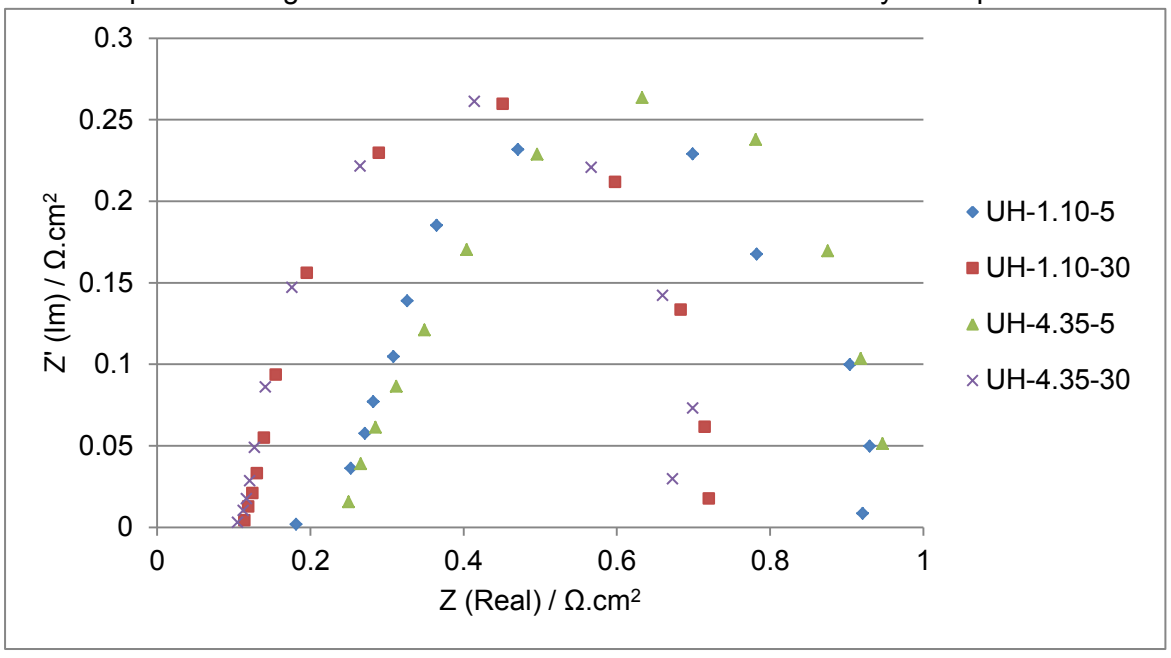

Figure 71: Nyquist plot at 100 mA.cm^{-2} for MEAs prepared by inks mixed using variable parameters of UH. N/C = 1 for all electrodes. Testing conditions: Frequency range: 20000 – 0.1 Hz, T_{cell}=80˚C, RH=100%, gases at 1 bar using N212 membrane and SGL24BC GDL.

Shown in the table below is the Pt-loading for each tested sample; the calculated ECSA; and the charge transfer resistance obtained from the Nyquist plots.

Table 20: ECSA and charge transfer resistance for MEAs prepared by inks mixed by UH

Sample Name	**Anode Loading ($mg.cm^{-2}$)**	**Cathode Loading ($mg.cm^{-2}$)**	**ECSA ($m^2.g^{-1}$)**	**EIS at $100mA.cm^{-2}$ ($\Omega.cm^2$)**
UH-1.10-5	0.41	0.59	31.54	0.739
UH-1.10-30	0.40	0.50	26.99	0.609
UH-4.35-5	0.42	0.55	28.01	0.669
UH-4.35-30	0.42	0.55	26.93	0.587

There is no significant performance difference when changing UH parameters as shown in Figure 70. However, UH-4.35-30 shows a relatively high performance in the ohmic region (0.5 V – 0.75 V). Nyquist plots in Figure 71 shows that catalyst inks dispersed for prolonged period of time produce a low contact resistance. This performance difference could be an effect of the nature of the catalyst layer formation after mixing. ParSD shows that catalyst inks dispersed for prolonged time period have smaller particles. Smaller particles have a higher total contact area as compared to larger particles. Improved particle contact could thus lead to enhancing the bulk transport of charge in the CL. The EIS data also shows that a higher mixing time improves charge transfer in the CL. A decrease in the ECSA is observed, which could be an effect of the high intensity ultrasonic pulses delaminating Pt from the support, previously observed by Pollet & Goh, (2014).

Ultimately, inks dispersed with higher ultrasonic power for a prolonged time period produces catalyst inks with a large ParSD range. This forms a homogeneous dispersion of CL components and produces a uniform CL topography. Also, high pore volumes can be achieved when ultrasonic intensity is increased; charge transfer is enhanced and low CL ohmic resistance is achieved at high dispersion parameters.

6. Summary of Results

The primary objective of this study was to investigate the effects mixing procedures have on CL formulation and PEMFC performance. This was done by investigating three different mixing methods namely: BM, HSS and UH. The basis for selecting these techniques was that they are widely used on a laboratory scale and to an extent industrially; and that these techniques use different mechanical processes for dispersion. Physical and electrochemical characterisation of the catalyst layer was conducted extensively in order to bridge the link between preparation and performance.

6.1. Effect of Different Mixing Procedures on CL Formulation and PEMFC Performance

In the first part of the study a comparison was drawn between the three mixing techniques. Mixing was conducted at high dispersive intensities for 30 minutes and the samples were denoted: BM-3000-30, HSS-9000-30 and UH-4.35-30, as shown in Table 10. The ParSD showed that all techniques achieved a significant particle size difference in comparison to the unmixed catalyst ink. UH produced very large particle size range spanning 300 to 0.03 µm however, BM and HSS produced inks with 300 to 0.5 µm agglomerate distributions. This is due to high energy cavitation events during UH, causing interparticle collisions which results in the shift towards producing very fine dispersions. The data shows that narrow and nearly monomodal distributions are obtained with BM and HSS; however, large multimodal dispersions are obtained with UH and suggests catalyst inks here are unstable and not suitable for high throughput processing.

Temperatures were recorded every 5 minutes over the 30 minute mixing period and T vs. t plotted for each of the techniques (shown in Figure 40). Temperature increased linearly with time, where HSS and UH achieved a temperature change of >40°C whilst the BM temperature essentially remained unchanged. It has been reported that Nafion morphology is largely dependent on temperature and transforms from rigid-rod like structures to elongated, entangled and interconnected structures when temperature is increased (Yaun et al., 2012a). In effect, the increase in catalyst ink temperature would then change the morphology of Nafion during HSS and UH, however the extent of change has not been determined. SEM characterisation shows no difference in topography between mixing techniques however at 10 000 x magnification, evenly distributed pore structures are observed for HSS and UH CLs, unlike BM. EDX analysis conducted showed the Stdev-S of S:Pt, as a representation of the dispersion of catalyst layer components. The three mixing methods all achieved equivalent dispersions likely due to the high intensity and mixing times they were conducted at.

The CL consists of three distinct regions of pores being micropores (<10 nm), mesopores (between 10 nm and 1000 nm) and macropores (>1000 nm). In order to span across the entire pore range N_2 physisorption and Hg-porosimetry was used for pore volume analysis. It was observed that macro pores contribute to almost 90 % of the total CL pore volume. BM particularly had significantly lower secondary pores (meso and macro pores) as compared to HSS and UH. BM produces very high impact collisions and grinding during comminution. This could result in a significant reduction in Nafion size. As BM ink temperature remains low Nafion does not elongate (Yaun et al., 2012a) and fibres remain small which could promote

filling and blocking of secondary pores, as observed. Due to the increased CL porosity and enhanced ionomer network, gaseous diffusion and ionomer conduction paths are enhanced. This promotes H^+ transfer and therefore improves PEMFC performance, as observed for HSS and UH. This is particularly seen by reduced ohmic losses and improved charge transfer during in-situ electrochemical characterisation. Ultimately, the MEA with CL prepared using HSS showed the maximum PEMFC performance.

6.2. Effect of Mixing Parameters on CL Quality and PEMFC Performance

In order to develop a better understanding of the role mixing techniques play during catalyst ink mixing, each mixing method was studied independently. In this study the effect of the individual mixing techniques were determined by varying mixing intensity and mixing time in a 2 x 2 factorial design. The two mixing parameters, intensity and time, were chosen such that distinguishable low and high mixing end conditions could be studied.

6.2.1. BM of Catalyst Inks

Bead-particle collisions generate impact forces during bead milling. Throughout catalyst ink mixing, these forces grind carbon agglomerates to smaller particle sizes. Monomodal ParSD curves suggest that the BM rupture agglomerates during dispersion. The results show that particle size reduction is dominated by the rate of agitation. The higher end mixing condition produces even CL topography and well distributed CL components. The data shows that in the initial stages of BM, ionomer films undergo shear dispersion and well distributed, and interconnected Nafion films form. However, at prolonged milling times, Nafion films are grinded down to such an extent that the interconnected ionomer networks diminish. Thus, prolonged milling times results in Nafion filling and blocking secondary pores. This is more observable in the macro pore range as larger pores are more susceptible to blocking. The diminished ionomer network observed when milling for 30 minutes, results in a decrease in charge transfer resistance and therefore lower PEMFC performance.

6.2.2. HSS of Catalyst Inks

High shear stirring is characterised by very large rotational speeds, high shear rates and highly localised energy dissipation rates at the mixing head (Zhang et al., 2012). ParSD curves suggest that the mechanism of mixing during HSS of catalyst inks is a result of agglomerate rupture. The results shows that particle size reduction is controlled by the rate of high shear agitation. High end mixing conditions produced even CL topography and a well distributed pore structure, as seen by SEM images (Figure 58). EDX analysis shows that extended mixing time improves catalyst ink distribution. Prior to mixing, the catalyst slurry has a low viscosity and therefore the dispersion process is predominantly dependant on impact processes. However, prolonged mixing increases ink viscosity and shear forces become more important (Tadros, 1987). High shear forces promote Nafion stretching and therefore creating thinner ionomer films. This results in a higher exposed agglomerate surface area and consequently, increases pore volume. During HSS secondary pore volumes increase as both mixing time and intensity increases. Mixing intensity however has a greater effect on the CL pore structure. PEMFC performance is significantly enhanced at higher shear rates. High agitation rates are characteristic of higher energy inputs. This increases shear forces and catalyst ink temperature, resulting in enhanced interconnected Nafion network. High temperatures also improves Nafion adhesion to catalyst agglomerates.

Consequently, this significantly reduced ohmic resistance and improved charge transfer, as seen during EIS measurement.

6.2.3. UH of Catalyst Inks

UH dispersion time controls the rate of particle size reduction. Bimodal ParSD is representative of erosive agglomerate dispersion UH. Large dispersion ranges produced here are not favourable when controlling particle size. CL topography observed under SEM shows no significant changes between the mixing parameters observed. When mixing at the higher end parameter, CL components evenly distributes, as shown by the EDX measurement. High ultrasonic power input significantly increases secondary pore volume. Ohmic resistance and charge transfer improves with prolonged UH times. The improvement in ohmic resistance is likely due to a higher total contact area amongst catalyst agglomerates; as smaller particles are produced at extended sonication times.

During BM and HSS, predictable trends for S:Pt Stdev-S were observed. As mixing intensity and time increases, S:Pt value also increases. This is an effect of improved dispersion with increased mixing energy. However, in UH, this trend is erratic and is unpredictable. This could be attributed to the large ParSD range, hence producing unstable inks. As previously noted, unstable inks are more likely to result in irreproducible CLs. From this, UH is not recommended for high throughput MEA processing.

7. Major Findings and Observations

The resulting ParSD is dependent on both mixed materials and mixing equipment. Using ParSD, the mechanism of particle breakup can be determined by observing the type and progression of the ParSD curves over mixing time (Özcan-Taskin et al., 2009; Zhang et al., 2012). Therefore, depending on the desired ink formulation, this can be used as a tool to determine which materials and mixing equipment are best suited. In this study, the result shows that monomodal distribution produced by BM and HSS is favourable for controlling catalyst particle size, as they rupture agglomerates during dispersion.

The results show that the temperature of the catalyst ink mixture is a considerable factor during mixing. Temperatures should therefore be monitored, as it plays a significant role to the morphology of Nafion. A further study in this area is recommended.

The general trend observed was that prolonged mixing time and agitation rates produce a well-defined CL topography and improves dispersion of CL components. However, extended mixing time in BM was an exception in this regard.

The ratio of S:Pt serves as a representative of the availability of Nafion to the platinum catalyst. Stdev-S of S:Pt serves as a unifying term representing the level of distribution for both catalyst and ionomer within the CL. The numerical significance of Stdev-S proved to consistently respond to the level of dispersion and, therefore could be a useful tool to characterise the distribution of CL components (hence CL reproducibility). However, this value does not give any suggestion to the placement of ionomer in the CL and therefore cannot be used to characterise performance.

Macro pores are responsible for almost 90% of the total pore volume in CLs. Nafion morphology plays a considerable role to the secondary pore volumes of catalyst layers. High agitation rates generally produce thin elongated Nafion films exposing higher agglomerate surface area and consequently, increases pore volume. Conversely, extended BM could result in breaking down of Nafion films which lead to blockage of pores and thus, reduce pore volume.

A careful selection of mixing technique(s) and parameters can result in an improved PEMFC performance. High energy mixing produces an interconnected Nafion network which improves H^+ transfer. In the case of BM and HSS, a high mixing intensity is more beneficial however; prolong BM proved to be destructive. In the case of UH extended time had a greater effect on improving FC performance. The result show that ohmic resistance is likely dependant on catalyst particle size distribution as seen during UH inks. However, it is dependent on several other factors as well, making the effect that ParSD has on ohmic resistance difficult to control.

An observable loss in ECSA is obtained as mixing intensity increases. This applies for all mixing techniques. This might suggest that a higher mixing intensity delaminates Pt nanoparticles from the carbon support, resulting in a lower ECSA. This was previously observed by Pollet and Goh, 2014 during UH of catalyst inks. However, an overall performance improvement is still possible due to the influence of mixing on agglomerate pore structure and Nafion morphology. However, it should be noted that there are

inconsistencies in the ECSA measurement. This might be a consequence of conducting the measurement externally and at different conditions to polarisation tests.

Mixing effectively changes the catalyst agglomerate particle size, CL topography, ink dispersion and Nafion morphology. As a consequence, results show that mixing does influence PEMFC performance albeit, not significantly. Considering energy consumption, in this case BM uses the lowest energy, followed by UH and highest HSS. At a laboratory scale energies are insignificant however, becomes a substantial cost effect during high throughput MEA production. On a basis of energy input, BM would be the more feasible option. However, the mixing parameters should be effectively investigated prior to scale-up. Amongst the mixing techniques investigated BM is the easiest to scale-up. Therefore intuitive thinking and thorough research is required in when choosing mixing parameters/methods during the CL optimisation process.

8. Conclusions

Much more research is still required in the PEMFC space in order for it to become a viable and marketable energy generation source. Efficient management of resources and good leadership is imperative when trying to achieve any research objective. The only way FC will become a viable option in South Africa is through employing and developing skilful researchers with comprehensive knowledge in the field.

In this study, a large number of concerns were briefed relating to PEMFC development. Some of which are: CL and MEA manufacturability; CL characterisation; performance optimisation and ultimately, to gain a better insight into the MEA manufacturing process. Additional research ideas were acquired and could possibly be explored.

MEA characterisation could be enhanced by employing the use of alternative characterisation techniques. Ionomer structure and dispersion are major focal points in this study. It would therefore serve useful to be able to physically map the ionomer through staining or doping techniques; e.g.: Ag^{+} cation exchange using a suitable Ag source such as $AgNO_3$ (Uchida et al., 2006; Scheiba et al., 2008). Porosimetry is also a major study point. Useful insight could come from 3D-reconstruction of the catalyst layer and visualising pore structure under FIB-SEM (Ziegler et al., 2011; Singh et al., 2014).

Although changes in the CL has been observed after decaling (seen in Appendix A), in-situ performance data still show the effects of mixing. Microstructural changes to CL made after mixing is maintained; therefore the effects of decaling does not appear to be significant to the overall performance. However, this needs to be validated. Therefore to draw a more direct link between fabrication and performance, the study should be conducted (physical and in-situ characterisation) with the CL applied directly to the membrane. Dispersive processes are commonly studied as an individual technique however; many institutions use a combination of mixing equipment. In this study, the effect of mixing has been observed and it has been shown that mixing indeed influence CL formulation. Therefore, it would be useful to explore the use of a combination of mixing methods; a possible area for CL optimisation.

9. References

AimyBazylak 2015. *AimyBazylak.* Available: http://bazylak.mie.utoronto.ca/research/ [2016, January 06].

Alkire, R.C., Kolb, D.M. & Lipkowski, J. 2006. *Advances in electrochemical science and engineering.* John Wiley & Sons.

Allahyarov, E. & Taylor, P.L. 2008. Simulation study of the correlation between structure and conductivity in stretched nafion. *The Journal of Physical Chemistry B.* 113(3):610-617.

Baines, R. & Cope, G. 1968. Mixing and dispersion techniques. *Journal of the Society of Cosmetic Chemists.* 19(4):225.

Benitez, R., Soler, J. & Daza, L. 2005. Novel method for preparation of PEMFC electrodes by the electrospray technique. *Journal of Power Sources.* 151:108-113.

Berg, P., Novruzi, A. & Promislow, K. 2006. Analysis of a cathode catalyst layer model for a polymer electrolyte fuel cell. *Chemical Engineering Science.* 61(13):4316-4331.

Bladergroen, B., Su, H., Pasupathi, S., Linkov, V. 2012. Overview of Membrane Electrode Assembly Preparation Methods for Solid Polymer Electrolyte Electrolyzer. DOI:10.5772/52947.

Brandon, N.P., Skinner, S. & Steele, B.C. 2003. Recent advances in materials for fuel cells. *Annual Review of Materials Research.* 33(1):183-213.

Carrette, L., Friedrich, K. A. and Stimming, U. (2001), Fuel Cells – Fundamentals and Applications. Fuel Cells, 1: 5–39. doi: 10.1002/1615-6854(200105).

Chaparro, A., Folgado, M., Ferreira-Aparicio, P., Martín, A., Alonso-Álvarez, I. & Daza, L. 2010. Properties of catalyst layers for PEMFC electrodes prepared by electrospray deposition. *Journal of the Electrochemical Society.* 157(7):B993-B999.

Cheng, X., Yi, B., Han, M., Zhang, J., Qiao, Y. & Yu, J. 1999. Investigation of platinum utilization and morphology in catalyst layer of polymer electrolyte fuel cells. *Journal of Power Sources.* 79(1):75-81.

Chisaka, M. & Daiguji, H. 2006. Effect of glycerol on micro/nano structures of catalyst layers in polymer electrolyte membrane fuel cells. *Electrochimica Acta.* 51(23):4828-4833.

Cho, H.J., Jang, H., Lim, S., Cho, E., Lim, T., Oh, I., Kim, H. & Jang, J.H. 2011. Development of a novel decal transfer process for fabrication of high-performance and reliable membrane electrode assemblies for PEMFCs. *International Journal of Hydrogen Energy.* 36(19):12465-12473.

Cho, J.H., Kim, J.M., Prabhuram, J., Hwang, S.Y., Ahn, D.J., Ha, H.Y. & Kim, S. 2009. Fabrication and evaluation of membrane electrode assemblies by low-temperature decal methods for direct methanol fuel cells. *Journal of Power Sources.* 187(2):378-386.

Chun, Y., Kim, C., Peck, D. & Shin, D. 1998. Performance of a polymer electrolyte membrane fuel cell with thin film catalyst electrodes. *Journal of Power Sources.* 71(1):174-178.

Cindrella, L., Kannan, A., Lin, J., Saminathan, K., Ho, Y., Lin, C. & Wertz, J. 2009. Gas diffusion layer for proton exchange membrane fuel cells—A review. *Journal of Power Sources.* 194(1):146-160.

Conley, R.F. Ed. 1996. *Practical Dispersion: A Guide to Understanding and Formulating Slurries*. Canada: Wiley-VCH.

Cooper, K. & Smith, M. 2006. Electrical test methods for on-line fuel cell ohmic resistance measurement. *Journal of Power Sources.* 160(2):1088-1095.

DOE, U. 2007. *DOE Cell Component Accelerated Stress Test Protocols for PEM Fuel Cells.*

Eikerling, M. & Kornyshev, A. 1998. Modelling the performance of the cathode catalyst layer of polymer electrolyte fuel cells. *Journal of Electroanalytical Chemistry.* 453(1):89-106.

Felix, C., Jao, T., Pasupathi, S. & Pollet, B.G. 2013. Optimisation of electrophoretic deposition parameters for gas diffusion electrodes in high temperature polymer electrolyte membrane fuel cells. *Journal of Power Sources.* 243:40-47.

Fernandez, R., Ferreira-Aparicio, P. & Daza, L. 2005. PEMFC electrode preparation: influence of the solvent composition and evaporation rate on the catalytic layer microstructure. *Journal of Power Sources.* 151:18-24.

Fischer, A., Jindra, J. & Wendt, H. 1998. Porosity and catalyst utilization of thin layer cathodes in air operated PEM-fuel cells. *Journal of Applied Electrochemistry.* 28(3):277-282.

Franck, A. 2015. *Understanding Rheology of Structured Fluids.* Available: http://www.tainstruments.com/pdf/literature/AAN016_V1_U_StructFluids.pdf.

Franco, A.A. 2013. *Polymer Electrolyte Fuel Cells: Science, Applications, and Challenges.* CRC Press.

Frey, T. & Linardi, M. 2004. Effects of membrane electrode assembly preparation on the polymer electrolyte membrane fuel cell performance. *Electrochimica Acta.* 50(1):99-105.

Gomadam, P.M. & Weidner, J.W. 2005. Analysis of electrochemical impedance spectroscopy in proton exchange membrane fuel cells. *International Journal of Energy Research.* 29(12):1133-1151.

Haile, S.M. 2003. Fuel cell materials and components. Acta Materialia. 51(19):5981-6000.

Harvey, D., Pharoah, J. & Karan, K. 2008. A comparison of different approaches to modelling the PEMFC catalyst layer. *Journal of Power Sources.* 179(1):209-219.

Harrison, R. 1993. *Protein purification process engineering.* CRC Press.

He, Q., Suraweera, N.S., Joy, D.C. & Keffer, D.J. 2013. Structure of the Ionomer Film in Catalyst Layers of Proton Exchange Membrane Fuel Cells. *The Journal of Physical Chemistry C.* 117(48):25305-25316.

Hielscher, T. 2007. Ultrasonic production of nano-size dispersions and emulsions.

Hsu, C. & Wan, C. 2003. An innovative process for PEMFC electrodes using the expansion of Nafion film. *Journal of Power Sources.* 115(2):268-273.

Huang, D., Yu, P., Liu, F., Huang, S., Hsueh, K., Chen, Y., Wu, C., Chang, W. et al. 2011. Effect of Dispersion Solvent in Catalyst Ink on Proton Exchange Membrane Fuel Cell Performance. *International Journal of Electrochemical Science.* 6(2011): 2551 - 2565

Jang, J.H., Jeon, S., Cho, J.H., Kim, S., Lee, S., Cho, E., Kim, H., Han, J. et al. 2009. Complex capacitance analysis of ionic resistance and interfacial capacitance in PEMFC and DMFC catalyst layers. *Journal of the Electrochemical Society.* 156(11):B1293-B1300.

Jung, C., Kim, W. & Yi, S. 2012. Optimization of catalyst ink composition for the preparation of a membrane electrode assembly in a proton exchange membrane fuel cell using the decal transfer. *International Journal of Hydrogen Energy.* 37(23):18446-18454.

Kim, H., Subramanian, N.P. & Popov, B.N. 2004. Preparation of PEM fuel cell electrodes using pulse electrodeposition. *Journal of Power Sources.* 138(1):14-24.

Kim, K., Lee, K., Kim, H., Cho, E., Lee, S., Lim, T., Yoon, S.P., Hwang, I.C. et al. 2010. The effects of Nafion® ionomer content in PEMFC MEAs prepared by a catalyst-coated membrane (CCM) spraying method. *International Journal of Hydrogen Energy.* 35(5):2119-2126.

Kopeliovich, D. 2015. *SubsTech.* Available: http://www.substech.com/dokuwiki/doku.php?id=homogenization.

Larminie, J., Dicks, A. & McDonald, M.S. 2003. *Fuel cell systems explained.* Wiley New York.

Lee, S., Mukerjee, S., McBreen, J., Rho, Y., Kho, Y. & Lee, T. 1998. Effects of Nafion impregnation on performances of PEMFC electrodes. *Electrochimica Acta.* 43(24):3693-3701.

Li, G. & Pickup, P.G. 2003. Ionic conductivity of PEMFC electrodes effect of Nafion loading. *Journal of the Electrochemical Society.* 150(11):C745-C752.

Liang, X., Pan, G., Xu, L. & Wang, J. 2015. A modified decal method for preparing the membrane electrode assembly of proton exchange membrane fuel cells. *Fuel.* 139:393-400.

Lim, C., Allen, R. & Scott, K. 2006. Effect of dispersion methods of an unsupported Pt-Ru black anode catalyst on the power performance of a direct methanol fuel cell. *Journal of Power Sources.* 161(1):11-18.

Lindermeir, A., Rosenthal, G., Kunz, U. & Hoffmann, U. 2004. On the question of MEA preparation for DMFCs. *Journal of Power Sources.* 129(2):180-187.

Litster, S. & McLean, G. 2004. PEM fuel cell electrodes. *Journal of Power Sources.* 130(1):61-76.

Ma, S., Chen, Q., Jøgensen, F.H., Stein, P.C. & Skou, E.M. 2007. 19 F NMR studies of Nafion™ ionomer adsorption on PEMFC catalysts and supporting carbons. *Solid State Ionics.* 178(29):1568-1575.

Malek, K., Eikerling, M., Wang, Q., Navessin, T. & Liu, Z. 2007. Self-organization in catalyst layers of polymer electrolyte fuel cells. *The Journal of Physical Chemistry C.* 111(36):13627-13634.

Manahan, M.P., Kim, S., Kumbur, E.C. & Mench, M.M. 2009. Effects of surface irregularities and interfacial cracks on polymer electrolyte fuel cell performance. *ECS Transactions.* 25(1):1745-1754.

Mathias, M.F., Makharia, R., Gasteiger, H.A., Conley, J.J., Fuller, T.J., Gittleman, C.J., Kocha, S.S., Miller, D.P. et al. 2005. Two fuel cell cars in every garage. *Electrochem.Soc.Interface.* 14(3):24-35.

Millington, B., Du, S. & Pollet, B.G. 2011. The effect of materials on proton exchange membrane fuel cell electrode performance. *Journal of Power Sources.* 196(21):9013-9017.

Mixing & Blending Handbook 2001. High shear mixing advances for foods, pharmaceutiicals, cosmetics. In *The Mixing, Blending and Size Reduction Handbook.* 2nd ed. Putman. 2-7.

Ngo, T.T., Yu, T.L. & Lin, H. 2013. Influence of the composition of isopropyl alcohol/water mixture solvents in catalyst ink solutions on proton exchange membrane fuel cell performance. *Journal of Power Sources.* 225:293-303.

Ngo, T.T., Yu, T.L. & Lin, H. 2013. Nafion-based membrane electrode assemblies prepared from catalyst inks containing alcohol/water solvent mixtures. *Journal of Power Sources.* 238:1-10.

O'Hayre, R., Barnett, D.M. & Prinz, F.B. 2005. The triple phase boundary a mathematical model and experimental investigations for fuel cells. *Journal of the Electrochemical Society.* 152(2):A439-A444.

Özcan-Taşkin, N.G., Padron, G. & Voelkel, A. 2009. Effect of particle type on the mechanisms of break up of nanoscale particle clusters. *Chemical Engineering Research and Design.* 87(4):468-473.

Paipetis, A. & Kostopoulos, V. Eds. 2013. *Carbon Nanotube Enhanced Aerospace Composite Materials: A New Generation of Multifunctional Hybrid Structural Composites*. 1st ed. New York: Springer Science & Business Media. DOI:10.1007/978-94-007-4246-8.

Park, H., Cho, Y., Cho, Y., Jung, C.R., Jang, J.H. & Sung, Y. 2007. Performance enhancement of PEMFC through temperature control in catalyst layer fabrication. *Electrochimica Acta.* 53(2):763-767.

Passalacqua, E., Lufrano, F., Squadrito, G., Patti, A. & Giorgi, L. 2001. Nafion content in the catalyst layer of polymer electrolyte fuel cells: effects on structure and performance. *Electrochimica Acta.* 46(6):799-805.

Pollet, B.G. & Goh, J.T. 2014. The importance of ultrasonic parameters in the preparation of fuel cell catalyst inks. *Electrochimica Acta.* 128:292-303.

Poynton, S.D., Slade, R.C., Omasta, T.J., Mustain, W.E., Escudero-Cid, R., Ocón, P. & Varcoe, J.R. 2014. Preparation of radiation-grafted powders for use as anion exchange ionomers in alkaline polymer electrolyte fuel cells. *Journal of Materials Chemistry A.* 2(14):5124-5130.

Qi, Z. & Kaufman, A. 2002a. Activation of low temperature PEM fuel cells. *Journal of Power Sources.* 111(1):181-184.

Qi, Z. & Kaufman, A. 2002b. Enhancement of PEM fuel cell performance by steaming or boiling the electrode. *Journal of Power Sources.* 109(1):227-229.

Qi, Z. & Kaufman, A. 2003. Low Pt loading high performance cathodes for PEM fuel cells. *Journal of Power Sources.* 113(1):37-43.

Rajalakshmi, N. & Dhathathreyan, K. 2007. Catalyst layer in PEMFC electrodes—fabrication, characterisation and analysis. *Chemical Engineering Journal.* 129(1):31-40.

Ramani, V. 2006. Fuel Cells. The Electrochemical Society Interface.

Ren, X., Wilson, M.S. & Gottesfeld, S. 1996. High performance direct methanol polymer electrolyte fuel cells. *Journal of the Electrochemical Society.* 143(1):L12-L15.

Rieberer, S. & Norian, K.H. 1992. Analytical electron microscopy of nafion ion exchange membranes. *Ultramicroscopy.* 41(1):225-233.

Ross, C. 2015. *High Shear Mixers.* Available: http://www.highshearmixers.com/mixing.html.

Ryu, J. G., Lee, P. S., Kim, H. S., Lee, J. W. 2001. Development of PP-Based Nanocomposites via in-situ Copolymerisation and Melt Intercalcation With the Power Ultrasonic Wave. In *ANTEC 2001 Conference Proceedings*. 5

Saha, M.S., Paul, D.K., Peppley, B.A. & Karan, K. 2010. Fabrication of catalyst-coated membrane by modified decal transfer technique. *Electrochemistry Communications.* 12(3):410-413.

Scheiba, F., Benker, N., Kunz, U., Roth, C. & Fuess, H. 2008. Electron microscopy techniques for the analysis of the polymer electrolyte distribution in proton exchange membrane fuel cells. *Journal of Power Sources.* 177(2):273-280.

Seland, F., Berning, T., Børresen, B. & Tunold, R. 2006. Improving the performance of high-temperature PEM fuel cells based on PBI electrolyte. *Journal of Power Sources.* 160(1):27-36.

Shin, S., Lee, J., Ha, H., Hong, S., Chun, H. & Oh, I. 2002. Effect of the catalytic ink preparation method on the performance of polymer electrolyte membrane fuel cells. *Journal of Power Sources.* 106(1):146-152.

Sigma-Aldrich 2016. Nafion® perfluorinated resin solution. Available: http://www.sigmaaldrich.com/catalog/product/aldrich/274704?lang=en&region=ZA.

Singh, R., Akhgar, A., Sui, P., Lange, K. & Djilali, N. 2014. Dual-Beam FIB/SEM Characterization, Statistical Reconstruction, And Pore Scale Modeling of A PEMFC Catalyst Layer. *Journal of the Electrochemical Society.* 161(4):F415-F424.

Soboleva, T., Zhao, X., Malek, K., Xie, Z., Navessin, T. & Holdcroft, S. 2010. On the micro-, meso-, and macroporous structures of polymer electrolyte membrane fuel cell catalyst layers. *ACS Applied Materials & Interfaces.* 2(2):375-384.

Song, J., Cha, S. & Lee, W. 2001. Optimal composition of polymer electrolyte fuel cell electrodes determined by the AC impedance method. *Journal of Power Sources.* 94(1):78-84.

Song, S., Liang, Z., Zhou, W., Sun, G., Xin, Q., Stergiopoulos, V. & Tsiakaras, P. 2005. Direct methanol fuel cells: the effect of electrode fabrication procedure on MEAs structural properties and cell performance. *Journal of Power Sources.* 145(2):495-501.

Srinivasan, S. 2006. *Fuel cells: from fundamentals to applications.* Springer Science & Business media.

Stampino, P.G., Cristiani, C., Dotelli, G., Omati, L., Zampori, L., Pelosato, R. & Guilizzoni, M. 2009. Effect of different substrates, inks composition and rheology on coating deposition of microporous layer (MPL) for PEM-FCs. *Catalysis Today.* 147:S30-S35.

Su, H., Jao, T., Pasupathi, S., Bladergroen, B.J., Linkov, V. & Pollet, B.G. 2014. A novel dual catalyst layer structured gas diffusion electrode for enhanced performance of high temperature proton exchange membrane fuel cell. *Journal of Power Sources.* 246:63-67.

Suslick, K.S. 1998. Sonochemistry. *Kirk-Othmer Encyclopedia of Chemical Technology.*

Suslick, K.S. & Price, G.J. 1999. Applications of ultrasound to materials chemistry. *Annual Review of Materials Science.* 29(1):295-326.

Suzuki, T., Tsushima, S. & Hirai, S. 2011. Effects of Nafion® ionomer and carbon particles on structure formation in a proton-exchange membrane fuel cell catalyst layer fabricated by the decal-transfer method. *International Journal of Hydrogen Energy.* 36(19):12361-12369.

Tadros, T.H. Ed. 1987. *Solid/Liquid Dispersion*. Orlando, Florida: Academic Press Inc.

Tang, H., Santamaria, A., Kurniawan, J., Park, J.W., Yang, T. & Sohn, Y. 2010. Developing a 3D neutron tomography method for proton exchange membrane fuel cells. *Journal of Power Sources.* 195(19):6774-6781.

Tanuma, T. & Kinoshita, S. 2012. Impact of gas diffusion layers (GDLs) on MEA performance in PEFCs. *Energy Procedia.* 28:12-19.

Therdthianwong, A., Ekdharmasuit, P. & Therdthianwong, S. 2010. Fabrication and performance of membrane electrode assembly prepared by a catalyst-coated membrane method: effect of solvents used in a catalyst ink mixture. *Energy & Fuels.* 24(2):1191-1196.

Ticianelli, E., Derouin, C., Redondo, A. & Srinivasan, S. 1988. Methods to advance technology of proton exchange membrane fuel cells. *Journal of the Electrochemical Society.* 135(9):2209-2214.

U.S. Department of Energy 2014. *Fuel Cell System Cost - 2013.* Available: https://www.hydrogen.energy.gov/pdfs/14012_fuel_cell_system_cost_2013.pdf.

U.S. Department of Energy 2015. *Types of Fuel Cells.* Available: http://energy.gov/eere/fuelcells/types-fuel-cells [2015, August 6].

Uchida, H., Song, J.M., Suzuki, S., Nakazawa, E., Baba, N. & Watanabe, M. 2006. Electron tomography of nafion ionomer coated on Pt/carbon black in high utilization electrode for PEFCs. *The Journal of Physical Chemistry B.* 110(27):13319-13321.

Uchida, M., Aoyama, Y., Eda, N. & Ohta, A. 1995. Investigation of the Microstructure in the Catalyst Layer and Effects of Both Perfluorosulfonate Ionomer and PTFE-Loaded Carbon on the Catalyst Layer of Polymer Electrolyte Fuel Cells. *Journal of the Electrochemical Society.* 142(12):4143-4149.

Uchida, M., Fukuoka, Y., Sugawara, Y., Ohara, H. & Ohta, A. 1998. Improved Preparation Process of Very-Low-Platinum-Loading Electrodes for Polymer Electrolyte Fuel Cells. *Journal of the Electrochemical Society.* 145(11):3708-3713.

Vielstich, W., Lamm, A. & Gasteiger, H.A. 2009. *Handbook of fuel cells: fundamentals, technology, and applications.* John Wiley & Sons.

Wainwright, M. 2015. *http://www.analytical.unsw.edu.au/facilities/emu/instruments/fei-nova-nanosem-230-fesem*. Available: http://www.analytical.unsw.edu.au/facilities/emu/instruments/fei-nova-nanosem-230-fesem.

Wang, S., Sun, G., Wu, Z. & Xin, Q. 2007. Effect of Nafion® ionomer aggregation on the structure of the cathode catalyst layer of a DMFC. *Journal of Power Sources.* 165(1):128-133.

Wang, Y., Chen, K.S., Mishler, J., Cho, S.C. & Adroher, X.C. 2011. A review of polymer electrolyte membrane fuel cells: technology, applications, and needs on fundamental research. *Applied Energy.* 88(4):981-1007.

Wang, H., Li, H. & Yuan, X. 2011. *PEM fuel cell failure mode analysis.* CRC Press.

Wannek, C., Lehnert, W. & Mergel, J. 2009. Membrane electrode assemblies for high-temperature polymer electrolyte fuel cells based on poly (2, 5-benzimidazole) membranes with phosphoric acid impregnation via the catalyst layers. *Journal of Power Sources.* 192(2):258-266.

Wannek, C., Nehr, S., Vahlenkamp, M., Mergel, J. & Stolten, D. 2010. Pseudo-half-cell measurements on symmetrical catalyst-coated membranes and their relevance for optimizing DMFC anodes. *Journal of Applied Electrochemistry.* 40(1):29-38.

Wilkinson, D.P., Zhang, J., Hui, R., Fergus, J. & Li, X. 2009. *Proton exchange membrane fuel cells: materials properties and performance.* CRC Press.

Williams, M., Khotseng, L., Naidoo, Q., Petrik, L., Nechaev, A. & Linkov, V. 2009. Applicability of analytical protocols for the characterisation of carbon-supported platinum group metal fuel cell electrocatalysts. *South African Journal of Science.* 105(7-8):285-289.

Wilson, M. & Gottesfeld, S. 1992a. Thin-film catalyst layers for polymer electrolyte fuel cell electrodes. Journal of Applied Electrochemistry. 22(1):1-7. DOI:10.1007/BF01093004.

Wilson, M.S. & Gottesfeld, S. 1992b. High Performance Catalyzed Membranes of Ultra-low Pt Loadings for Polymer Electrolyte Fuel Cells. *Journal of the Electrochemical Society.* 139(2):L28-L30.

Wilson, M.S., Valerio, J.A. & Gottesfeld, S. 1995. Low platinum loading electrodes for polymer electrolyte fuel cells fabricated using thermoplastic ionomers. *Electrochimica Acta.* 40(3):355-363.

Wu, J., Yuan, X.Z., Wang, H., Blanco, M., Martin, J.J. & Zhang, J. 2008. Diagnostic tools in PEM fuel cell research: Part I Electrochemical techniques. *International Journal of Hydrogen Energy.* 33(6):1735-1746.

Xie, J., More, K.L., Zawodzinski, T.A. & Smith, W.H. 2004. Porosimetry of MEAs made by "thin film decal" method and its effect on performance of PEFCs. *Journal of the Electrochemical Society.* 151(11):A1841-A1846.

Xu, H., Brosha, E.L., Garzon, F., Uribe, F., Wilson, M. & Pivovar, B. 2007. The effect of electrode ink processing and composition on catalyst utilization. *ECS Transactions.* 11(1):383-391.

Yang, T., Yoon, Y., Park, G., Lee, W. & Kim, C. 2004. Fabrication of a thin catalyst layer using organic solvents. *Journal of Power Sources.* 127(1):230-233.

Yoon, Y.J., Kim, T., Kim, S.U., Yu, D.M. & Hong, Y.T. 2011. Low temperature decal transfer method for hydrocarbon membrane based membrane electrode assemblies in polymer electrolyte membrane fuel cells. *Journal of Power Sources.* 196(22):9800-9809.

Yuan, T., Zhang, H., Zou, Z., Khatun, S., Akins, D., Adam, Y. & Suarez, S. 2012a. A study of the effect of heat-treatment on the morphology of Nafion ionomer dispersion for use in the passive direct methanol fuel cell (DMFC). *Membranes.* 2(4):841-854.

Yuan, X., Sun, J.C., Wang, H. & Li, H. 2012b. Accelerated conditioning for a proton exchange membrane fuel cell. *Journal of Power Sources.* 205:340-344.

Yuan, X. & Wang, H. 2008. PEM fuel cell fundamentals. In *PEM Fuel Cell Electrocatalysts and Catalyst Layers.* Springer. 1-87.

Yudianti, R., Onggo, H. & Syampurwadi, A. 2014. Molecular Conformation of Nafion Ionomer on Electrocatalyst Layer Prepared by Screen Printing Technique. Int.J.Electrochem.Sci. 9:3047-3059.

Zaidi, S.J. 2009. Research trends in polymer electrolyte membranes for PEMFC. In *Polymer membranes for fuel cells.* Springer. 7-25.

Zhang, J., Xu, S. & Li, W. 2012. High shear mixers: A review of typical applications and studies on power draw, flow pattern, energy dissipation and transfer properties. *Chemical Engineering and Processing: Process Intensification.* 57:25-41.

Zhang, J. 2008. *PEM fuel cell electrocatalysts and catalyst layers: fundamentals and applications.* Springer Science & Business Media.

Zhang, X., Gao, Y., Ostadi, H., Jiang, K. & Chen, R. 2015. Method to improve catalyst layer model for modelling proton exchange membrane fuel cell. *Journal of Power Sources.* 289:114-128.

Zhao, J., He, X., Wang, L., Tian, J., Wan, C. & Jiang, C. 2007. Addition of NH 4 HCO 3 as pore-former in membrane electrode assembly for PEMFC. *International Journal of Hydrogen Energy.* 32(3):380-384.

Ziegler, C., Thiele, S. & Zengerle, R. 2011. Direct three-dimensional reconstruction of a nanoporous catalyst layer for a polymer electrolyte fuel cell. *Journal of Power Sources.* 196(4):2094-2097.

10. Appendix A: SEM Images of CCM's

In the figures (Figure 72, Figure 73 and Figure 74) are SEM images showing the morphology of CLs, after decal transfer. As seen, the surfaces of the CLs are squashed as a result of high pressure hot pressing. Therefore, the effects of mixing cannot be observed as the images are indistinguishable.

BM-3000-5

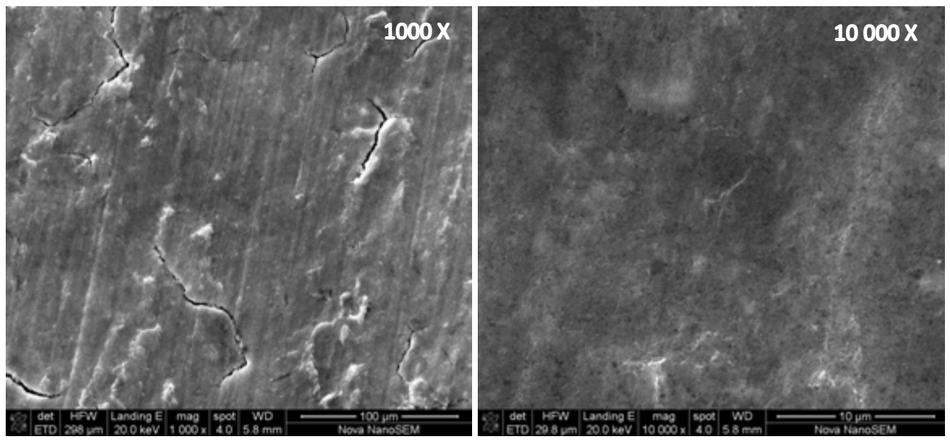

BM-3000-30

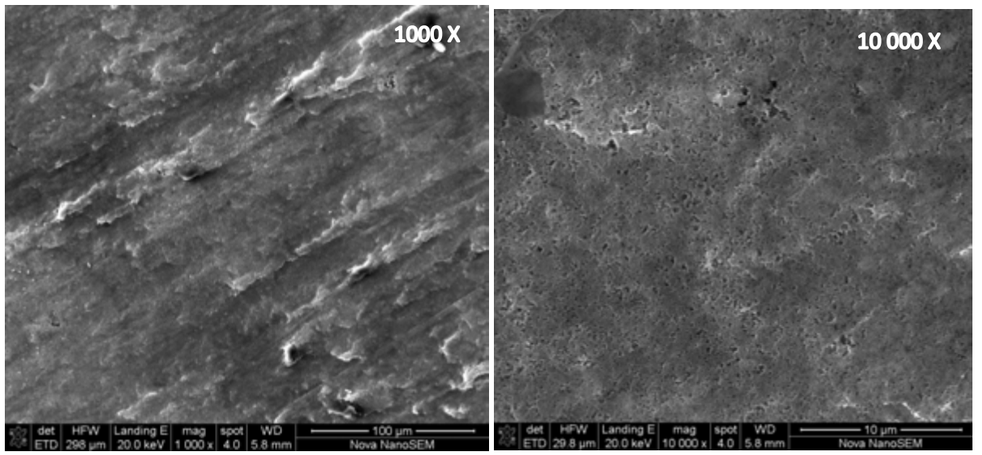

BM-200-5

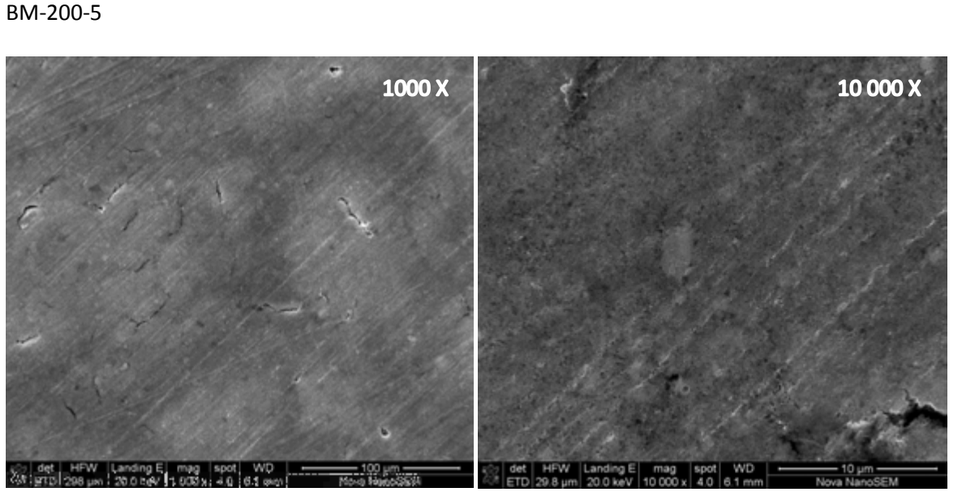

BM-200-30

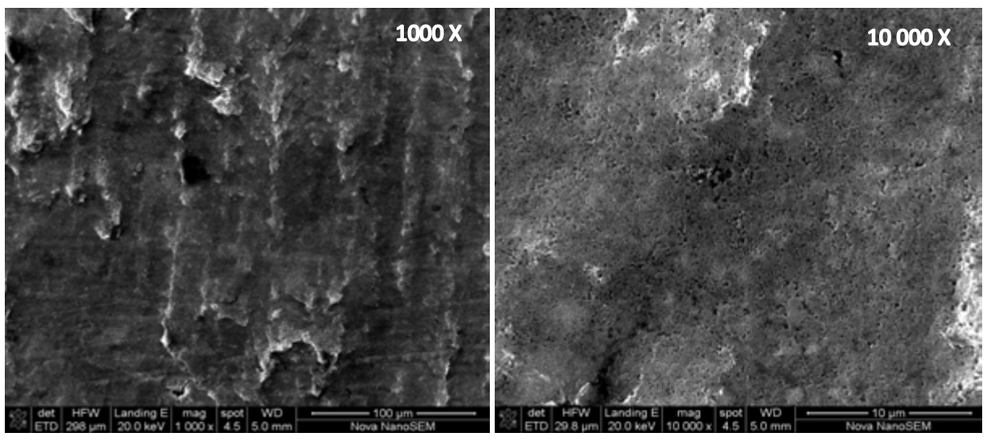

Figure 72: SEM analysis for CCMs produced by a variation in parameters of the BM mixing technique.

A

HSS-9000-5

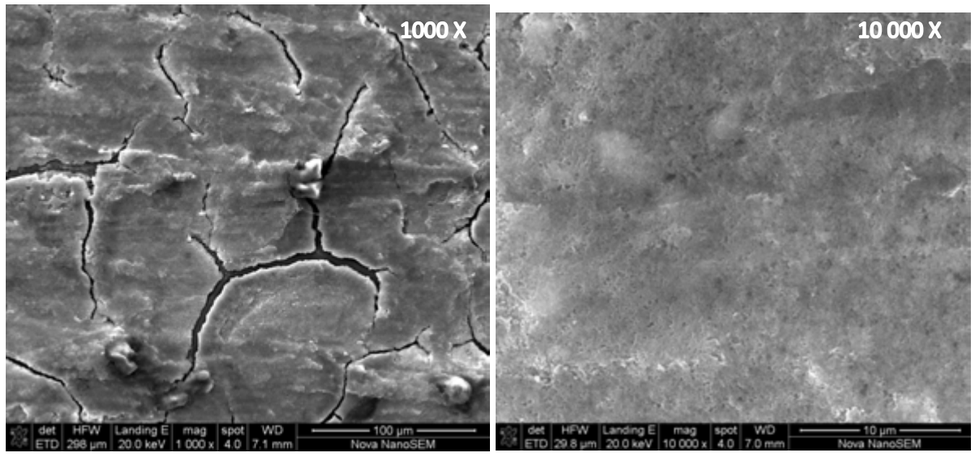

HSS-9000-30

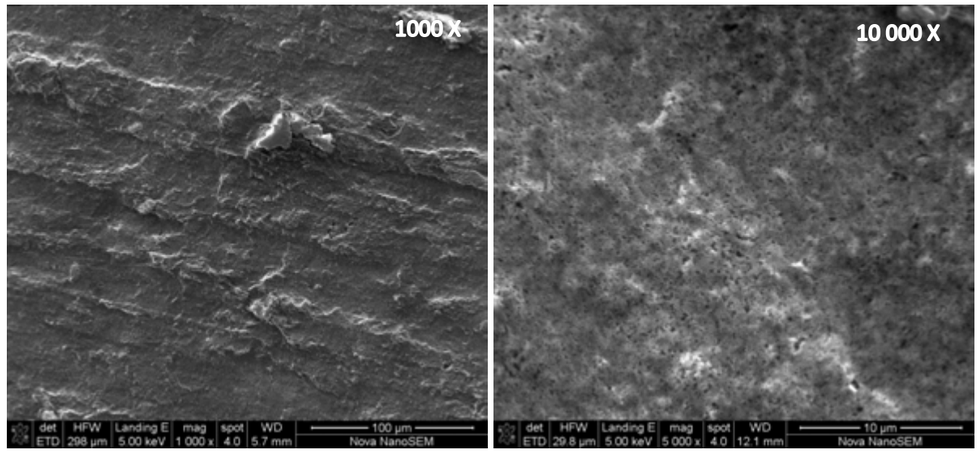

HSS-2000-5

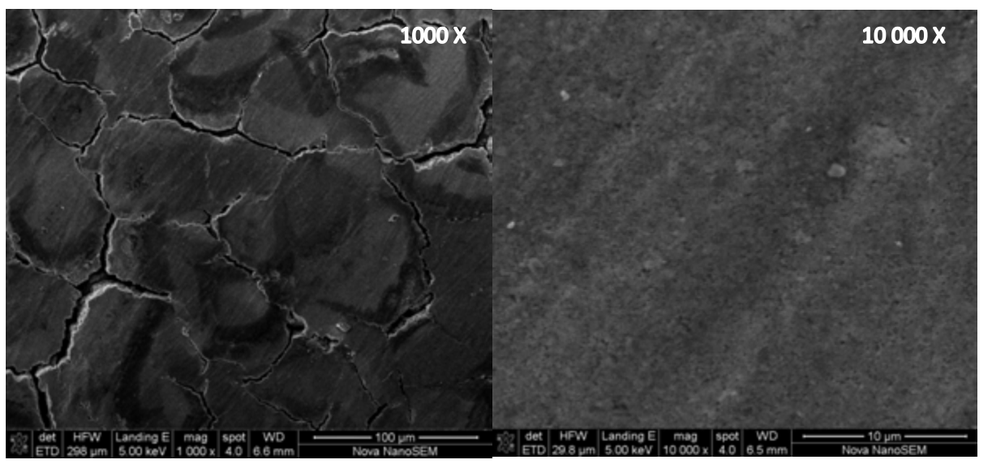

HSS-2000-30

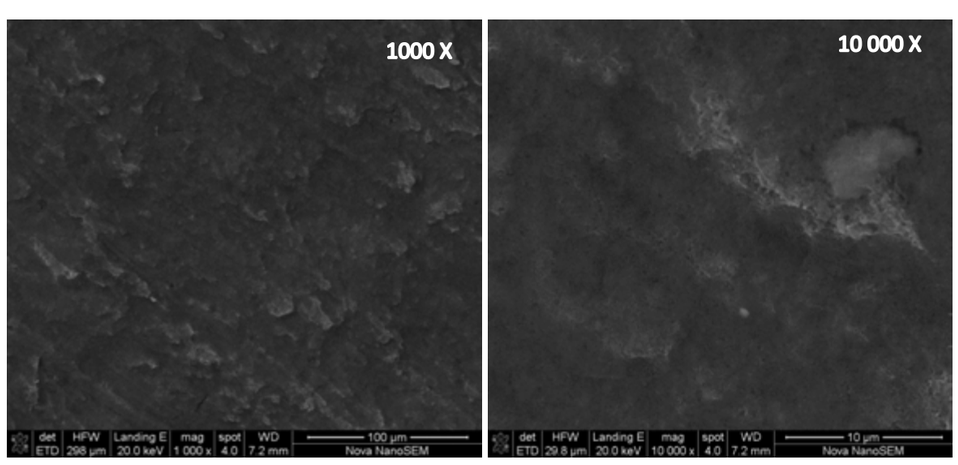

Figure 73: SEM analysis for CCMs produced by a variation in parameters of the HSS mixing technique.

UH-4.35-5

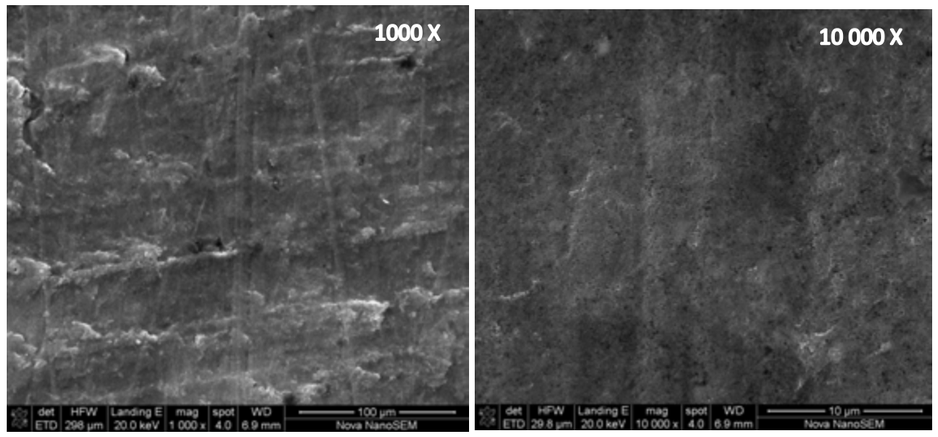

UH-4.35-30

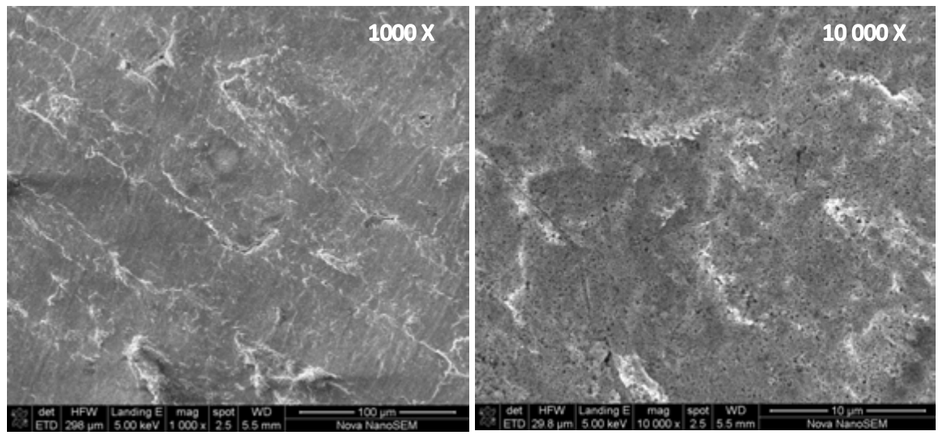

UH-1.10-5

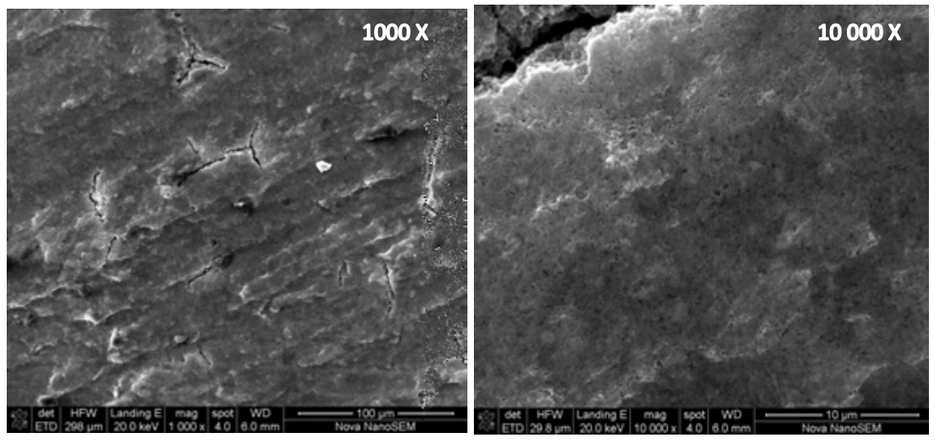

UH-1.10-30

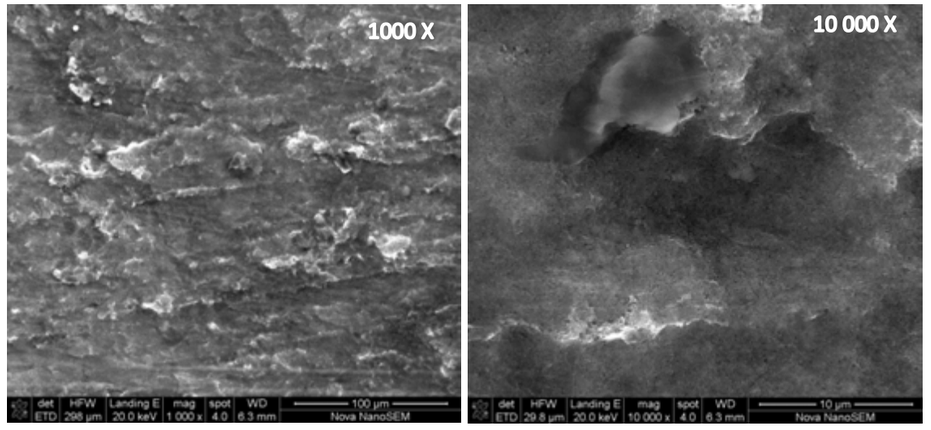

Figure 74: SEM analysis for CCMs produced by a variation in parameters of the UH mixing technique.

11. Appendix B: Oxygen Polarisation Curves

Oxygen polarisation curves was conducted for comparative analysis with other in-situ performance tests. However, they were not directly used in the results and the graphs are shown below.

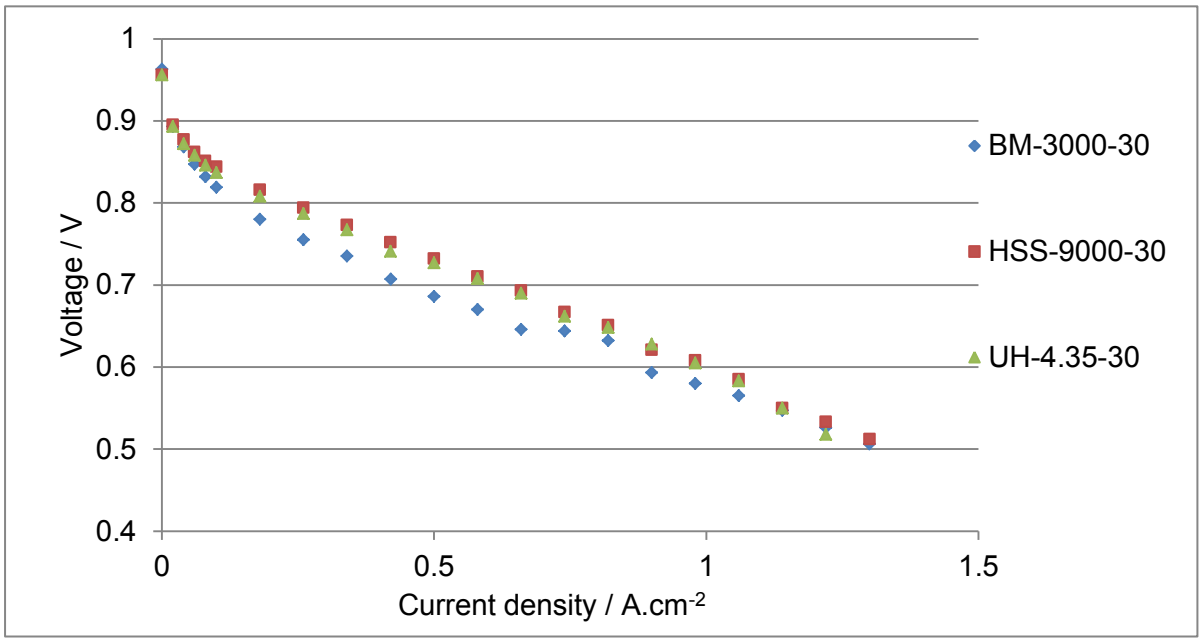

Figure 75: H_2/O_2 Polarisation curves for MEAs prepared by inks mixed with different techniques. N/C = 1 for all electrodes. Testing conditions: T_{cell}=80˚C, RH=100%, gases at 1 bar using N212 membrane and SGL24BC GDL.

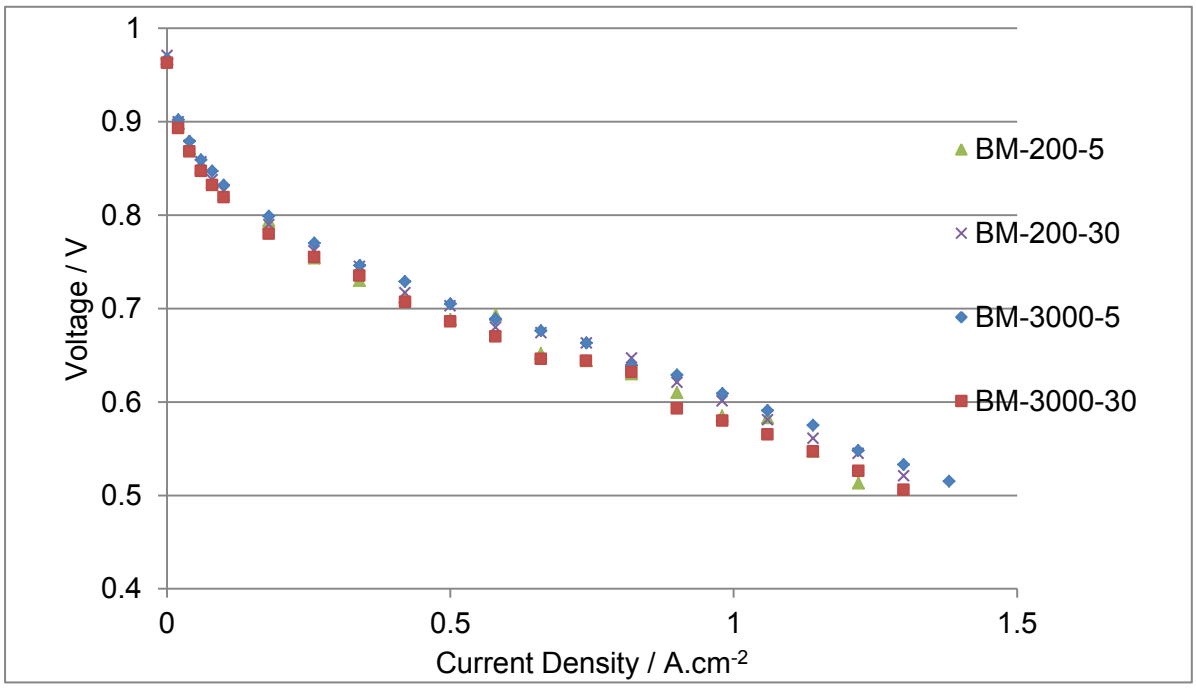

Figure 76: H_2/O_2 Polarisation curves for MEAs prepared by inks mixed using BM. N/C = 1 for all electrodes. Testing conditions: T_{cell}=80˚C, RH=100%, gases at 1 bar using N212 membrane and SGL24BC GDL.

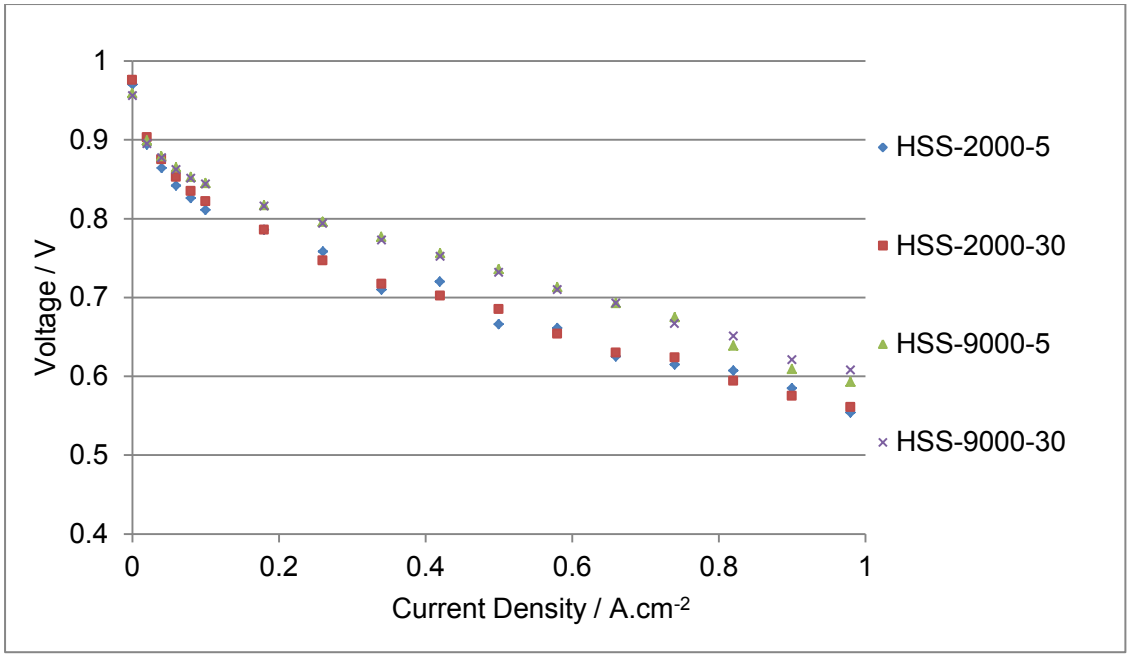

Figure 77: H_2/O_2 Polarisation curves for MEAs prepared by inks mixed using variable parameters of HSS. N/C = 1 for all electrodes. Testing conditions: T_{cell}=80˚C, RH=100%, gases at 1 bar using N212 membrane and SGL24BC GDL

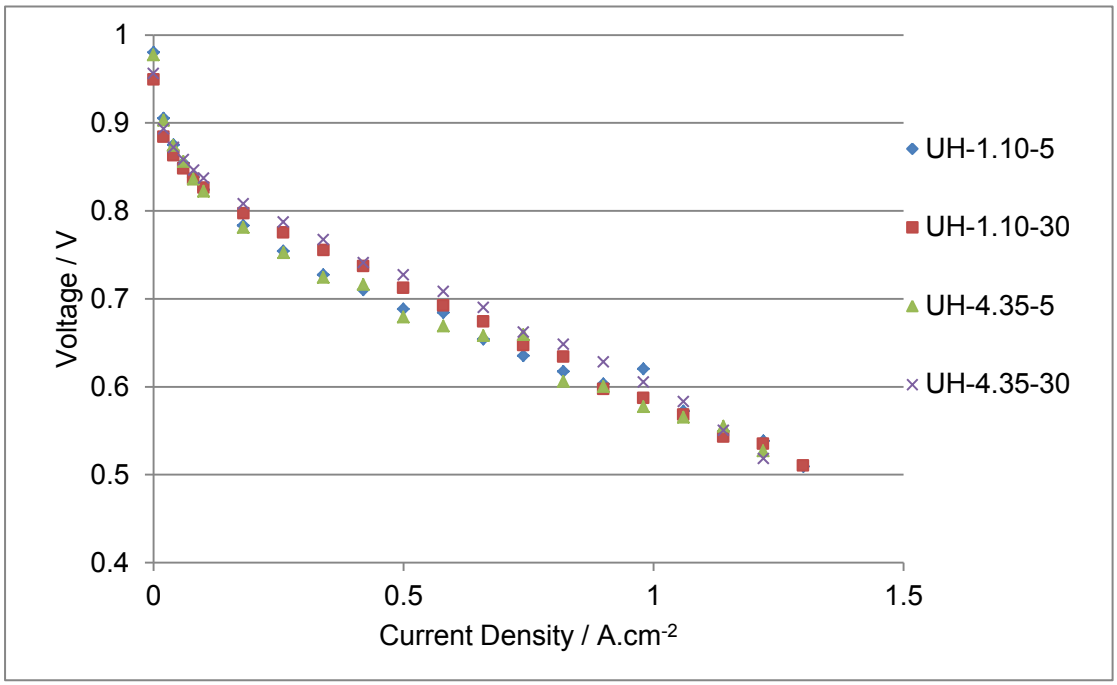

Figure 78: H_2/O_2 Polarisation curves for MEAs prepared by inks mixed using variable parameters of UH. N/C = 1 for all electrodes. Testing conditions: T_{cell}=80˚C, RH=100%, gases at 1 bar using N212 membrane and SGL24BC GDL.

12. Appendix C: Assessment of Ethics Form

EBE Faculty: Assessment of Ethics in Research Projects

Any person planning to undertake research in the Faculty of Engineering and the Built Environment at the University of Cape Town is required to complete this form before collecting or analysing data. When completed it should be submitted to the supervisor (where applicable) and from there to the Head of Department. If any of the questions below have been answered YES, and the applicant is NOT a fourth year student, the Head should forward this form for approval by the Faculty EIR committee: submit to Ms Zakiya Chikte (Zakiya.chikte@uct.ac.za); New EBE Building, Ph 021 650 5739). Students must include a copy of the completed form with the dissertation/thesis when it is submitted for examination.

Name of Principal Researcher/Student: Clayton Jacobs — Department: Chemical Engineering

If a Student: — Degree: Masters — Supervisor: Dr. Pieter Levecque

If a Research Contract indicate source of funding/sponsorship:

Research Project Title: Influence of catalyst ink mixing procedures on catalyst layer properties and in-situ PEFC performance

Overview of ethics issues in your research project:

Question 1: Is there a possibility that your research could cause harm to a third party (i.e. a person not involved in your project)?		NO
Question 2: Is your research making use of human subjects as sources of data? If your answer is YES, please complete Addendum 2.		NO
Question 3: Does your research involve the participation of or provision of services to communities? If your answer is YES, please complete Addendum 3.		NO
Question 4: If your research is sponsored, is there any potential for conflicts of interest? If your answer is YES, please complete Addendum 4.		NO

If you have answered YES to any of the above questions, please append a copy of your research proposal, as well as any interview schedules or questionnaires (Addendum 1) and please complete further addenda as appropriate.

I hereby undertake to carry out my research in such a way that

- there is no apparent legal objection to the nature or the method of research; and
- the research will not compromise staff or students or the other responsibilities of the University;
- the stated objective will be achieved, and the findings will have a high degree of validity;
- limitations and alternative interpretations will be considered;
- the findings could be subject to peer review and publicly available; and
- I will comply with the conventions of copyright and avoid any practice that would constitute plagiarism.

Signed by:

	Full name and signature	Date
Principal Researcher/Student: Signed	Clayton Jacobs	31/03/2016

This application is approved by:

Supervisor (if applicable):	PIETER LE VECQUE	31/03/2016
HOD (or delegated nominee): Final authority for all assessments with NO to all questions and for all undergraduate research.	Signed	31-3-2016
Chair : Faculty EIR Committee For applicants other than undergraduate students who have answered YES to any of the		